A NEW VIEW OF THE GRAIN-COARSENING BEHAVIOR OF AUSTENITE IN TI-MICROALLOYED LOW-CARBON STEELS

by

Victor Blancas-Garcia

BS in Industrial Physics Engineering, Instituto Teconológico y de Estudios Superiores de Monterrey, 2004

Submitted to the Graduate Faculty of

the Swanson School of Engineering in partial fulfillment

of the requirements for the degree of

Master of Science in Materials Science and Engineering

University of Pittsburgh

2016

UNIVERSITY OF PITTSBURGH

SWANSON SCHOOL OF ENGINEERING

This thesis was presented

by

Victor Blancas-Garcia

It was defended on

October 27, 2016

and approved by

C. Isaac Garcia, Ph.D., Professor,
Department of Mechanical Engineering and Materials Science

Ian Nettleship, Ph.D., Professor,
Department of Mechanical Engineering and Materials Science

Susheng Tan, Ph.D., Research Assistant Professor,
Department of Electrical and Computer Engineering

Thesis Advisor: C. Isaac Garcia, PhD., Professor,
Department of Mechanical Engineering and Materials Science

A NEW VIEW OF THE GRAIN-COARSENING BEHAVIOR OF AUSTENITE IN TI-MICROALLOYED LOW-CARBON STEELS

Victor Blancas-Garcia, M.S.

University of Pittsburgh, 2016

The role of Microalloying Element (MAE) additions to high strength low-allow (HSLA) steels has been well-documented since their commercial introduction in the late 1950's. Because of the benefits of MAE in terms of grain size control, among other metallurgical reactions, it has been important to study, understand and predict the role of MAE content on the grain coarsening behavior under different thermal cycles. Titanium content has shown beneficial effects in terms of austenite grain size control by the grain boundary pinning effect of TiN particles due to the low solubility of these precipitates at high temperatures. The thermodynamical stability of TiN is mainly influenced by the contents of both Ti and N which leads to hypo-stoichiometric and hyper-stoichiometric conditions for TiN particles nucleation, coarsening, and dissolution. Prior Austenite Grain Size studies and precipitation analysis have shown that these stoichiometric conditions play a role on the kinetics of the grain coarsening behavior under different thermal cycles by means of the available solute concentration in the matrix as predicted by particle coarsening theories and grain growth models. A systematic analysis of the grain boundaries character distribution (GBCD) by Electron Backscattered Diffraction and Electron Microscopy during the dissolution process of TiN precipitates has been conducted. These observations provided a better understanding of the role of GBCD in the presence or absence of TiN

particles located at the matrix and along the austenite grain boundaries. The results obtained from this study gave a strong correlation between the high angle boundaries with misorientations between 20° and 45° and the estimated pinning force exerted by TiN particles, providing therefore a new view for studying the kinetics of austenite grain coarsening behavior for different MAE contents.

TABLE OF CONTENTS

LIST OF TABLES

LIST OF FIGURES

LIST OF EQUATIONS

ACKNOWLEDGEMENTS

I wish to express my gratitude and appreciation to Dr. Isaac Garcia for his continuous encouragement, support, guidance, and confidence throughout this project.

I would like to gratefully acknowledge the financial support from my sponsoring company, Tenaris, which allowed me to focus all efforts on my education and research work. Special thanks to Héctor Quintanilla and Enrique García who gave me this unique opportunity of pursuing a graduate degree as part of my professional development in the company. I also wish to thank my colleagues Mauricio Pelcastre, Marisa Hernández, and Fernando Barradas from the Metallurgy and Materials team in Mexico, for all their support with the activities at TenarisTamsa facilities; and to my colleagues Gonzalo Gómez and Martín Valdez in Argentina for their support with the Gleeble experiments. I am also grateful to my teammates from the Ferrous Physical Metallurgy group at the University of Pittsburgh: Aihua, Gregorio, Allan, Rafael, Louis, Siwei, Dayong, Austen, Cain, Bob, Kevin for their support, training, and patience during this project. I also wish to thank Dr. Susheng Tan for his training and support with the TEM activities.

Finally, I would like to thank my family for their constant love and patience, and to my friends for their company, encouraging conversations, and best wishes in every step of the process.

1.0 INTRODUCTION

Nearly 80 years of fundamental understanding of austenite grain coarsening behavior in steels, several studies have been conducted aiming at understanding the role of microalloying elements (MAE) content in metallurgical controlling mechanisms and final material performance. Because of their beneficial contributions in the strengthening mechanisms, MAEs have been extensively used in the steel manufacturing industry and their study keeps attracting the attention of the scientific community, in particular the field of physical metallurgy of materials science. Current progress in the design of new microstructures from microalloyed technology, in synergy with processing advancements and advanced material characterization techniques, has been driven by the higher strength, enhanced toughness, and weldability of the modern steel designs demanded mainly by the oil and gas, construction, and automotive industries.

Several publications have described and documented the benefits of MAEs, such as V, Nb, and Ti, in terms of their control on metallurgical reactions which include austenite grain size control, microstructural refinement during hot deformation, and transformation control for precipitation strengthening, among others [1-6]. Most of these reactions occur because of the ability of MAE to form carbides, nitrides or complex carbo-nitrides that can remain stable at high temperatures and thermal cycles characteristic of steel processing and welding operations.

Ti-microalloying content additions to low-carbon steels have shown beneficial effects in terms of austenite grain size control at high temperatures and extreme thermal cycles (i.e. welding operations) by the grain boundary pinning effect of TiN stable particles that have very low solubility [7, 8]. The thermodynamical stability of these particles is influenced mainly by the contents of both Ti and N which leads to hypo-stoichiometric and hyper-stoichiometric conditions for TiN particle nucleation, coarsening, and dissolution [9, 10].

Prediction of the austenite grain coarsening behavior in microalloyed steels based on experimental data can be obtained by the use of different models available which take into account a balance between the driving forces and the inhibition or retardation forces (pinning forces) due to the presence of secondary phase particles [11]. Particle size and volume fraction of secondary phase particles can be estimated by the use of solubility product and the particle coarsening theories given by kinetic analysis of the Gibbs-Thomson equation. Most of these models, however, rely on isothermal experiments and steady-state conditions.

Despite the wealth of information available in the literature related to the role of Ti and other MAEs in the austenite grain-coarsening behavior of steels, there are still some questions regarding a better quantitative and analytical understanding of the growth and dissolution of stable precipitates and the austenite grain structure evolution. In addition, there is still some concern on developing an understanding in the control and behavior of the austenite grain size under extreme thermal cycles, i.e. welding operations, as well as in knowing the limit where the addition of MAEs becomes ineffective or detrimental to the final material performance.

This work aims at providing a systematic analysis on the effect of Ti microalloying content on the austenite grain coarsening behavior of low carbon steel designs under different thermal cycle conditions. Precipitation dissolution and coarsening, as well as their correlation with grain size classical thermodynamical and topographical prediction models are aspects included in this study. In addition, a systematic analysis of the grain boundaries character distribution (GBCD) by Electron Backscatter Detection (EBSD) and electron microscopy has been conducted in order to provide a better understanding of the stability of TiN precipitates and their potential role in the kinetics of the austenite grain coarsening behavior.

2.0 LITERATURE REVIEW

2.1 MICROALLOYING ELEMENTS IN LOW CARBON STEEL DESIGNS

Microalloying Elements (MAE) such as Titanium, Vanadium, and Niobium have been extensively used in low carbon steels as a result of their effect by relatively small amount additions on the strengthening mechanisms. The tensile properties are increased by precipitation strengthening, while the impact toughness by grain size refinement. In addition, because low carbon contents, the weldability is also improved [9, 11-16]. Their beneficial effect is enhanced when combined with processing technologies, such as accelerated cooling; direct quenching, and thermo-mechanical controlled processing.

Studies on the understanding of the niobium microalloying influence of mechanical properties of low-carbon steels started to be conducted by several Universities around the world in the late 50's and this triggered a significant number of research work in this subject at the time, many of which were also motivated by the discovery of large deposits of niobium bearing ores in Canada and Brazil [1].

Baker provides a good review on the role of vanadium in the development of new steel designs as a nitride and carbide former, its stability and precipitation hardening effect during tempering while stressing some of the current controversial topics regarding several mechanisms involved when vanadium is added as a MAE [2].

The role of titanium microalloying content additions on low carbon steels has been widely studied since this element forms titanium nitrides (TiN) that have very low solubility in austenite even at temperatures above 1350°C, which makes it an attractive choice for the controlling of the austenite grain under high temperature processes.

Current progress in the design of new microstructures from microalloyed technology in synergy with processing advancements are mostly driven by the higher strength, enhanced toughness and weldability of the modern steel designs demanded mainly by the oil and gas, construction, and automotive industries.

Microalloying additions on carbon steel designs are known for having a crucial role in retarding the kinetics of recrystallization, austenite grain size control under operative thermal cycles as well as the inhibition of grain boundary and dislocation movement. These additions are considered effective for such mechanisms as long as they result in finely dispersed stable nitrides or carbides.

2.2 AUSTENITE GRAIN COARSENING IN MICROALLOYED STEELS

It is well understood that the main driving force for austenite grain coarsening is the reduction of the grain boundary interfacial energy. In theory, if impurities, defects, solutes, or other secondary particles are absent in polycrystalline structure, grain boundary mobility at a high temperature will tend to reduce the grain-boundary area per volume in the system leading to form a single crystal. Fine and uniform austenite grain size distribution represents a high grain boundary area with a high interfacial energy and

because this condition is thermodynamically unstable, larger grains will grow at the expense of smaller grains through a mechanisms known as coalescence [17]. Given this principle and the fact that the most effective way to increase both strength and toughness in a given steel is by obtaining a fine grain-sized microstructure, the understanding of the parent austenite grain coarsening behavior of micro-alloyed steels during reheating processes and thermal cycles is relevant for achieving the desired mechanical properties on the final product.

Numerous studies of austenite grain growth behavior in metals have been conducted under isothermal conditions. Beck et al. first proposed the power function expression (Equation 2.1) as a result from experimental grain size measurements in high purity aluminum specimens [18].

$$D^n - D_0^n = C \cdot t \qquad \textbf{Equation 2.1}$$

where D and D_0 is the actual and initial grain size diameter, respectively, t is the holding time at temperature, and n and C are constants (independent of the grain size) that are a function of the alloy chemical composition and the holding temperature during the isothermal treatment. The value n is also known as the grain growth exponent and C is the rate constant follows an Arrhenius-like dependence as follows:

$$C = A \cdot e^{\left(-\frac{Q}{RT}\right)} \qquad \textbf{Equation 2.2}$$

where A is the pre-exponential term, Q is the activation energy for grain boundary mobility, R is the universal gas constant (8.314 J/mol·K), and T is the holding temperature. Constants n and C can be determined through the analysis of information obtained from grain size measurements after isothermal experiments.

Moreover, in microalloyed steels, grain boundary mobility can be reduced or inhibited by the presence of stable secondary particles in the system, such as inclusions and precipitates, that will exert a pinning force against the grain growth driving forces [3, 6-8, 11]. Grain Growth is inhibited as long as the pinning force exceeds the driving force for grain growth (Equation 2.3.) Some of the mechanisms explained by many authors are included in the following sections.

$$F_{pin} \gg F_{GG} \qquad \textbf{Equation 2.3}$$

where F_{pin} is the pinning force exerted by secondary particles, and F_{GG} is the driving force for grain growth in the system. The pinning effect is thus a function of the stability of these secondary stable particles which is interdependent on their volume fraction, size distribution, morphology, as well as the concentration of micro-alloying elements in the system. As it has been presented and concluded by many authors in the literature, the general rule for effective grain growth inhibition is to obtain a large volume fraction of fine stable precipitates [6, 19-23].

2.2.1 Precipitation Stability and Solubility Product

The formation of ordered phases or precipitates depends ultimately on the chemical composition of the alloy system and their stability can be affected by an external heat energy applied in the system such as in the case of a reheating process, a welding thermal cycle or a heat treatment schedule.

The thermodynamic stable form of a microalloying element in austenite can be present as nitride, carbide or in solid solution. When more than one nitride or carbide-

forming microalloying elements are present, complex carbo-nitrides may be formed in the system [11]. The reaction of a nitride or carbide former and an interstitial element can be expressed as:

$$[M] + [X] \leftrightarrow (MX) \quad \textbf{Equation 2.4}$$

where [*M*] is the concentration of the nitride or carbide former (i.e. Ti, Nb, or V) dissolved in austenite, [*X*] is the concentration of the interstitial element (i.e. N or C) and (*MX*) is the compound formed by these two elements.

The isothermal equilibrium constant for the compound (*MX*) can be represented by the product of [*M*] and [*X*] as follows:

$$K_S = [M][X] \quad \textbf{Equation 2.5}$$

where K_S is the equilibrium constant, also known as the solubility product. The temperature dependence of the equilibrium constant K_S can be expressed in the following form [11]:

$$logK_S = -\frac{Q}{2.303 \cdot RT} + A \qquad \textbf{Equation 2.6}$$

where $logK_S$ is the logarithm to the base 10 of the equilibrium constant, Q is the heat of dissolution, R is the universal gas constant, and A is a constant that depends on the precipitate formed. The reduced form of Equation 2.6 typically used in the literature is by the definition of constants A and B expressed by the following equation:

$$logK_S = A - \frac{B}{T} \qquad \textbf{Equation 2.7}$$

Solubility product constants A and B can be determined by several methods and there is usually more than one reference in the literature. Some of the methods are the

precipitate extraction, gaseous equilibrium and thermodynamic calculations. Table 2.1 presents example values for A and B available in the literature for common precipitates.

Table 2.1. Solubility products for different precipitates in Figure 2.1 [11, 24]

Precipitate	Ferrite		Austenite	
	A	B	A	B
AlN	2.05	8790	1.03	6770
NbN	4.91	12170	3.79	10150
$NbC_{0.87}$	4.33	9830	2.81	7020
TiN	6.40	18420	5.40	15790
TiC	4.45	10230	2.75	7000
VN	3.90	9720	2.86	7700
$VC_{0.75}$	4.24	7050	4.45	6560

Figure 2.1 depicts the temperature dependence for the different solubility products presented in Table 2.1.

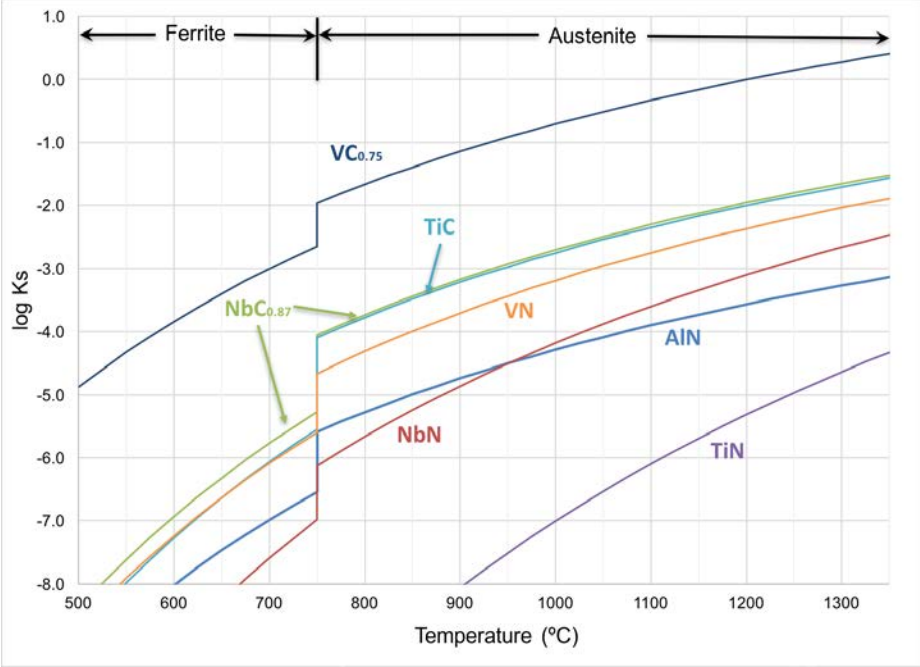

Figure 2.1. Temperature dependence of the solubility products of different precipitates (constructed from data presented in references [11] and [24])

Based on the solubility data of carbides and nitrides formed by the different most common microalloying elements, it is expected that the low solubility of TiN will result in higher volume fraction in austenite at high temperatures in comparison with other microalloy nitrides and carbides. Vanadium precipitates on the contrary would be dissolved at considerably lower temperatures. Table 2.2 presents some of the solubility product constants for TiN in austenite found in the literature.

Table 2.2. Solubility product constants for TiN in austenite following Equation 2.6

Reference	A	B
Inoue et al. [25]	4.35	14890
Turkdogan et al. [26]	5.4	15790
Kunze et al. [27]	5.19	15490
Gurevic et al. [27]	6.75	19740
Irvine et al. [11]	3.82	15020
Wada et al. [28]	4.94	14400
Matsuda and Okumura [11]	0.322	8000

Solubility data is helpful in the calculation of the amount of undissolved microalloyed precipitates for a particular steel composition at a certain temperature in equilibrium and therefore it is possible to estimate the temperature at which the nitrides or carbides can be dissolved, and consequently to estimate the amount of microalloying element available in solid solution.

Precipitates can be also classified by their coherency with respect to the matrix; this degree of coherency will define their morphology and also their effectiveness in exerting pinning force on grain boundary mobility [29, 30]. Coherent precipitates have the same

crystal structure as the matrix with a different chemical composition; these precipitates usually have the form of plates, needles or spheres and they are in a metastable state. Semi-coherent precipitates start from coherent precipitates, they are metastable, and are coherent with the matrix on one lattice plane; these precipitates are usually present as plates and grow following the ledge mechanism. Incoherent precipitates are typically stable equilibrium phases that have a crystal structure different from the matrix.

2.2.2 Second Phase Nucleation and Growth

Formation of second phases in the solid state takes place by diffusional nucleation followed by growth [30]. Nucleation can be either homogeneous or heterogeneous depending on the matrix condition where precipitation is taking place.

For homogeneous nucleation, the total free energy change will depend on three main components: the change in the interfacial energy which destabilizes the nuclei, meaning that it takes energy to form an interface; the change in the volume free energy which relates the creation of a volume to a reduction in the volume free energy; and the change in the strain energy which originates from the misfit between the matrix and the new volume formed. The balance between these three components gives rise to a free energy threshold with a critical nucleus where the nuclei radius will shrink if it is below the critical nucleus radius and it will grow if it is above this value in order to reduce the total free energy of the system. The following expression summarizes the free energy change in homogeneous nucleation [30]:

$$\Delta G = -V\Delta G_v + A\gamma + V\Delta G_s \quad \textbf{Equation 2.8}$$

where ΔG is the free energy change, V is the volume of the second phase formed, ΔG_v is the volume free energy reduction, A is the area of the interface area created, and ΔG_s is the strain energy that will depend on the second phase particle coherency with respect to the matrix.

In heterogeneous nucleation, the energy required for nucleation is reduced by the presence of defects in the matrix such as free surfaces, grain boundaries, interphase borders, stacking faults, dislocations and vacancies. These defects are also called nucleation sites. The free energy change in heterogeneous nucleation can be expressed by the following equation:

$$\Delta G = -V(\Delta G_v - \Delta G_s) + A\gamma - \Delta G_d \qquad \textbf{Equation 2.9}$$

which basically consist on the same expression as Equation 2.8 except that the term ΔG_d has been added to the energy system representing the reduction in the activation energy barrier for nucleation due to the presence of defects (or nucleation sites). In practice, heterogeneous nucleation is more likely to occur under high temperature heat treatment processes.

As a continuation of the nucleation process, particle growth will follow and this mechanism will depend mostly on the mobility of the interfaces precipitate/matrix and the precipitate type (coherent, semi-coherent, or incoherent.)

2.2.3 Second Phase Particle Coarsening

After nucleation and growth, secondary particles can coarsen at the expense of other surrounding smaller particles of the same phase separated by a matrix; this process is

known as Oswald Ripening and it is relevant for the understanding of grain size control mechanisms specially when dealing with high temperature precipitation in austenite [11] since this effect can cause the particles to be ineffective in terms of grain refinement capabilities. The reduction of the interfacial energy between the particles and the matrix is the main driving force for coarsening. The kinetic analysis for this process is given by the Gibbs-Thomson equation which relates the local solubility at the second particle-matrix interface with the size of the particle:

$$C_r = C_e\left(1 + \frac{2\gamma V_m}{RTr}\right) \quad \textbf{Equation 2.10}$$

where C_r is the equilibrium concentration of the matrix α with a second particle of radius r, C_e is the matrix composition in equilibrium with a large radius, V_m is the molar volume of the second particle, R is the gas constant, and T is the absolute temperature. The Gibbs-Thomson relationship provides an understanding of the concentration gradient that will exist in the matrix between two precipitates of different sizes that will lead to a diffusional flow and cause the large particle to grow at the expense of the smaller one.

The rate of coarsening behavior of precipitates in microalloyed steels will depend on the diffusion of the microalloying solute in the matrix and the diffusion mechanism that is dominant. This diffusion mechanism can be bulk-controlled, direct precipitation or interphase-controlled, or grain boundary diffusion.

The bulk diffusion control mechanism will be used in subsequent chapters and it is well described by the simplified equation of Lifshitz, Slyozov, and Wagner [10, 11] that relates the diffusion flux in equilibrium from a supersaturated infinite medium C^*, to the

concentration C_r at a precipitate of radius r (Zener's approximation). The prediction of particle growth is then obtained by the following expression:

$$r^3 - r_0^3 = \frac{8\sigma V_m D t C}{9RT} \qquad \textbf{Equation 2.11}$$

where r is the final precipitate radius, r_0 is the initial precipitate radius, σ is the interfacial energy, V_m is the molar volume of the precipitate, D is the diffusion coefficient of the microalloying solute in the matrix, t is the time for coarsening, C is the concentration of solute in solid solution, R is the universal gas constant and T is the absolute temperature. Equation 2.11 is therefore useful for the estimation of second phase particle coarsening in a solid matrix.

2.2.4 Austenite Grain Size Prediction Models for Microalloyed Steels

At the beginning of section 2.2, Beck's equation was introduced as a way to predict the general kinetics of isothermal grain growth by means of a time exponent and rate constant determined by the temperature and the alloy composition. For the microalloyed steels case, several prediction models for austenite grain growth are available in the literature and the majority of them take into account the grain growth inhibition or retardation by the presence of secondary phase particles, also known as Zener drag effect [11].

The approach used by Zener was based on the determination of a critical grain size diameter whose driving force for growth would be balanced by the pinning force exerted by secondary stable particles. Through the effect of stable particles (assumed spherical in shape), the grain size in equilibrium can be correlated to the volume fraction of the second particles, and the particle radius, leading to the well-known Smith-Zener equation:

$$D_{cr} = \frac{8r}{3f} \qquad \textbf{Equation 2.12}$$

where D_{cr} is the critical diameter, r is the mean particle radius and f is the particle volume fraction. From this expression, several modified versions have been proposed by different researchers. These new versions are essentially based on the interaction between the particles and the grain boundaries. One of these modifications is the Gladman expression [31] which considers particle coarsening due to coalescence and energy changes related to the growth of tetrakaidecahedral large grains surrounded by smaller tetrakaidecahedral grains. For such approach, unpinning of grains occurs when particles reach a critical value (onset of abnormal grain growth):

$$D_{cr} = \frac{\pi}{3}\left[\frac{3}{2} - \frac{2}{Z}\right] \cdot \frac{r}{f} \qquad \textbf{Equation 2.13}$$

where Z is the Zener coefficient that usually goes from 1.41 to 2.00 and can be fit based on experimental data. Table 2.3 gives a summary of different models available in the literature for austenite grain growth behavior prediction.

Table 2.3. Summary of grain growth models available in the literature

Author	Model	Definitions	Criteria / Comments
Beck [18]	$D^n - D_0^n = C \cdot t$	D=mean grain diameter D_0=initial grain size C=rate constant n=time exponent t=time	Kinetics of isothermal grain growth where n and C can be determined based on material and temperature.
Hillert [3]	$D_{cr} = \frac{8r}{3f^{0.93}}$	D_{cr}=equilibrium grain size r=particle mean radius f=particle volume fraction	Expression for three dimensional systems, recommended for small values of f.
Nishizawa et al. [32]	$D_{cr} = \frac{8}{3}\frac{r}{f^{2/3}}$	D_{cr}=equilibrium grain size r=particle mean radius f=particle volume fraction	High C, high Mn steel in 3 dimension. An exponent value of 0.5 for the volume fraction in 2D case is recommended.
Rios [33]	$D_{cr} = \frac{r}{3f}$	D_{cr}=equilibrium grain size r=particle mean radius f=particle volume fraction	Particles coarsen and then dissolve.
Moon et al. [7]	$\frac{dD}{dt} = nK\left[\frac{1}{D} - \frac{1}{Z}\frac{f}{r}\right]^{(1/n)-1}$	D=mean grain size n=time exponent K=rate constant Z=Zener coefficient r=particle mean radius f=particle volume fraction	*Based on Beck's equation (requires $D>3D_0$) by differentiation and analyzing isothermal grain growth data (additive rule). *Considers pinning effect of secondary particles and solute drag effect through the rate constant K. *Meant for welding thermal cycles. *This model requires knowledge of the isothermal austenite grain growth rate.

In many of these models an experimental value of the mean austenite grain size, an estimated initial second particle size and an estimation of the solute concentration in solution through the solubility product would be enough to predict the austenite grain coarsening behavior of a particular microalloyed steel and for some cases the mechanical properties of the material. The main limitation of these models is that they rely on

isothermal holding conditions and because of the complexity of precipitation processes under different heating practices, there has not been universal agreement on experimental results for a single proposed model.

2.2.5 Estimation of Pinning Force and Driving Force for Grain Growth

Grain boundary pinning by secondary particles occurs when a grain boundary intersects a particle and consequently an area of the boundary disappears. As the grain boundary is distorted by the presence of the particle, its surface energy is increased, requiring additional work, and allowing eventually to become unpinned [11]. Zener provided a general form for the pinning force exerted by a single spherical particle of radius r as follows:

$$p = \pi r \gamma \qquad \textbf{Equation 2.14}$$

where p is the force required for boundary unpinning, and γ is the boundary surface energy per unit area. The pinning force for a certain number of pinning particles can be obtained by the following expression:

$$F_{pin} = p \cdot N_a \qquad \textbf{Equation 2.15}$$

where F_{pin} is the pinning force per unit area of the grain boundary and N_a is the number of particles per unit area. The different models available in the literature follow this pinning model proposed by Zener and their differences consist essentially in the way the number of particles per unit area (N_a in Equation 2.15) is calculated. Table 2.4 presents a summary of the different models and their criteria for the calculation of the number of particles per unit area N_a, where r is the mean particle radius and f is the volume fraction of the particles.

Table 2.4. Summary of models for the estimation of pinning forces

Model	Equation	Criteria for calculation of N_a
Gladman [11]	$P_G = \frac{3f\gamma}{2r}$ **Equation 2.16**	Particles randomly distributed and their center lying within a distance $+r$ to $-r$ from the boundary.
Rigid Boundary [34]	$P_R = \frac{6f\gamma}{\pi r}$ **Equation 2.17**	The grain boundary can only interact with particles lying between $\pm$r of the boundary plane.
Flexible Boundary [21, 34]	$P_F = \frac{3\gamma f^{2/3}}{\pi r}$ **Equation 2.18**	The grain boundary can be in contact with every particle within a single plane in a 3D array until complete pinning.

Moreover, the driving forces for grain growth are determined by the surface energy in the boundaries. Table 2.5 presents the models for grain growth considering energy changes in the surface area of grains.

Table 2.5. Summary of models for the calculation of driving forces for grain growth

Model	Equation	Criteria
Zener [11]	$F_Z = \frac{2\gamma}{R}$ **Equation 2.19**	Continuous grain growth. γ is the interfacial energy, and R the radius of curvature.
Gladman [26]	$F_G = \left(\frac{2}{Z} - \frac{3}{2}\right)\frac{\gamma}{R_0}$ **Equation 2.20**	Growth of a large tetrakaidecahedral. Z is equal to R/R_0 and when greater than 4/3 the force is negative and grain growth proceeds. R is the radius of a grain that might grow, R_0 is the grain size of the system
Hillert [11]	$F_H = k\left(\frac{1}{R} - \frac{1}{R_c}\right)$ **Equation 2.21**	R is the radius of curvature of the grain boundary, R_c a critical grain radius and k a constant.

2.3 SEAMLESS LINE PIPE STEEL GRADE MANUFACTURING

Since the last 30 years, the manufacturing of high-end seamless line pipe steel has been demanding higher strength microstructures, better fracture toughness properties, and good weldability for their use in the oil and gas production in both onshore and offshore operations under harsh conditions. This has been possible to attain in one part by the introduction of MAE technology in combination with the use of lower carbon content levels, and modern controlled processing mills [35].

Seamless line pipe steel grades are obtained by piercing a reheated steel bar, followed by an elongating and sizing process to form the mother pipe (as-rolled pipe) with the dimensions specified by the customer. The layout and technology can vary depending on the type of rolling mill. High-end API 5L seamless pipe grades (i.e. X65-X100) for more demanding applications need a heat treatment to attain the mechanical properties

required. Higher strength line pipe grades are required for reducing cost by manufacturing thinner pipe walls (better transportation efficiency) and for increasing the operating pressure.

The heat treatment of as-rolled seamless line pipes consist of austenitizing to a temperature above Ac3 (usually 900-920°C), followed by quenching in water media and subsequent tempering treatment at a temperature below Ac1 (below ~720°C). Depending on the alloying and microalloying composition, as well as the quenching technology, the resulting microstructures are usually mixtures of bainite, ferrite, and low-carbon martensite in different proportions giving a good balance of tensile and toughness properties.

Moreover, steel seamless line pipe grades (in the as-quenched and tempered condition) will undergo thermal cycles during onshore and offshore stringent operative welding conditions in which the parent material is subjected to high peak temperatures in a short period of time, leading to a Heat Affected Zone (HAZ) and more specifically to a coarse-grained heat affected zone (CGHAZ) near the fusion line as a result of high heating inputs used in welding procedures.

2.4 AUSTENITE GRAIN COARSENING MECANISMS DURING WELDING PROCESSES

Based on what has been described in previous sections, it is anticipated that grain coarsening temperature and the type of microalloying concentration are the major factors that will determine the particle dissolution process in the system and consequently the

austenite grain coarsening behavior. There are many manufacturing processes, operative conditions, and applications where microalloyed low carbon steel products are exposed to different thermal cycles in which austenite grain growth can take place and the coarsening or controlling mechanisms can be determined by the precipitate behavior under such thermal conditions.

It has been concluded by many authors that Ti microalloying in appropriate contents has a beneficial effect in terms of final toughness properties by grain boundary pinning effect of stable secondary particles that prevent grain boundary motion during heat treatment cycles [36] similar to the stringent operative welding conditions. The main issues that arise during welding procedures is the non-isothermal nature of the thermal cycles which means that the estimation of the grain coarsening behavior assuming particle coarsening and/or dissolution can be quite challenging. While in isothermal heating one can assume steady state conditions, in welding processes, the temperature-time profile plays an important role in the behavior of the precipitation stability. In addition, after high peak temperatures, material may undergo re-precipitation during the cooling stage [37, 38].

Some of the main mechanisms for improvements of the HAZ microstructure discussed in the literature that have general consensus are as follows:

(1) Thermal stability of titanium nitrides or titanium oxides well distributed in the matrix cause effective pinning and refines the ferrite grains in the HAZ microstructure.

(2) Pure titanium nitrides and oxides uniformly dispersed in austenite can act as nucleation sites for the formation of acicular ferrite during the cooling stage of the welding thermal cycle, therefore improving toughness properties.

There have been other studies that show the effect of the coherency of precipitates in the effectiveness of exerting pinning force on grain boundary mobility [39].

In their review [40] from 2006 about non-isothermal grain growth in metals and alloys, Mishra and DebRoy provide a comprehensive and useful summary on special grain growth features that are characteristic from processes that experience spatial and temporal temperature variations. They conclude that most of the research needs in this matter still require a better understanding of the coarsening and dissolution behavior of precipitates and a good correlation with the evolution of the grain structure.

Banerjee et al. present a good example of austenite grain growth in X80 line pipe steel through the study of the precipitate dissolution evolution for thermal cycles typical of the heat affected zone [22]. One of the interesting observations was that for heating rates higher than 100°C/s the austenite grain size is a function of the peak temperature and independent of the heating rate applied. They conclude that precipitate stability and grain boundary mobility analyses are the aspects that provide an understanding of grain coarsening behavior in the HAZ and that up until now it has been difficult to observe them separately.

Table 2.6 gives some examples of the energy input ranges involved for different welding processes while Figure 2.2 provides an example of TiN precipitates coarsening as a function of welding heat input energy and corresponding peak temperature in the heating cycle. Figure 2.3 illustrates the microstructural changes that occur at the HAZ of a low carbon steel weld and its correlation with the Fe-Fe_3C phase diagram.

Table 2.6. Typical heat-input ranges related to welding processes [38]

Welding Process	Approximate energy-input range (kJ/mm)
Submerged Arc	1.0-10
Gas-Metal Arc	0.5-3.0
Manual Metal Arc	0.5-3.0
Gas-Tungsten Arc	0.3-1.5
Electron beam	0.1-0.6
Laser beam	0.1-0.6

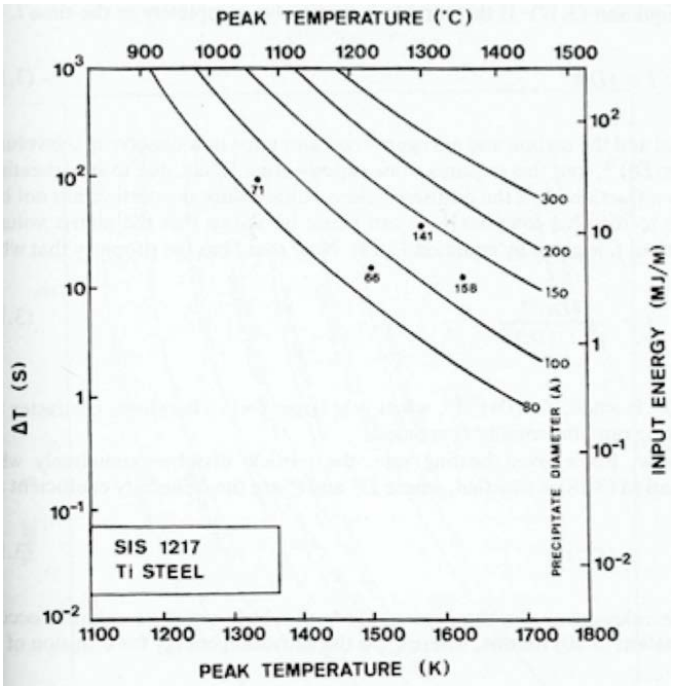

Figure 2.2. Theoretical graph of TiN coarsening as a function of welding heat input energy and peak temperature in the HAZ. Points refer to experimental values [38]

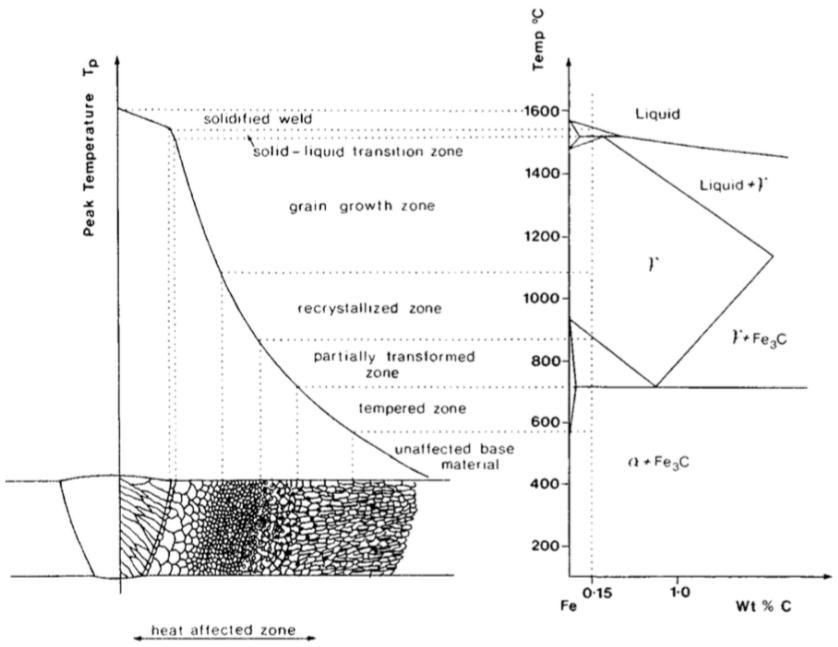

Figure 2.3. Scheme of microstructural changes in the HAZ in a low carbon steel weld [38]

There are some considerations that have to be taken into account when dealing with thermal cycles characteristic of a welding process, for instance, the solubility products previously presented in Table 2.1 do not generally apply since equilibrium will not be reached at the heating rate and this will therefore impact the pinning force exerted against the grain growth forces [38, 41]. Particles can consequently undergo either a mix of incomplete dissolution and coarsening, or complete dissolution during a welding thermal cycle.

Additionally, under these conditions, the particle coarsening will now depend on both the temperature and time and a modified version of Ostwald ripening theory (Equation 2.11) shall be used. The following resulting relationship has been used for estimating the precipitate coarsening during a welding thermal cycle [38]:

$$r^3\text{-}r_0^3 = \int_0^{\infty} \frac{A}{T(t)} e^{-\left(\frac{Q_v}{R \cdot T(t)}\right)} dt \quad \textbf{Equation 2.22}$$

where r and r_0 are the initial and actual precipitate radius, respectively, A is a constant that depends on the alloy system, Q_v is the activation energy for bulk diffusion, R is the gas constant, and $T(t)$ is the thermal profile.

An important implication to consider during welding cycles is the superheating effect of the ferrite before the transformation to austenite due to the high heating rates involved in the process [38]. Furthermore, another phenomenon that is likely to occur due to high heating rates is the dissolution of carbides (i.e. cementite) at a much greater temperature than estimated.

There has also been suggested that resulting deformation due to strains from reverse martensitic transformation accelerates the process of completion of the $\alpha \rightarrow \gamma$ phase transformation and grain coarsening in the heat affected zone [41]. It is therefore assumed that the solubility products previously presented (Table 2.1 and Table 2.2) must be modified taking into account that precipitates will not dissolve completely or at least they will do so at a higher temperature than the expected. The fraction of particle dissolved f considering superheating can be obtained by the following expression [38]:

$$f = \frac{1}{1+\left[\frac{t^*}{t} e^{-\frac{Q_v}{R}\left(\frac{1}{T^*}-\frac{1}{T}\right)}\right]^{3/2}} \quad \textbf{Equation 2.23}$$

where t^* is the time for complete dissolution at a temperature T^*, Q_v is the activation energy for bulk diffusion and R is the gas constant. Based on Equation 2.23, the temperature for full dissolution T_s can be obtained by the following relationship:

$$T_S = \frac{B}{A\text{-}log\left(\frac{[C_M]^a[C_X]^b}{f^{a+b}}\right)}$$ **Equation 2.24**

where A and B are the solubility product constants given in Tables 2.1 and 2.2, C_M and C_X are the concentrations of the carbide or nitride former and the interstitial element, respectively, and a and b are the stoichiometric constants of the compound.

Figure 2.4 depicts a times of complete dissolution of different carbides and nitrides in austenite as a function of peak temperature.

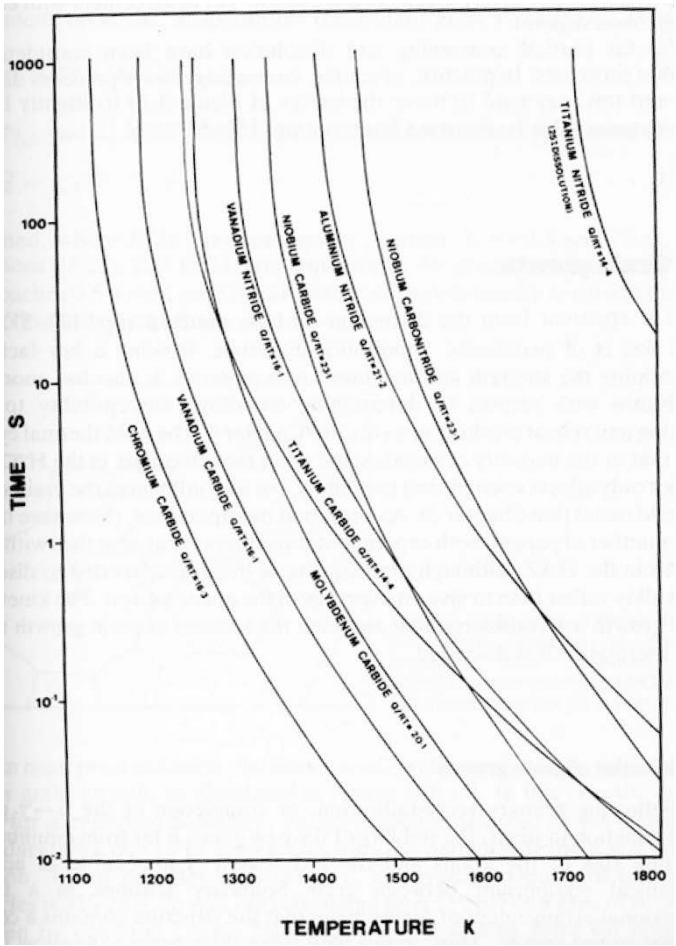

Figure 2.4. Times of complete dissolution for different nitrides and carbides in austenite [38]

2.5 EFFECT OF TI:N RATIO ON THE AUSTENITE GRAIN COARSENING

In Ti-bearing steels, dispersed TiN precipitates are expected to show stability in austenite under both isothermal heat treatments at high temperature and welding thermal cycles. The addition of appropriate levels of Ti and N are of relevance in the understanding of the stability of nitrides formed throughout the different processes and the potential interaction with other nitride or carbide formers such as Al, V, Nb, and Zr [38, 42] by mutual or exclusive mutual solubility. The ratio of Ti to N concentration in Ti-bearing steel designs, as well as its closeness to the stoichiometric equilibrium ratio 3.42, has been widely used as a reference in different works for the determination of optimum levels of these two elements in the alloy design. The stoichiometric ratio of 3.42 is the proportion of relative atomic weights of Ti and N (48 and 14, respectively) that react and form titanium nitride (TiN.) The present section includes a description of some information available in the literature with respect to the observations and potential effect of the Titanium to Nitrogen ratio on the austenite grain size control. In addition, the next section includes a review of works related to the effect of Ti/N ratio on some mechanical properties such as hardness, toughness and tensile properties, as a consequence of Ti or N available as precipitate or in solid solution.

Back in 1989 Wang published the results of a systematic study of the effect of different nitrogen content levels on a series of Ti-microalloyed systems on the austenite grain coarsening behavior simulating reheating processes with temperature ranging from 950°C to 1260°C [9]. Ti/N values for a series of laboratory heats varied from 0 (Ti-Free) up to 8.5 depending on both the titanium and nitrogen content. The main conclusion of this

study was that higher austenite grain coarsening temperature (onset of mixed grain structure) is obtained with Ti/N ratio near the stoichiometric value of 3.42; moreover, the increase in nitrogen content (nitrogen in excess) results in an increase on the volume fraction of TiN precipitates, while the increase in Ti content (titanium in excess) increases the particle size leading to a lower grain coarsening temperature.

Medina et al. present interesting results in their work related to the influence of Ti and N contents effect on the precipitate size distribution and grain coarsening behavior in structural steels [10]. A noticeable observation in their results was that one of the alloy systems reheated at 1300°C did not show the austenite grain size expected based on the Ti/N ratio (see Figure 2.3) and they suggest that the reason behind that behavior was the insufficient Ti content as precipitate (volume fraction of TiN) at that particular temperature compared to other Ti-bearing system included in their study with even higher Ti/N ratio.

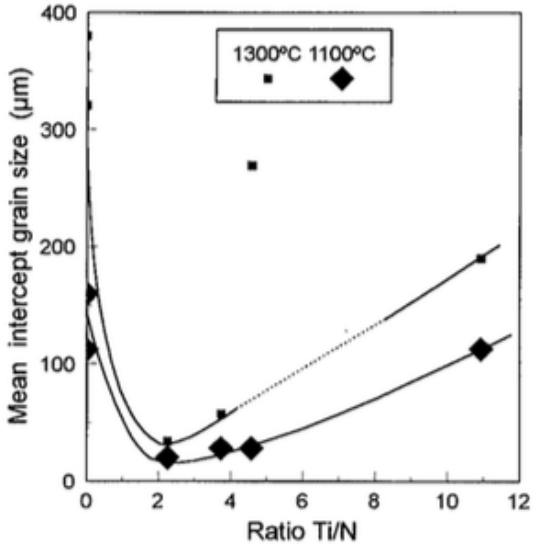

Figure 2.5. Austenite grain size vs Ti/N ratio at 1100°C and 1300°C, 10 min soaking [10]

In their work about the effect of Ti microalloying content on pinning force exerted by stable TiN precipitates against recrystallization driving forces, M.I. Vega et al. conclude that under hypo-stoichiometric conditions grain growth control is effectively obtained at temperatures around 1300°C where a fine distribution of TiN precipitates was observed in the matrix [21].

Liu and Liao [39] concluded that HAZ microstructure and properties obtained in their experimental Ti-V microalloyed steels were determined by the volume fraction, size distribution and thermal stability of the precipitates by affecting both the austenite grain size and the subsequent phase transformations. They also conclude that nitrogen-enhanced Ti-V microalloyed systems can exhibit stable TiN precipitates at temperatures even above 1350°C. Another important conclusion was that grain boundary precipitation on nitrogen-enhanced systems was also responsible on the control of TiN coarsening behavior for short holding times at the peak temperature. These observations strongly suggest that hypo-stoichiometric Ti/N ratios are more effective to control the grain coarsening behavior of austenite.

Table 2.7. Summary of main findings in the literature related to Ti/N ratio influence on AGS

Author(s)	Alloy systems studied	Thermal Cycles applied	Experimental Approach	Main findings
Medina et al. [10]	Low-C steels with variations in Ti (0-0.047 Wt%) and N (40-83 ppm)	Isothermals at 1100°C and 1300°C for 10 min	AGS measurements TEM- precipitate size distributions TiN volume fraction estimations	*Ti/N close to 2 is observed to be the optimal for AGS control. *Minimum value of Ti, close to 0.010 wt% for AGS control is necessary. LSW equation for controlled diffusion (Equation 2.11) shows good agreement with results.
Wang [9]	Low-C steels with variation in Ti (0-0.042 wt%) and n 26-65 ppm)	Isothermals from 950°C to1260°C for 90 min.	AGS measurements TEM-precipitate size distribution (carbon replica method)	*Highest grain coarsening temperatures are observed around the Ti/N stoichiometric ratio of 3.42. Beyond that value, grain coarsening temperature decreases. *Results suggest that conditions with higher Ti/N ratio extend the temperature range of mixed grain structure.
Liu et al. [39]	2 low-C Ti-V microalloyed systems (Ti=0.01%wt, V=0.08%wt), one with low N (30 ppm) and the other N-enhanced (130ppm). Material processed through recrystallization controlled rolling and accelerated cooling.	Gleeble 1500 CGHAZ simulations: Heating rate of 200°C/s to 820°C, 1050°C, 1200°C, and 1350°C for 2, 15, 35, and 60 s. followed by severe quenching	AGS Measurements TEM precipitate size distribution (carbon replica method)	*N-enhanced steels showed finer AGS. Charpy Transition temperature in the initial state is slightly higher than the low-N steel. *Fine TiN particles were observed in the N-enhanced steel which is considered to have been effective in the AGS pinning. *Hyperstoichiometric N/Ti conditions are effective in retarding Austenite Grain coarsening at high temperatures simulating CGHAZ *Grain-boundary-assisted diffusion was responsible of the coarsening of TiN along the austenite grain boundaries.

While several information can be found related to austenite grain coarsening behavior under isothermal conditions and its correlation with precipitate stability, there is still few studies that specifically explore the role of the stability precipitates under high heating rates and Ti/N stoichiometric conditions.

2.6 EFFECT OF TI:N RATIO ON MECHANICAL PROPERTIES

Several authors have studied the effect of Ti/N ratio of microalloyed designs on the final mechanical properties, in particular toughness. In a study conducted by Yan et al. on low carbon microalloyed steels with Boron added, they analyzed the effect of the Ti/N ratio (2.44, 3.5, and 4.2) in the formation of coarse TiN precipitates that are considered to be the reason of low toughness properties in this type of materials [43]. Some of their main observations were that in the first place, the average prior austenite grain size appeared to be similar in all three alloys after thermomechanical processing; second, the charpy V-notch impact toughness at -20°C, however, was significantly lower in the alloy design with the higher Ti/N ratio compared to the Ti/N ratio of 2.44. Based on post-mortem scanning electron microscopy analysis conducted on the charpy specimens, they conclude that coarse TiN particles were responsible of the inferior impact toughness properties on the high Ti/N ratio alloy designs, and considered that the martensite-austenite (M-A) micro constituents [44] did not play any role in this decreased material performance. They conclude therefore that a Ti/N ratio above stoichiometry results in a faster TiN coarsening rate. In another work conducted previously by Shen and Hansen [45] on similar alloy compositions with variation in the Ti/N ratio, they conclude that Ti in excess provides an increase in hardenability during quenching and an increase in tensile strength after tempering due to precipitation of Ti carbo-nitrides. They also conclude that coarse TiN particles are responsible for toughness reduction and that the number of these coarse TiN particles can be increased linearly by increasing the product of Ti and N concentrations in the steel composition. It is important to mention that in the previous two studies the main

reason of Ti addition in the alloy composition was the protection of BN formation (which reduces the boron hardenability effect) by tying the nitrogen with the Ti and leaving this way all boron available in solid solution or borocarbides that are soluble during austenitization. It is also important to mention that in the study conducted by Shen et al. details of the thermomechanical processing were not defined. It is well-known that the combined effect of TiN precipitates and microstructural conditioning are both responsible for the impact toughness behavior.

2.7 EFFECT OF INITIAL CONDITION ON THE AUSTENITE GRAIN COARSENING

There is a dearth of information available in the literature specifically dedicated to the exploration of the effect of initial condition of the material (i.e. as-cast, as-rolled, thermomechanical process, as-normalized, or quenched and tempered) on the austenite grain size behavior of microalloyed low-carbon steels. In most of the prediction models developed after experimental work, the initial state of the microstructure is usually neglected or its effect is assumed to be insignificant at the heat treatment conditions involved in the study, in particular if high temperature and holding times are involved. Some of the austenite grain coarsening estimations taken in different works assume an initial austenite grain size diameter, (typically between 10 to 20 μm) and, when microalloying elements are present, they estimate an initial homogeneous size of the possible thermodynamically stable precipitates [46].

Uhm et al. presented a work [47] in which they account for the effect of initial microstructure in the austenite grain growth behavior at different isothermal temperatures (from 900°C to 1300°C) by producing experimental alloy compositions with variations on alloying elements (Mn, Ni, Cr) leading to different initial microstructures after forging and normalizing at 950°C for one hour. Their main findings were that the time exponent *n* (see Equation 2.1) remained constant regardless of the isothermal temperature, and the activation energy for grain coarsening increases with the addition of alloying elements. On the other hand, austenite grain size predictions presented good agreement with respect to experimental values from high isothermal temperatures, whereas calculation of AGS for lower temperatures showed poor agreement and it was considered to be due to the underestimation of the effect of initial grain size.

Another more recent work conducted by Enloe et al. [48] analyzes the effect of the thermal history on precipitate evolution and subsequent austenite grain size behavior in carburizing steels with combination of Mo and Nb. The main observations were that stabilization of precipitates before reheating at high temperatures decreased the bimodality of the precipitate size distribution, the coarsening due to capillarity effects, and delays the possible dissolution of fine precipitates. In addition, for some Nb and Mo combinations it was found that a process of sulutioning (holding at 1250°C for 10 minutes) avoids the presence of abnormal grain coarsening after an isothermal at 1100°C for 60 minutes.

2.8 GRAIN BOUNDARY CHARACTER DISTRIBUTION STUDIES

There are few studies available in the literature that explore the correlation between the coarsening or dissolution process of precipitates in steels with the type of grain boundary and consequently their role in the austenite grain coarsening behavior.

Recently, Tao et al. conducted a study on the role dissolution process of carbonitrides on austenite grain growth of high chromium ferritic steels. This study provides evidence that high energy grain boundaries with misorientations between 20° and 45° are responsible for the austenite grain coarsening behavior by playing a role in the unpinning of secondary particles [49]. Tao et al. observed through electron backscatter diffraction (EBSD) analysis that this range of mis-oriented grain boundaries decreased with increasing the holding time during isothermal treatments at 1070°C as NbN precipitates coarsen and become less effective in exerting pinning forces against grain growth boundary mobility. This observation was in agreement with arguments by Hayakama and Szpunar, from a study published back in 1996, in which they linked the role of these high energy grain boundary misorientation range (with high disordered structure) on grain boundary mobility and secondary recrystallization of electrical steels [50]. Tao et al. also observed through SEM analysis that coarse precipitates were frequently present inside large grains, which served as evidence that precipitation coarsening (and consequently unpinning) occurs at the high-energy boundaries by both Ostwald ripening and grain-boundary assisted diffusion mechanisms.

3.0 STATEMENT OF PURPOSE

Based on the lack of information on studies related to GBCD on the austenite grain control of microalloyed low-carbon steels, this work will be focused on the hypothesis that the unpinning mechanism for grain boundary mobility can be understood by the quantification of the type of GBCD and its correlation with the presence or absence of Ti-rich precipitates that exert pinning forces against driving forces for grain growth, allowing consequently to provide a new view of the kinetics of austenite grain-coarsening behavior in Ti-microalloyed low-carbon steels. The present project has therefore the following objectives:

Study the role of Ti microalloying in the formation of precipitates that play a role in exerting pinning forces for Austenite Grain Size Control under selected heat treatment conditions and thermal cycles.

Provide a new view of the role of GBCD during the dissolution process of stable TiN particles in Ti-bearing low-carbon steels. This part of the study will use EBSD analysis after selected isothermal holding treatments as well as microalloying solute concentration analysis in both the matrix and along the grain boundaries through Electron Probe Micro Analyzer technique.

4.0 EXPERIMENTAL APPROACH

4.1 ALLOY SYSTEMS

Three experimental heats were manufactured using a laboratory vacuum induction-melting furnace. Around 190 kg of each experimental heat were cast into approximately 7 1/8" square by around 28" long ingots. The final chemical composition of the experimental heats is shown in Table 4.1. The selection of the aimed Ti microalloying content in two of the three alloy systems was based on the stoichiometry of TiN particles in order to have a hypo-stoichiometric condition for which Ti/N ratio were below 3.42 (alloy system labeled as Ti29) and a hyper-stoichiometric case for which Ti/N ratio were above the stoichiometric value of 3.42 (alloy system labeled as Ti54). A third system without Ti microalloying addition was included in order to have evidence of the influence of Ti content and therefore validate the effect of the Ti-bearing alloys in the austenite grain size control and precipitation stability. The base chemical composition for the three systems corresponds to a low carbon V-microalloyed line pipe design aiming for X65 API steel grade after Quenching and Tempering.

Table 4.1. Chemical Composition in Weight % for the three experimental heats

Element (%Wt)	TiF	Ti29	Ti54
C	0.076	0.079	0.084
Mn	1.18	1.16	1.16
Si	0.27	0.26	0.26
P	0.012	0.013	0.011
S	<0.001	<0.001	<0.001
Ni	0.21	0.21	0.21
Cr	0.20	0.19	0.19
Mo	0.121	0.121	0.121
V	0.054	0.055	0.055
Ti	**<0.001**	**0.011**	**0.020**
Nb	0.001	0.001	0.001
Al	0.026	0.030	0.030
N	0.0041	0.0038	0.0037
Cu	0.121	0.121	0.120
Ceq	0.368	0.369	0.373
Pcm	0.177	0.179	0.183
Ti/N	**0**	**2.89**	**5.41**
Ti*N	**0**	**0.000042**	**0.000074**

As it can be observed in Table 4.1, the base composition includes alloying elements such as Mo, Cr, and Ni, that influence the phase transformation behavior of the material and have also an effect on the calculation of the Carbon Equivalent (*Ceq*) and Parameter of Crack Measurement (*Pcm*) based on API Standards, which are typically used as a reference of weldability and alloy content limit control for line pipe steel designs. Since the aimed value of the alloying elements was remained constant, the calculated *Ceq* and *Pcm* based on these equations are similar for the three alloy systems.

$$Ceq_{(IIW)} = C + \frac{Mn}{6} + \frac{(Cr+Mo+V)}{5} + \frac{(Ni+Cu)}{15} \qquad \textbf{Equation 4.1}$$

$$Ceq_{(pcm)} = C + \frac{Si}{60} + \frac{Mn}{20} + \frac{Cu}{20} + \frac{Ni}{60} + \frac{Cr}{20} + \frac{Mo}{15} + \frac{V}{10} + 5B \qquad \textbf{Equation 4.2}$$

4.2 MATERIAL PROCESSING – HOT ROLLING OF PLATES

All three experimental ingots were hot rolled to plates of 25.4 mm in thickness. The pass schedule used in the hot rolling process is presented in Table 4.2. The rolling schedule was selected so that it can be as close as possible to the industrial practice for a seamless steel pipe of a similar wall thickness. After reheating of slabs, the starting rolling temperature was of 1,150°C and all subsequent deformations were conducted at a temperature above Ar_3 followed by air-cooling to room temperature after the final pass.

Table 4.2. Pass Schedule for hot rolling of experimental ingots

Pass #	Deformation %	Thickness [mm]
0	**-**	181.0
1	15	153.8
2	15	130.8
3	20	104.6
4	25	78.5
5	25	58.8
6	35	38.2
7	33	25.4

Overall, the thermo-mechanical history of the plates was kept constant for all three experimental heats so as to minimize the potential initial variation of alloying concentration and second phase particle distribution.

4.3 PRIOR AUSTENITE GRAIN SIZE STUDY

A prior austenite grain size (PAGS) study was carried out on samples taken from the three experimental systems in order to correlate the austenite grain coarsening behavior observed at different reheating temperatures with the precipitate coarsening and dissolution, as well as solute drag mechanisms.

Specimens in dimensions 10 mm x 12 mm x 25 mm (Figure 4.1) were cut from the hot rolled plates and subjected to isothermal reheating conditions to the following temperatures: 900°C, 950°C, 1000°C, 1100°C, 1200°C, 1300°C, and 1350°C. Experiments were conducted in a SentroTech Laboratory Furnace capable of providing a heating rate between 5 and 10°C/s depending on the temperature set-up. The holding time selected for all reheating temperatures was of 30 minutes. Figure 4.2 shows some schematics of the thermal profiles used for this study. Heating curves were recorded for each thermal set-up with a Picolog TC-08 data logger and a type K thermocouple inserted in a dummy sample.

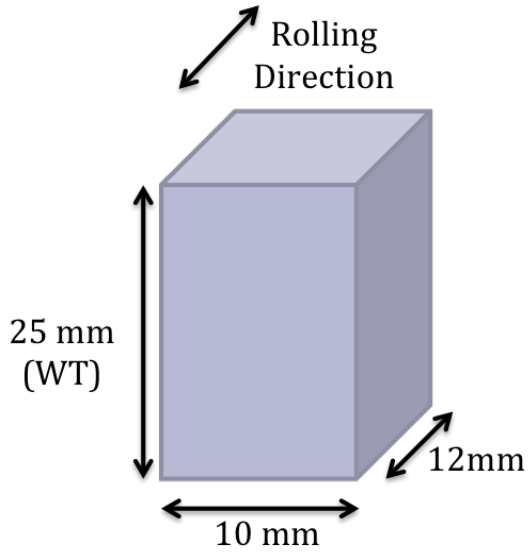

Figure 4.1. Dimensions of PAGS specimen

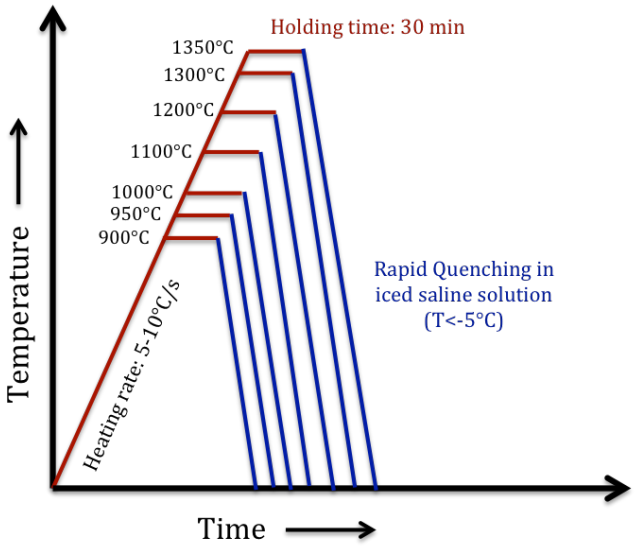

Figure 4.2. Schematics of the thermal cycles

Prior to each heat treatment, samples were encapsulated in quartz tubes back-filled with argon in order to limit the oxidation and decarburation due to oxygen and carbon diffusion during the heat treatment process. After 30 minutes of holding time at the desired reheating temperature, samples were subjected to quenching in an iced brine at a temperature below -10°C to guaranty full transformation of austenite grains into martensite and facilitate this way in revealing the grain boundaries. After quenching, samples were sectioned, mounted in Bakelite, and subjected to basic metallographic preparation for optical microscopy imaging.

In order to reveal the grain boundaries, all specimens were etched in a solution prepared with 100 mL of saturated aqueous picric solution, 4 g of sodium dodecylbenzene sulfonic acid (wetting agent) and 0.6 mL of HCl. The optimal etching temperature was 85°C and the etching time varied between 180 to 240 seconds depending on the heat treatment

condition of the sample. No tempering prior to etching was necessary for any specimen. Images of the resulting structure were obtained by optical microscopy at an appropriate magnification for the different reheating conditions. Image analysis for measuring the austenite grain size distribution was conducted using ImageJ software and at least 200 well-defined grains were measured by planimetric method based on ASTM E112 Standard; less than 200 grains were measured for conditions with an average grain diameter above 300 μm due to prepared surface availability on specimens.

Additional heat treatments were conducted at 1,200°C and 1,350°C on specimens from the three alloy systems that were previously subjected to an austenitization at 900°C with a soaking time of 10 min followed by water quenching and a tempering at 640°C with a 45-minute soaking time. These additional conditions were included to analyze the possible effect of the initial condition of the material (As-rolled vs. Quenched and Tempered) prior to reheating on the austenite grain coarsening behavior, particularly in the high temperature range.

In addition to the prior austenite grain size measurements, sections were obtained and prepared from selected PAGS samples for other analysis techniques such as EBSD, SEM, TEM, which are described in the following sections.

4.4 OPTICAL MICROSCOPY

Specimens for optical microscopy analysis from the different experimental works conducted in this project were subjected to basic metallographic by grinding with SiC

abrasive paper (320, 400, 600, 800 and 1,200 grit) followed by polishing with Alumina suspension (0.05 μm.) Optical microscopy analysis was conducted in a Keyence microscope equipment which has been mainly used for the following activities: prior austenite grain imaging for further size measurements; phase balance and ferrite grain size analysis in as-received condition; as-quenched, and quenched and tempered microstructural analysis; as well as preliminary microstructural assessment for different experimental conditions. Samples for PAGS study were etched with the solution described in section 4.3, whereas samples in as-rolled, quenched, and quenched and tempered conditions were etched with 3% nitric acid in ethanol (Nital) solution. Special coloring etchants such as Lepera reagent [51] and an etching solution of 3% Nital followed by 10% aqueous sodium metabisulfite [52] were used on selected samples for detailed multiphase microstructural analysis.

4.5 ELECTRON MICROSCOPY TECHNIQUES

4.5.1 Scanning Electron Microscopy

The main purpose of the scanning electron microscopy (SEM) technique was to obtain initial evidence of the presence of stable precipitates prior to the quantitative analysis at the TEM, in particular, the presence of TiN and other stable particles in both the hypo-stoichiometric and the hyper-stoichiometric alloy systems in the as-received condition, some selected temperatures from the PAGS study and the simulated high heating rate cycles. Specimens for SEM analysis were prepared by standard grinding and polishing

metallography. The analysis of specimens was conducted on a ZEISS Sigma 500 VP scanning electron microscope equipped with Oxford Aztec X-EDS and operating at a voltage between 10kV and 20kV depending on the interaction volume desired for the samples; both secondary electron and backscatter electron detectors were used during the analysis. Some of the samples were etched with 2% Nital solution to reveal microstructural features by secondary electron detection.

4.5.2 Electron Backscatter Diffraction (EBSD)

The main purpose of the EBSD technique was to analyze crystallographic characteristics and the grain boundary character distribution of the alloy systems under the different heat treatment cycles and its correlation with the presence of stable precipitates during the dissolution process and the type of grain boundary (misorientation) responsible of austenite growth mobility.

Specimens for EBSD analyses were prepared by standard grinding and polishing metallography followed by vibro-polishing in a VibroMet® polisher for 3 hours with 0.05 μm nanometer alumina suspension. EBSD analyses were conducted on a FEI Scios field emission gun scanning electron microscope equipped with an EBSD system. An accelerating voltage of 20kV with a beam current of 13nA, and a dwelling time of 200 ns were used as parameters for the data acquisition. Samples were tilted 70° to increase the signal detection of backscattered electrons diffracted. The scanned area and the step size varied from 30 μm x 30 μm up to 300 μm x 300 μm, and from 0.1 μm/step to 2 μm/step, respectively, depending on the desired scanned area and the average primary austenite

grain size previously observed on the samples. The hexagonal scan system was used for all the analyses as it provided a better delimitation of the grain boundaries compared to the squared scan system. After scanning, the data collected was processed by an Orientation Imaging Mapping (OIM) analysis software and data cleaning up routines for processing miss-indexed patterns included Confidence Index Standardization (CIS), grain dilation, and neighbor orientation correlation. The minimum rotation angle considered was of 2°.

In order to correlate the grain boundary character distribution during the dissolution process with the estimated and observed stable precipitates present in the matrix and grain boundaries, a systematic assessment has been done by combining the EBSD and the SEM analysis described in section 4.5.1. The same EBSD scanned areas were carefully tracked and analyzed by both secondary and backscattered electron detection.

4.5.3 Transmission Electron Microscopy with EDS analysis

Transmission electron microscopy analysis was conducted in a JEOL JEM2100F field emission gun equipment operating at 200 kV and equipped with and Energy Dispersive X-Ray (XEDS) detector. The main objective of the TEM analysis was to determine the size distribution, chemical composition and morphology of stable precipitates as well as other finer particles present in the matrix or grain boundaries in the as-rolled condition and under different thermal cycle conditions selected. Thin foils were prepared from material in the as-rolled condition, selected samples from PAGS study, and from the high heating rate thermal cycles at a location close to the mid-wall at a cross section perpendicular to the rolling direction of the plates.

Thin wafers around 0.5 mm in thickness were obtained from the material with a precision cutting machine followed by mechanical grinding to about a thickness between 70 and 140 μm. 3 mm diameter disks were then mechanically punched from the wafers and subjected to a dimpling grinder methodology with a Fischione Model 200 to guarantee the generation of a well-centered hole during subsequent electropolishing of the disk by reducing its thickness at the center down to 40-60 μm. Dimpled disks were then electro-polished with a Tenupol-5 twin jet polisher using a 5% perchloric acid and 95% ethanol solution electrolyte at a voltage around 20 V and a current between 25 μA and 30 μA at a temperature between -15°C and -20°C. Bright Field (BF) images for precipitate size distribution were taken at an appropriate magnification and ImageJ software was used for image analysis and measurements. Selected Area Diffraction Pattern (SADP) was also part of the TEM analysis for crystal structure determination and for obtaining evidence of finer particles present in the matrix.

4.5.4 Electron Probe Microanalyzer (EPMA)

Some samples prepared for systematic SEM and EBSD analysis were selected for an additional analysis of compositional distribution of microalloying content along specific grain boundaries in order to support the evidence of TiN precipitate dissolution and microalloying content available in solid solution. Wavelength-disperse method with crystal spectrometers was conducted in a JEOL JXA-8530F Electron probe microanalyzer. NIST standard reference material 1763a (low alloy steel) was used for the quantitative electron-probe line scans with a spot size of 1 μm diameter and a probe current of 20nA, an

operation voltage of 20kV and a dwelling time of 10 seconds for peak search and 5 seconds for background.

4.6 HIGH HEATING RATE CYCLES

The aim of this experimental work was to explore the stability of precipitates in the Ti-bearing systems under hypo-stoichiometric and hyper-stoichiometric conditions (Ti29 and Ti54 alloy systems respectively) when subjected to high heating rates that can simulate characteristic peak temperatures conditions of the Coarse Grain Heat Affected Zone (CGHAZ) on base material during welding procedures. The relevance of this experimental part relies on the fact that to a significant extent, the final performance of these alloy designs under welding thermal cycles is determined by the austenite grain size coarsening behavior across the HAZ and therefore the stability of the precipitates for the case of microalloyed low carbon steels [27, 39].

Specimens with dimensions 13 mm x 13 mm square x 90 mm long with the longitudinal dimension parallel to the rolling direction of the plate were obtained from the plates as illustrated in Figure 4.3. These specimens were subjected to an austenitizing at 900°C with 10 min soaking time followed by water quenching and a tempering at 640°C with a soaking time of 45 min in a laboratory furnace. After quenching and tempering heat treatment, specimens were milled to final dimensions of 11 mm x 11 mm square and 90 mm long.

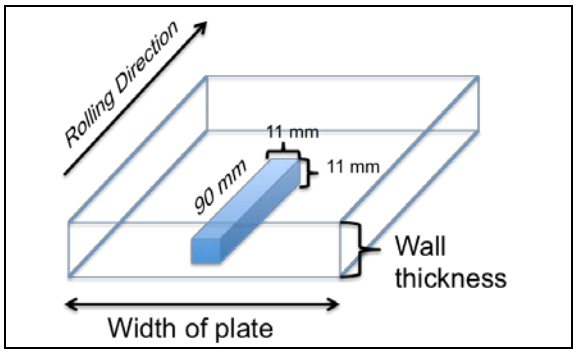

Figure 4.3. Location of specimens for welding cycle simulations on experimental plates

Thermal cycles were simulated by a Gleeble 3500 equipment following the profile presented in Figure 4.4 which describes a peak temperature of 1350°C followed by rapid water and air cooling to room temperature just after the peak temperature of 1350°C. Specimens were used for prior austenite grain size measurement following the preparation, etching and analysis methodology described in section 4.3; precipitation analysis following the sample preparation and analysis methodology described in section 4.5.3 was also conducted on this last sample.

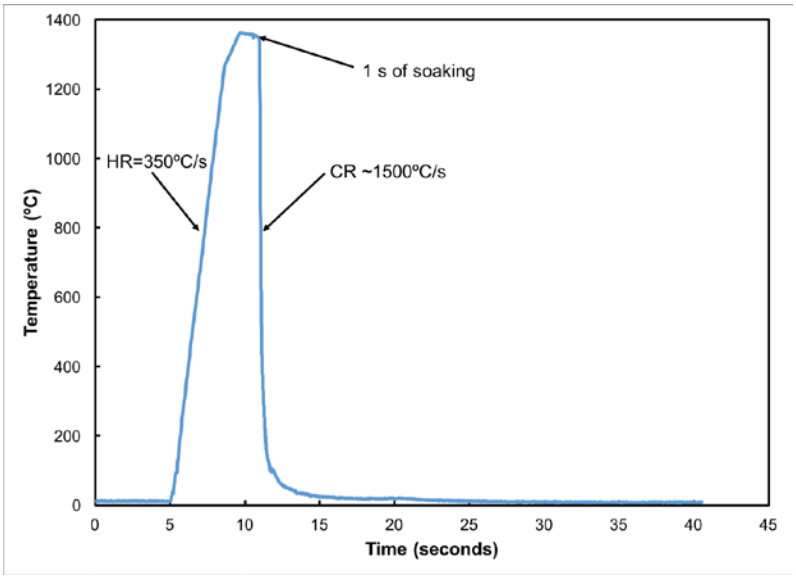

Figure 4.4. Thermal profile used for high heating rate effect on AGS

4.7 MECHANICAL TESTING

4.7.1 Hardness

Hardness Testing was conducted on samples from different experimental conditions in a LECO LM 800 microhardness tester with a load of 500 grams and 2 kg depending on the purpose of the test and a loading time of 15 seconds. The load used for hardness survey on as-rolled, as-quenched, and tempered material was of 2 kg; loads below 2 kg were employed on microhardness analysis for microstructural features observed on the samples.

4.7.2 Tensile Testing

In order to assess the tensile properties of the different material conditions and associate the potential effect of Ti additions effect on final properties, tensile testing was performed on material in as-rolled condition. Standard cylindrical tensile specimens with 12.7 mm of gauge diameter and a nominal gauge length of 50.8 mm were machined from plates according to ASTM E8/E8M-09 standard. Testing was performed in a MTS servohydraulic machine at a yielding rate of 11.5 MPa/s for Yield Point determination and at a straining rate of 25.4 mm/mm/min for ultimate tensile strength determination.

4.7.3 Charpy V-Notch Impact Testing

Impact toughness assessment was done on different sample conditions through machining of Charpy V-notch specimens. Standard Charpy V-notch specimens (10 mm x 10 mm square cross section x 55 mm in length) were prepared from material in the as-received condition and evaluated with the notch location at the transverse and longitudinal direction in sets of 3 specimens at a testing temperature of 0°C, -10°C, -20°C, -30°C, and -40°C.

5.0 RESULTS

5.1 MATERIAL CHARACTERIZATION IN THE AS-ROLLED CONDITION

Detailed analysis in the as-rolled (AR) condition of the alloy systems was considered critical for this study being the initial state that accounts for the potential dissolution and coarsening of stable precipitates during the different heating cycles which can be correlated to the pinning effect of the austenite grain boundaries. As mention in previous sections, the as hot-rolled condition of the material is the initial state of seamless line pipe steel grades before heat treatment and subsequent welding cycles.

5.1.1 Microstructural Analysis

Characteristic micrographs at the mid-wall location of the plates in the as-rolled condition for the three alloy systems are presented in Figure 5.1. Based on the microstructural analysis, TiF system developed a larger average ferrite grain size compared to the Ti-bearing systems Ti29 and Ti54. The phase balance for all three systems is constituted predominantly by ferrite and pearlite. Few iron carbides in the matrix were also observed through SEM analysis.

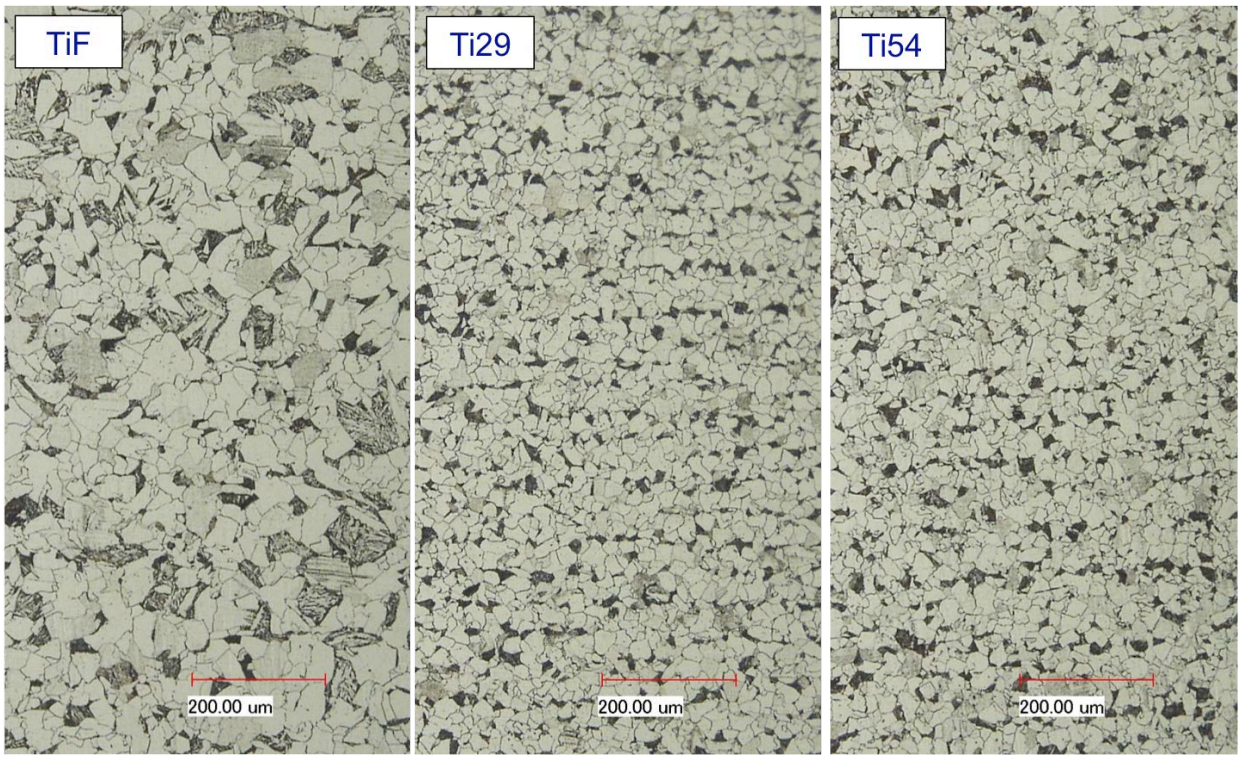

(a) (b) (c)

Figure 5.1. Characteristic Micrographs of the as-rolled condition for the alloy systems

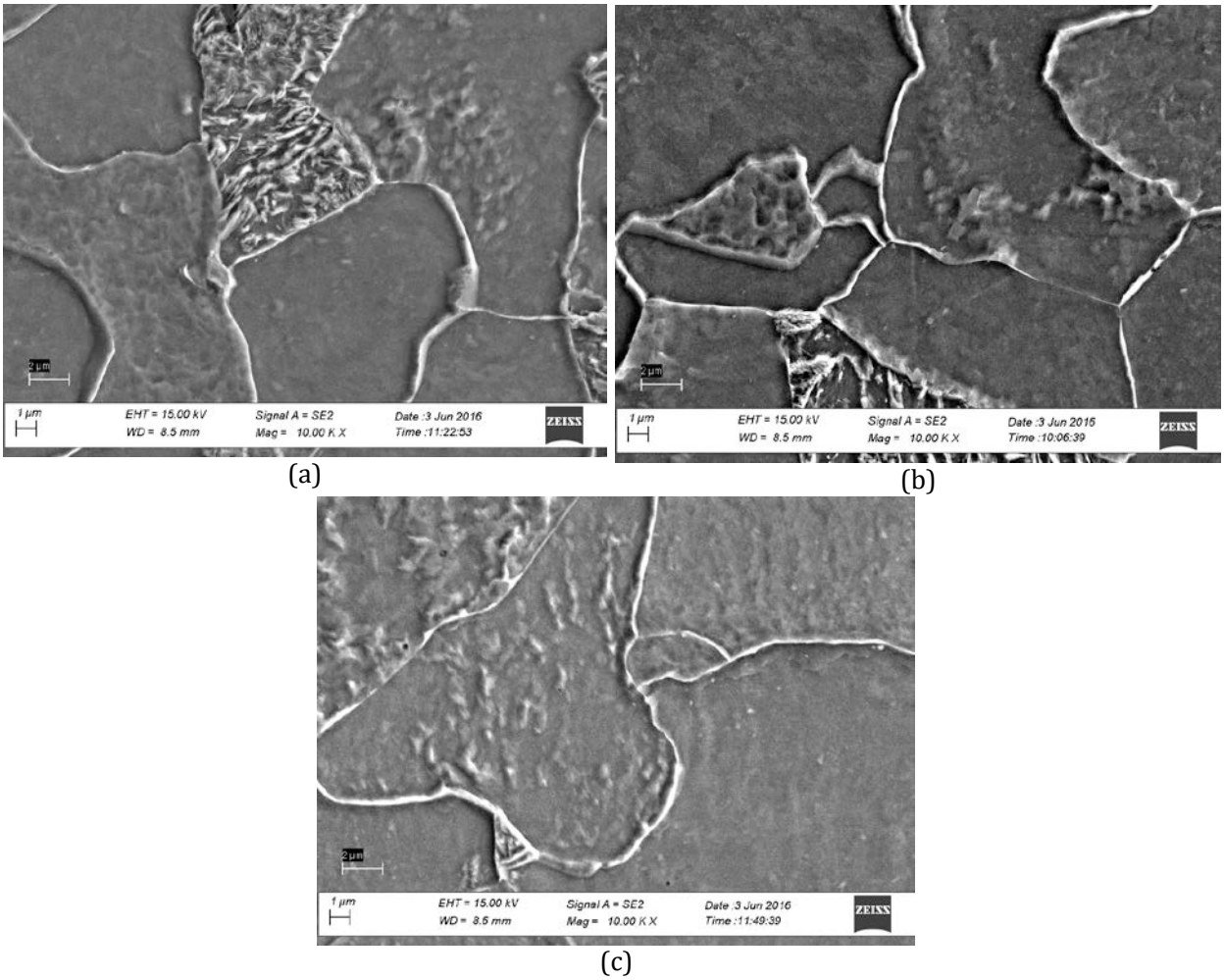

Figure 5.2. SEM micrographs in the as-rolled condition for (a) Ti29, (b) Ti54 and (c) TiF

5.1.2 Ferrite Grain Size

Table 5.1 presents the average ferrite grain size (equivalent diameter) for the three alloy systems in the as-rolled condition. Grain size measurements were done by optical microscopy and ImageJ analysis software as described in section 4.3. At least 200 grains were measured for each sample. For each alloy system measurements were done on two samples, one located at the center of the width of the plate and a the other at a location

near one of the edges of the width of the plate in order to attest the homogeneity of the microstructure across the transverse section of the plate.

Table 5.1. Results from ferrite grain size measurements on laboratory hot-rolled plates

Location across the width of plate	TiF				Ti29				Ti54			
	D avg (μm)	D min (μm)	D max (μm)	Std Dev	D avg (μm)	D min (μm)	Max (μm)	Std Dev	D avg (μm)	D min (μm)	D max (μm)	Std Dev
Edge	23.29	3.85	67.48	11.29	16.59	4.18	37.86	6.95	18.78	6.40	40.08	6.34
Center	24.43	6.34	63.04	12.02	19.26	5.87	41.21	8.02	19.85	5.60	45.50	7.71

As it can be observed in Table 5.1, a slightly higher ferrite grain size value was measured on the three alloy systems at the center of the width of the plate compared to the edge location. Nonetheless, it is clear the beneficial effect of Ti addition on the microstructural refinement of ferrite.

5.1.3 Precipitate Analysis – Initial State

A preliminary SEM analysis was done for obtaining evidence of precipitates in the initial state of the material (as-rolled condition). Figure 5.3 (a) and (b) depicts some examples of first evidence of coarse precipitates found on Ti-bearing samples etched with Nital 2%. TiN precipitates are encircled (dashed yellow lines) in the pictures.

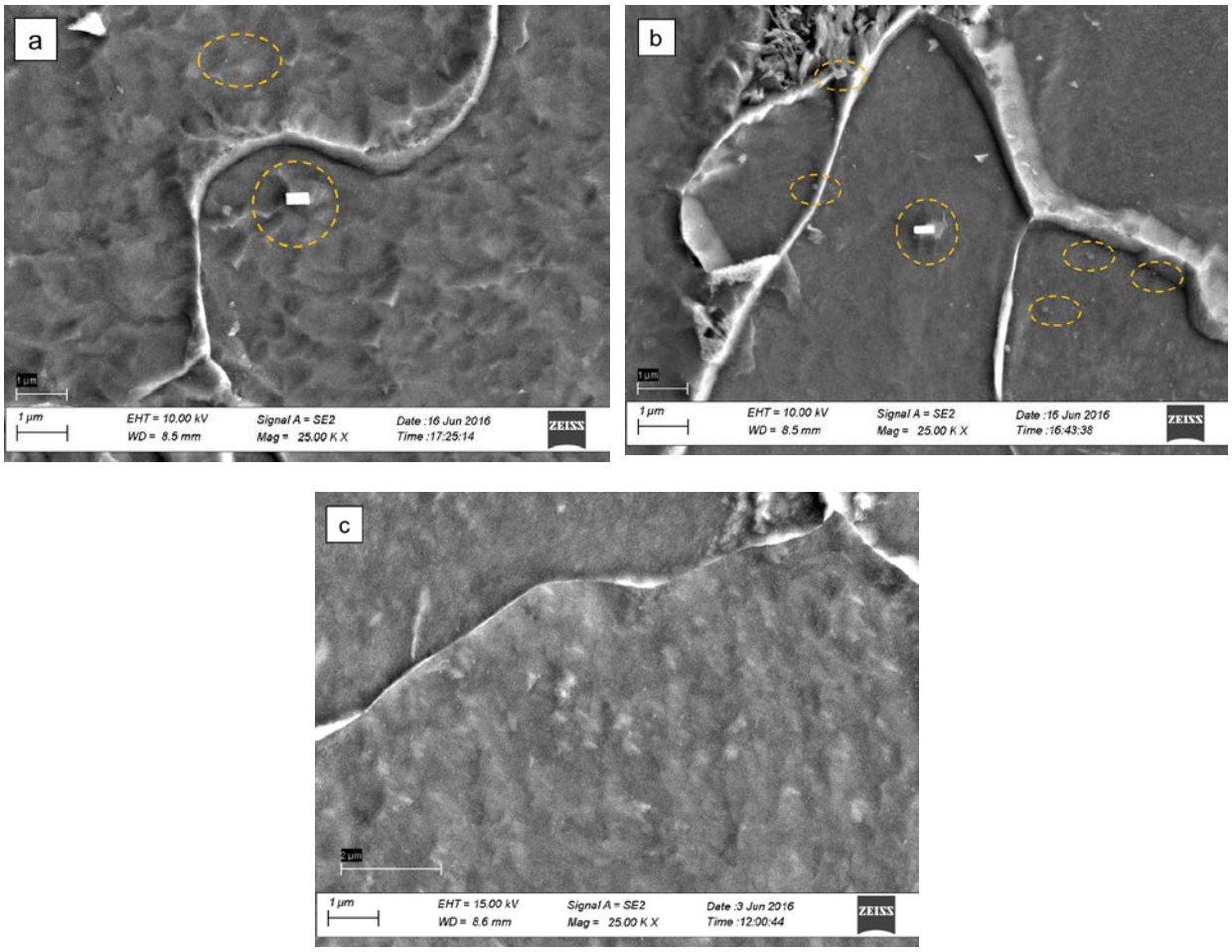

Figure 5.3. Secondary electron images in the AR condition for Ti29 (a), Ti54 (b), and TiF (c) systems

Figure 5.4 includes a line scan and spectra analysis conducted for Ti54 system in the as-rolled condition for the different particles observed in the microstructure. According to information obtained from spectra analysis, medium and large particles (between 200 nm and 0.7 µm) observed in the SEM images correspond to TiN and Ti(C,N) precipitates. It can also be observed on the images that finer cubic or rectangular-shaped particles are dispersed around the matrix and some along the grain boundaries. For the TiF system, spectra analysis conducted on some of the fine features observed in the microstructure was not able to detect and quantify concentration of specific alloying or microalloying elements.

Most of the medium and large particles observed in TiF system corresponded to MnS and Al_2O_3.

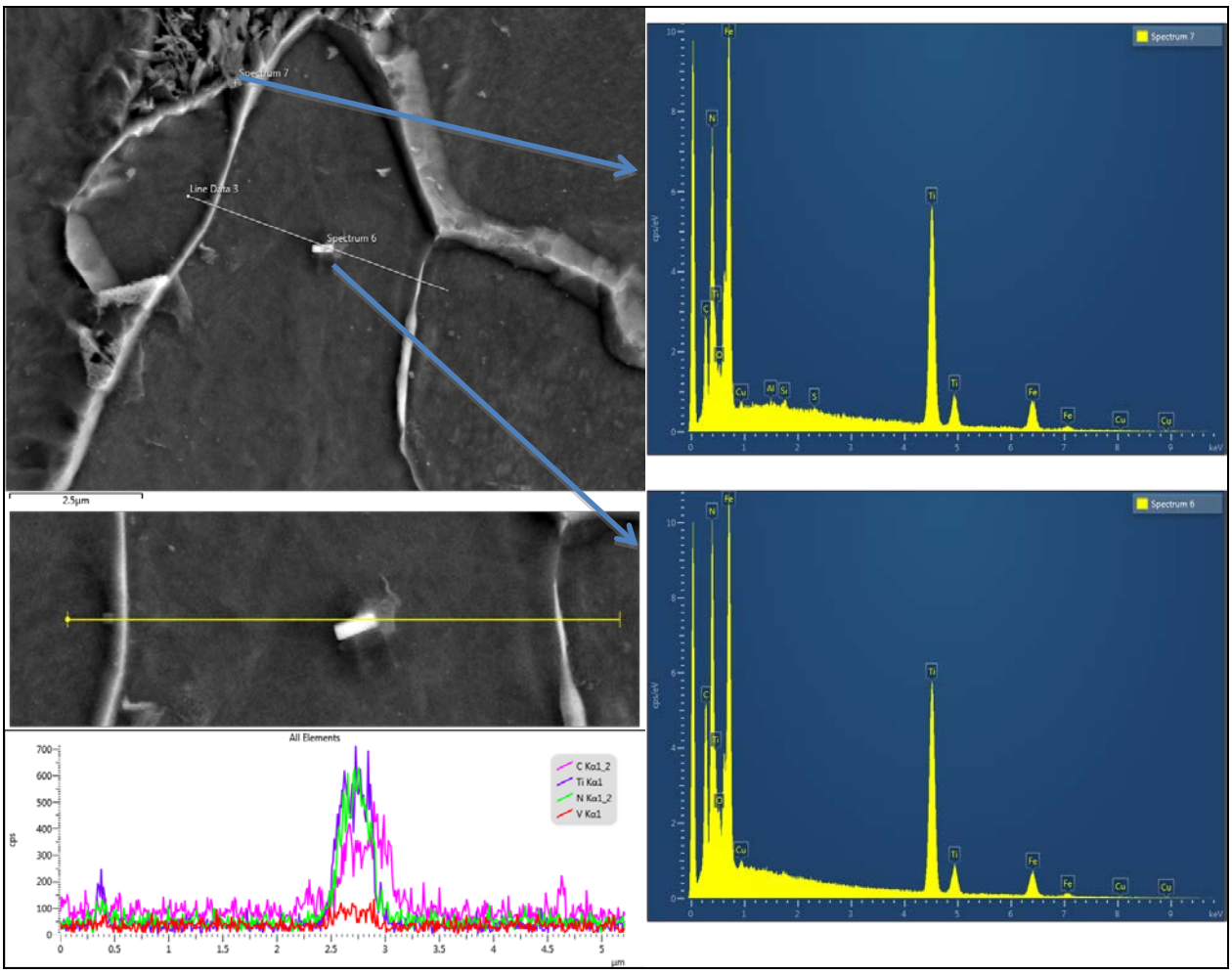

Figure 5.4. Line scan and EDS analysis on particles for Ti54 system in AR condition

Moreover, since many of the features expected to have an effect austenite grain coarsening behavior are below the resolution of both the optical microscopy and scanning electron microscopy, TEM analysis was employed for measuring the precipitate size distribution, composition and morphology. Figures 5.5 presents bright field (BF) images characteristic of the precipitates observed in the as-rolled condition for the alloy systems.

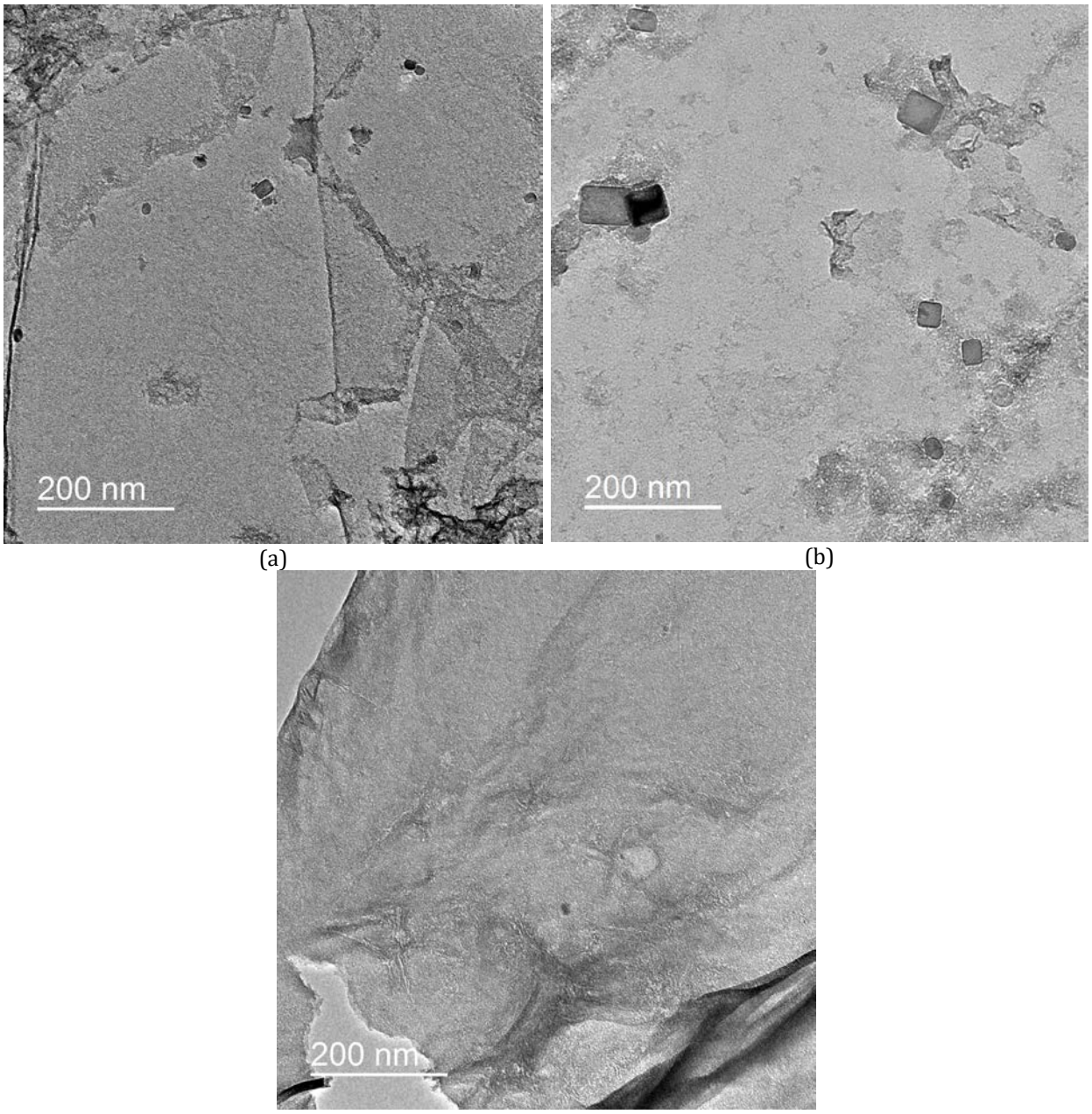

(a) (b)

(c)

Figure 5.5. BF TEM images on thin foils from Ti29 (a), Ti54 (b), and TiF (c) in AR condition

For the Ti-bearing systems two type of precipitates were clearly identified, the first type being the cubic TiN with an FCC NaCl crystal structure with a lattice parameter of 4.232 Å. The second type of particle was irregular in shape and overall with a smaller

average size compared to TiN. According to spectra analysis, these irregular-shaped particles are V and Mo-rich and they tend to form clusters as depicted in Figure 5.6.

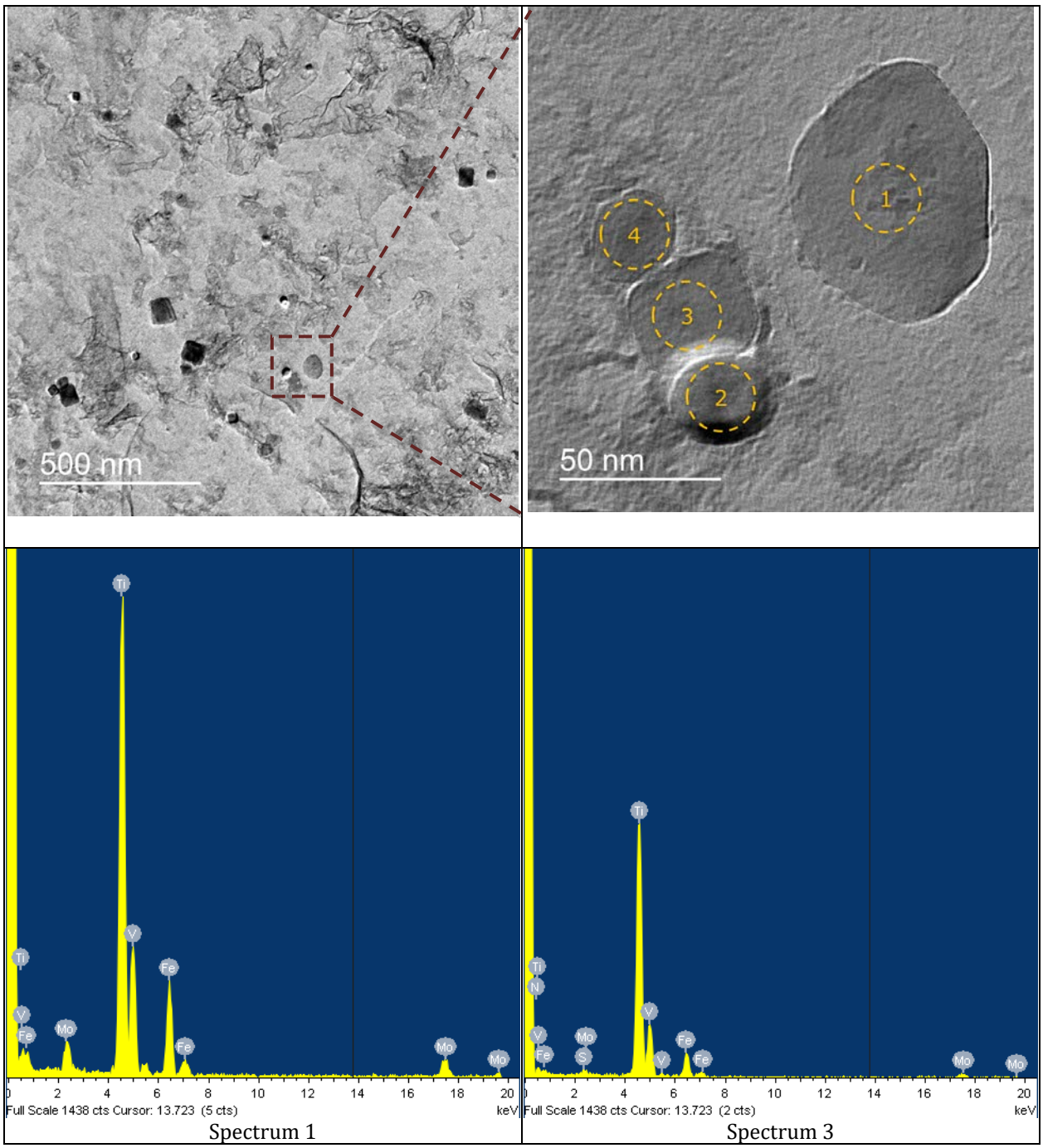

Figure 5.6. Example of spectra analysis on particles observed on Ti54 alloy in AR condition

Table 5.2. EDS spectra from Figure 5.6

Element (%wt)	Spectrum 1	Spectrum 2	Spectrum 3	Spectrum 4
C K	0	0	0	0
N K	14.47	14.6	4.3	9.03
S K	0	0	1.6	1.56
Ti K	57.68	49.87	79.19	61.29
V K	8.7	12.85	6.8	11.76
Fe K	12.53	17.78	8.11	11.74
Mo L	6.62	4.9	0	4.62

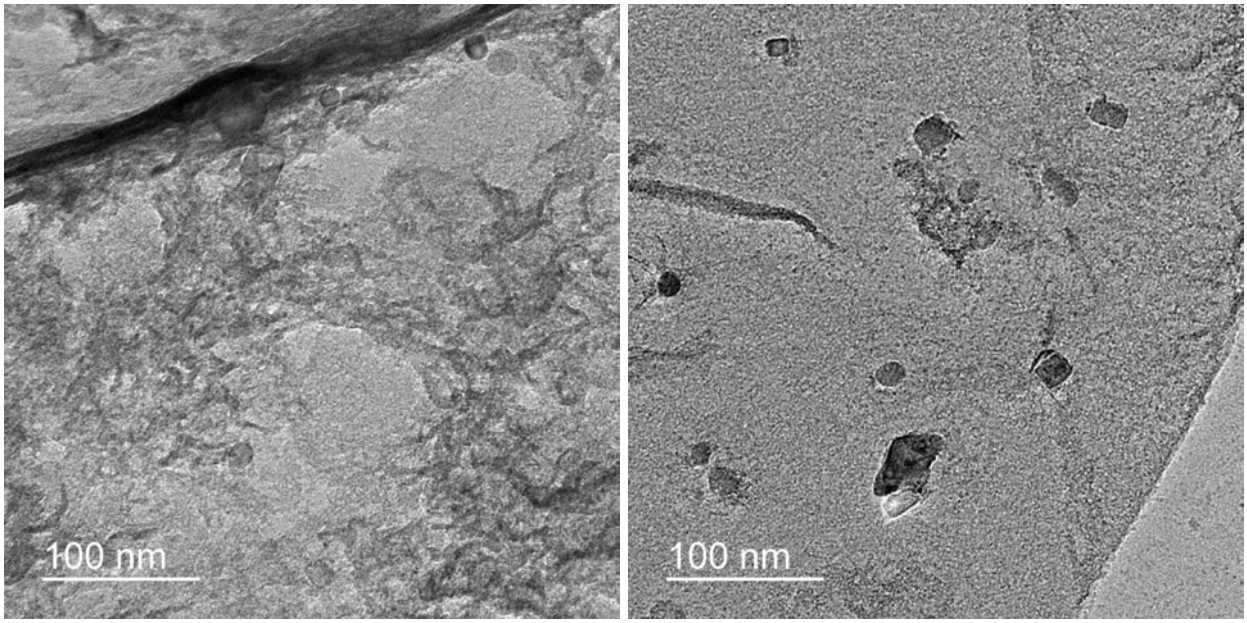

(a) (b)

Figure 5.7. BF TEM image of precipitates on Ti29 alloy system in the AR condition at the grain boundary (a) and the ferrite matrix

Figure 5.8 shows the precipitate size distribution for the Ti-bearing systems measured on images with ImageJ analysis software. At least 200 particles were measured for each Ti-bearing system taken from 3 different thin foil disks each.

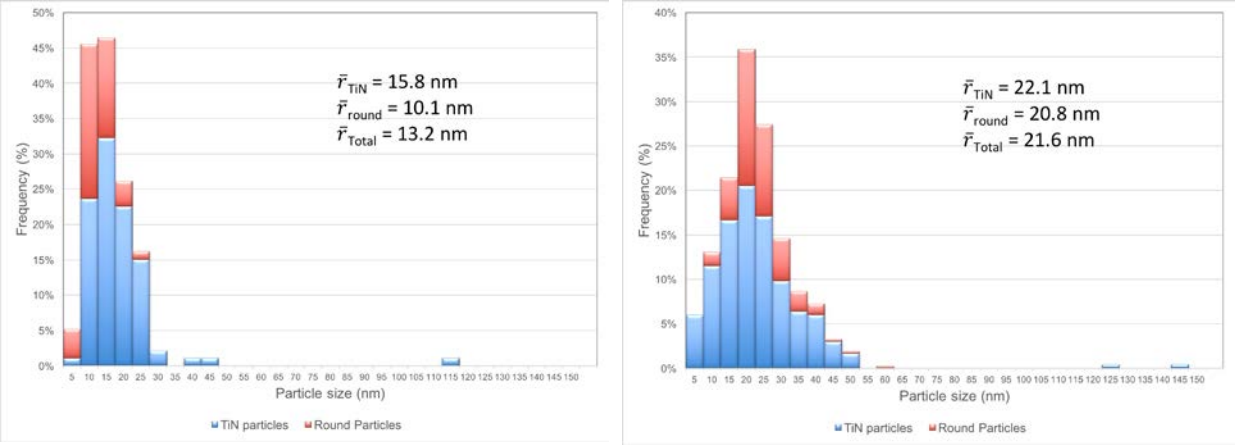

(a) (b)

Figure 5.8. Particle size distribution for (a) Ti29 and (b) Ti54 in the AR condition

As it is represented in Figure 5.8, Ti54 system shows a larger particle size distribution compared to Ti29 in the initial state. The average TiN particle equivalent radius measured were 15.8 nm and 22.1 nm for Ti29 and Ti54, respectively. Very few and dispersed large TiN precipitates (up to ~0.5 μm) were observed in both Ti-bearing alloy systems on thin foils and on SEM analysis. These coarser particles are assumed to have formed during the solidification process at interdendritic areas with Ti concentration enrichment [23].

5.1.4 Mechanical Properties in the As-Rolled Condition

5.1.4.1 Tensile Testing Table 5.3 presents the longitudinal tensile tests conducted on specimens in the as-rolled condition. In order to evaluate the potential variability of the tensile properties of the plates across the width of the plate, specimens were obtained from

three locations along the width, one tensile specimen on each edge as depicted in Figure 5.9 and one specimen located at the centerline of the plate.

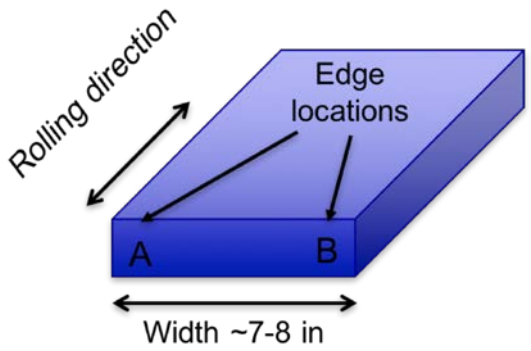

Figure 5.9. Scheme of edge locations for tensile test specimens along the width of plate

Table 5.3. Longitudinal tensile test results on alloy systems in the as-rolled condition

Alloy System	Location	YS (0.2% offset)	YS (EUL=0.5%)	UTS	Uniform Elongation	Total Elongation
		(MPa)	(MPa)	(MPa)	(%)	(%)
TiF	Edge A	332.37	332.07	489.63	13.81	32.99
	Center	312.79	316.42	487.77	13.17	32.81
	Edge B	333.61	332.79	492.81	13.94	32.68
Ti29	Edge A	335.87	336.49	473.21	16.6	35.87
	Center	331.1	332.44	470.99	15.92	34.7
	Edge B	339.42	339.84	475.79	16.18	35.78
Ti54	Edge A	341.82	339.09	478.11	15.9	35.53
	Center	335.64	327.2	477.51	16.23	35.98
	Edge B	343.28	344.21	477.69	16.02	35.3

Overall, TiF shows higher Ultimate Tensile Strength values compared to Ti29 and Ti54, while Ti-bearing systems showed similar tensile properties results. A slight increase in the yield strength is observed at the edges of the width compared to the centerline, this

can be associated to the finer ferrite grain size difference between the edge and center presented in Table 5.1. Ti-bearing systems presented a higher uniform and total elongation compared to the Ti-free system which can related to a higher strain hardening capability of these systems.

5.1.4.2 Hardness Figure 5.10 presents the hardness Vickers results across the thickness of the plates in the as-rolled conditions for the three systems. TiF alloy showed a slight higher hardness compared to the Ti-bearing systems with an average value of 156.2 HV_2. Ti29 and Ti54 showed similar hardness properties with averages values of 144.4 HV_2 and 144.3 HV_2, respectively.

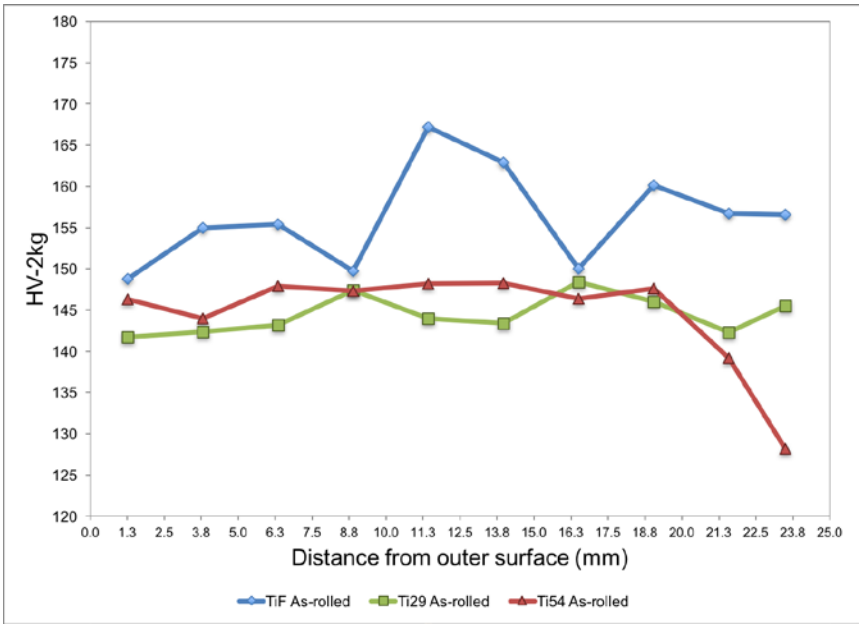

Figure 5.10. Hardness Vickers profile across the thickness of plates in AR condition

5.1.4.3 Charpy V-Notch Impact Testing Figures 5.11 presents the transverse CVN Impact test absorbed energy and shear area values obtained after testing at temperature

from 0°C to -40°C for the three alloy systems in the as-rolled conditions. Longitudinal CVN results are presented in Figure 5.12.

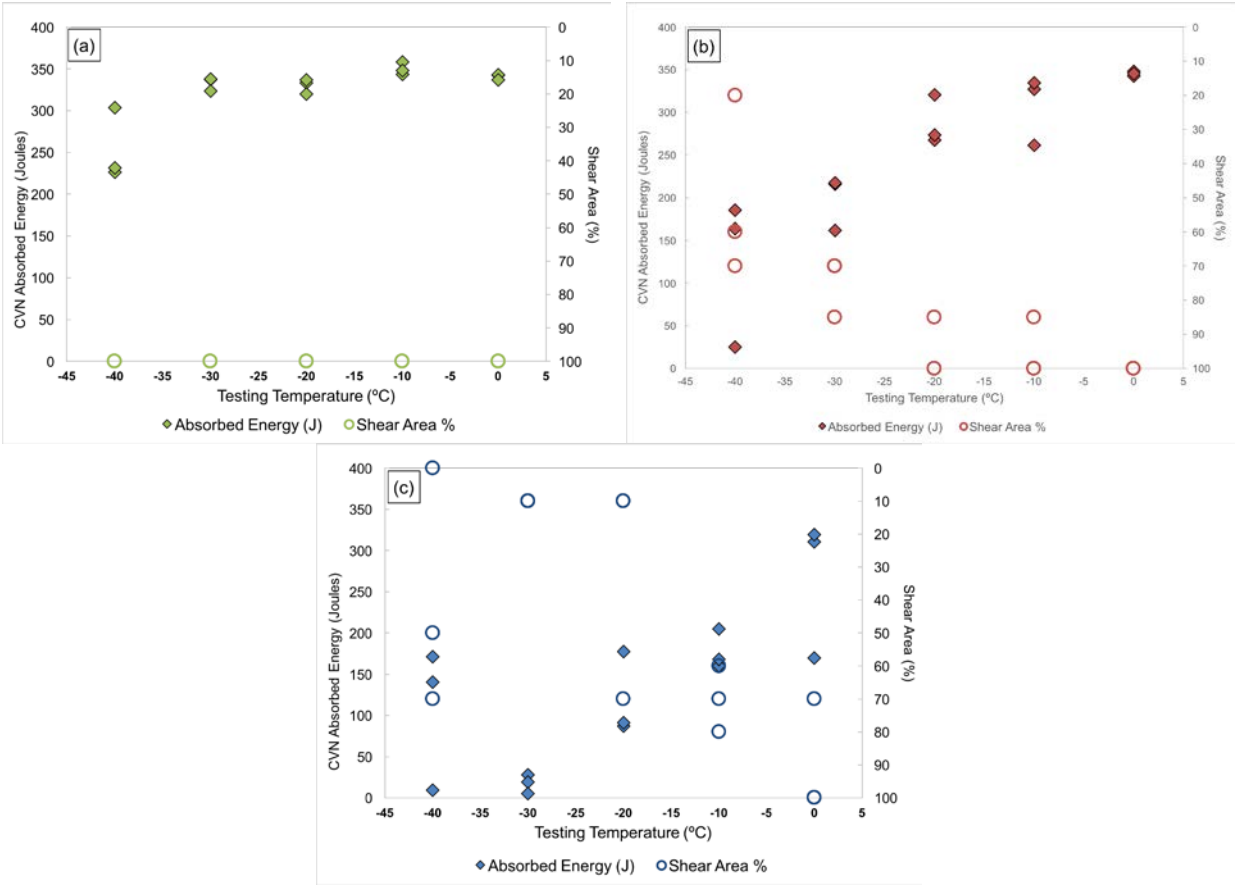

Figure 5.11. Transverse CVN Impact test results on (a) Ti29, (b) Ti54, and (c) TiF

As observed in Figure 5.11 and Figures 5.12, Ti-bearing systems showed better impact toughness properties at the testing temperatures with a shelf energy value around 350 Joules and a transition temperature below -30°C considering a 50% of ductile fracture surface area criteria for both transvers and longitudinal test results. TiF alloy system on the contrary presented disperse absorbed energy and shear area values and a high percentage of cleavage fracture area for most of the testing temperature conditions. Ti29

presented better impact toughness properties compared to alloy system Ti54 with absorbed energy values above 250 Joules and a shear area above 85% even at testing temperature of -40°C.

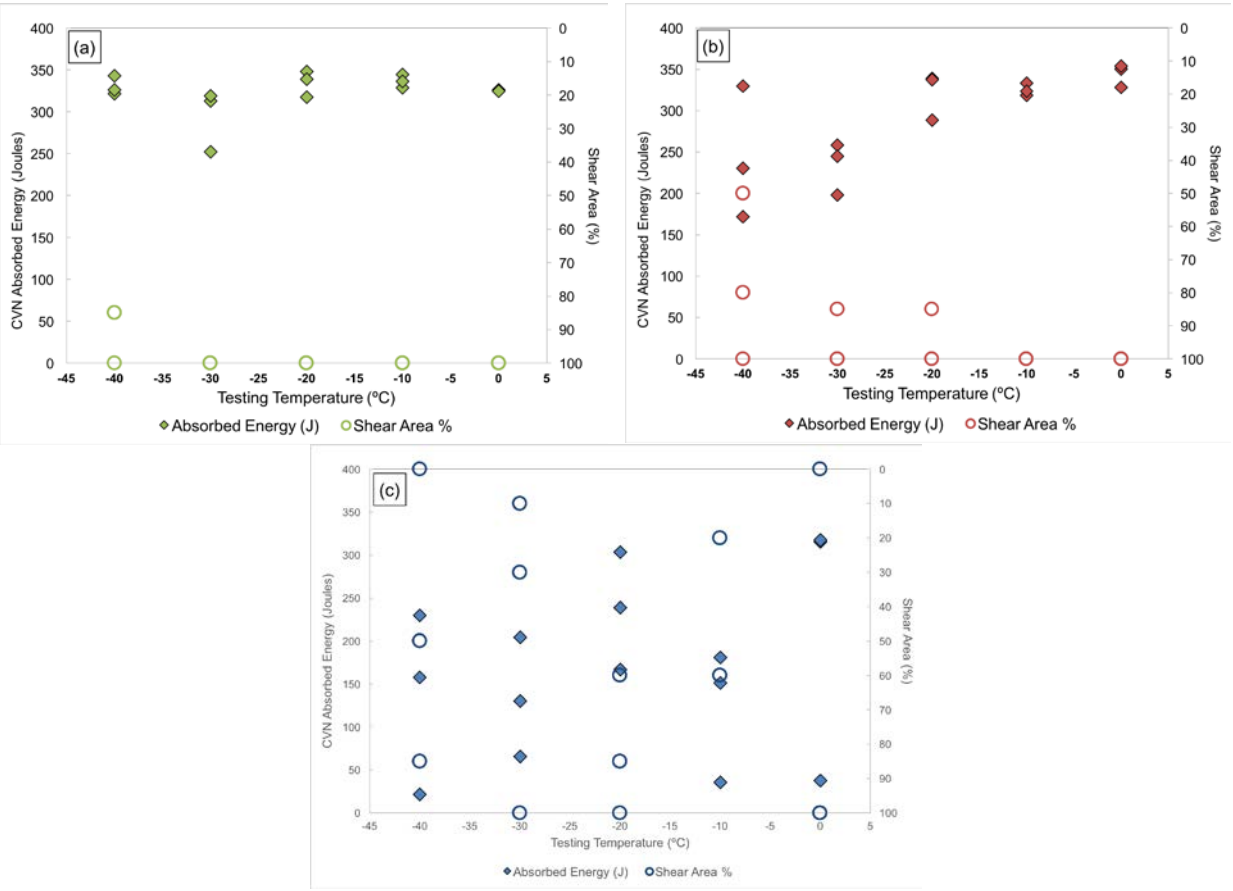

Figure 5.12. Longitudinal CVN Impact test results on (a) Ti29, (b) Ti54, and (c) TiF

5.2 PRIOR AUSTENITE GRAIN SIZE STUDY

5.2.1 Austenite Grain Coarsening Behavior

Characteristic images of the different isothermal holding experiments are presented from Figures 5.13 to 5.18. As it is explained in section 4.3, the holding time used for all the conditions was of 30 minutes. It is important to take into account that magnification of the images presented for each temperature was adjusted based on the average grain size diameter obtained at a particular temperature.

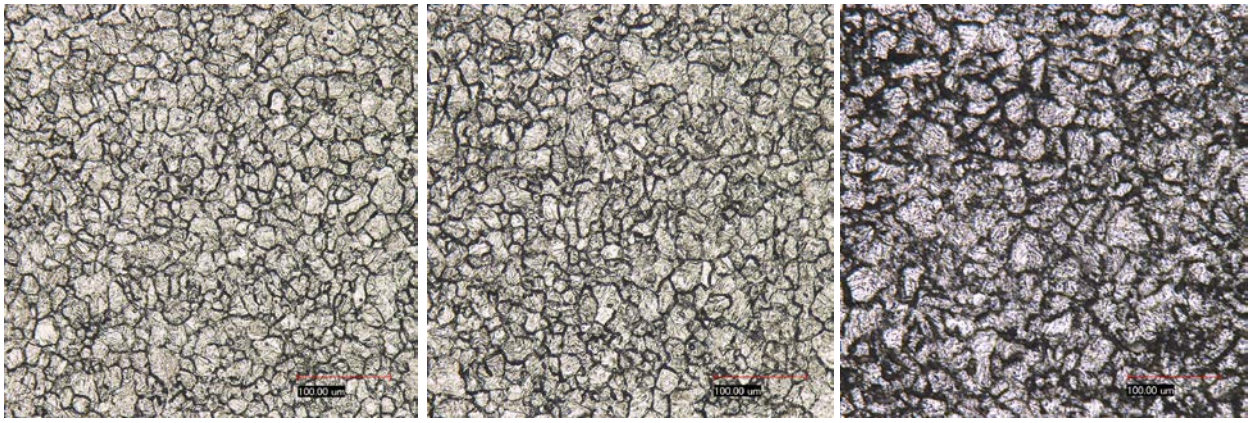

(a) (b) (c)

Figure 5.13. PAGS on (a) Ti29, (b) Ti54, and (c) TiF at 900°C (500X Magnification)

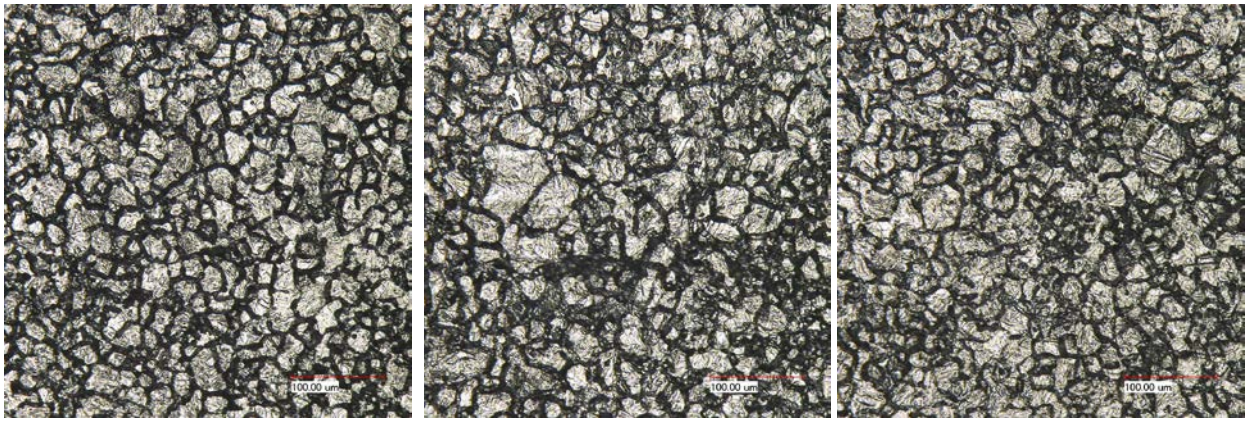

(a) (b) (c)

Figure 5.14. PAGS on (a) Ti29, (b) Ti54, and (c) TiF at 950°C (500X Magnification)

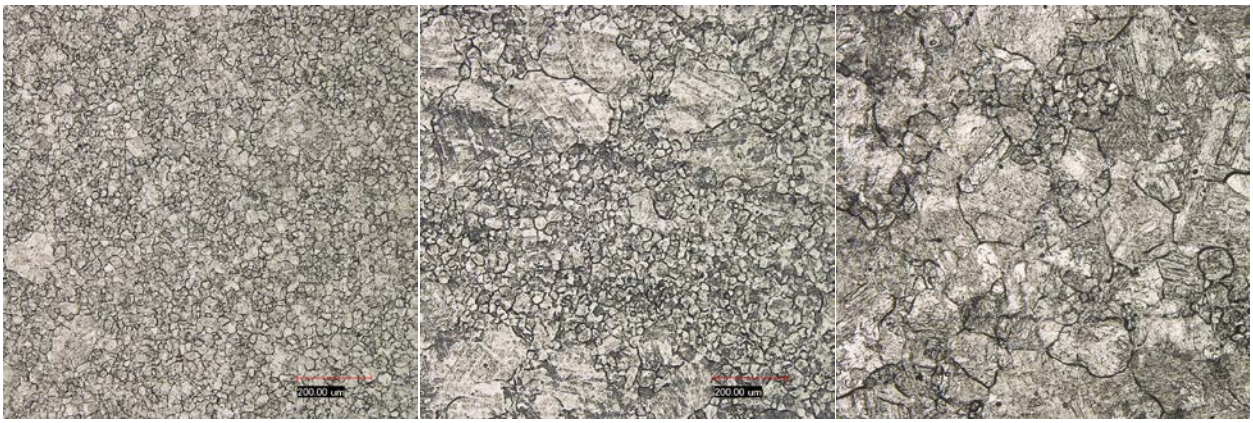

(a) (b) (c)

Figure 5.15. PAGS on (a) Ti29, (b) Ti54, and (c) TiF at 1000°C (200X Magnification)

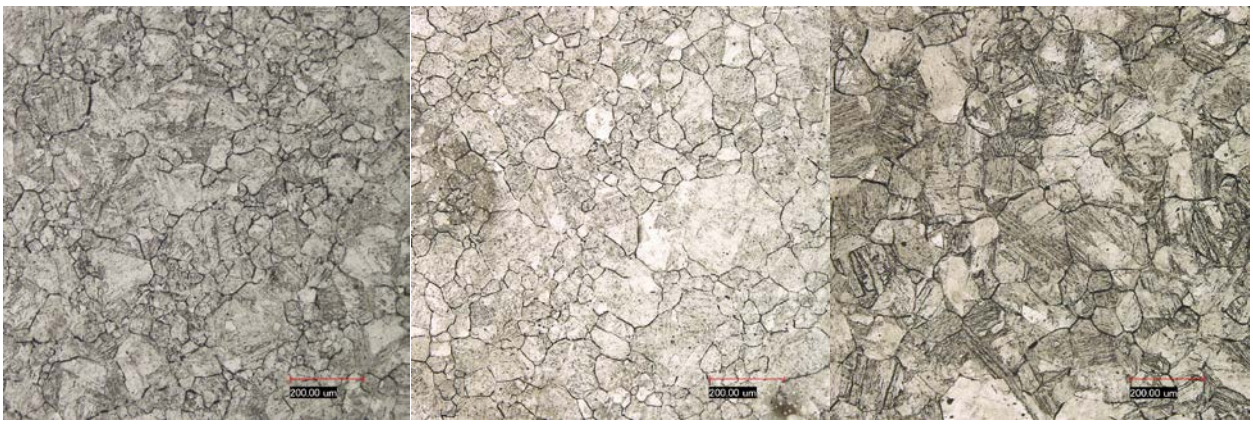

(a) (b) (c)

Figure 5.16. PAGS on (a) Ti29, (b) Ti54, and (c) TiF at 1100°C (200X Magnification)

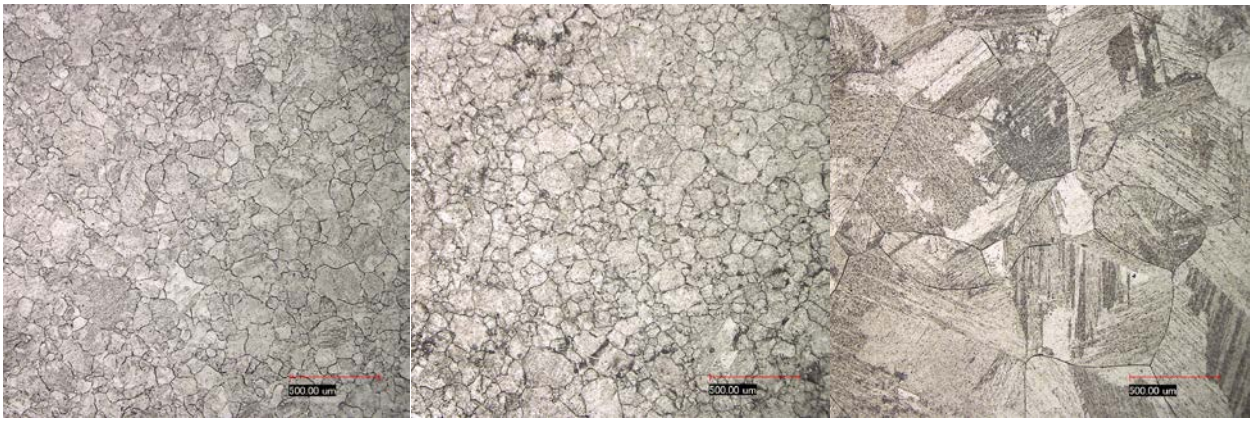

(a) (b) (c)

Figure 5.17. PAGS on (a) Ti29, (b) Ti54, and (c) TiF at 1200°C (100X Magnification)

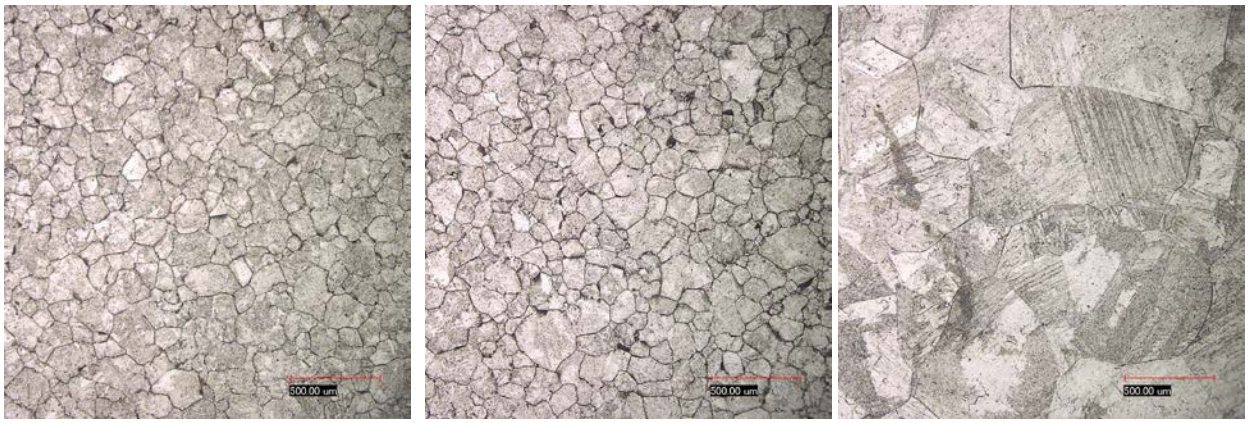

(a) (b) (c)

Figure 5.18. PAGS on (a) Ti29, (b) Ti54, and (c) TiF at 1300°C (100X Magnification)

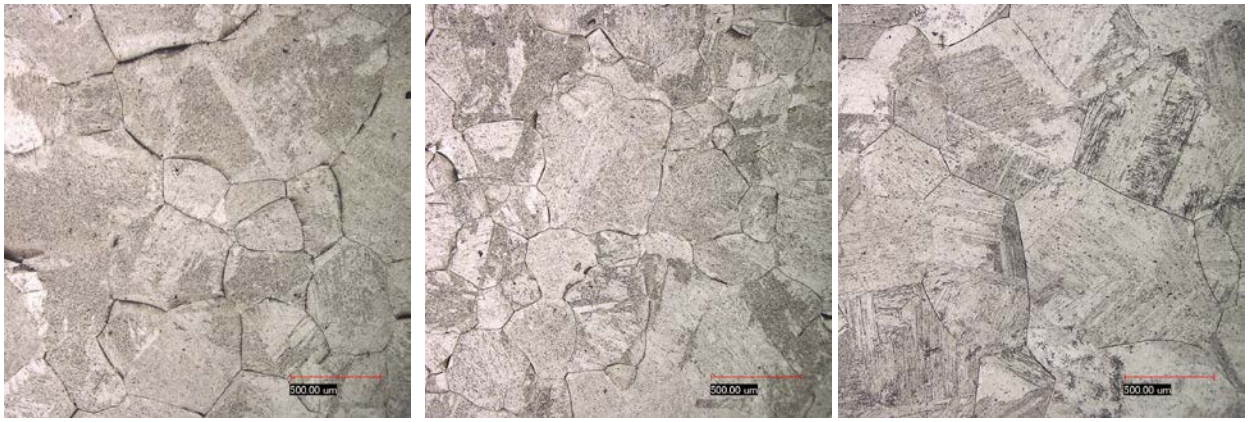

(a) (b) (c)

Figure 5.19. PAGS on (a) Ti29, (b) Ti54, and (c) TiF at 1350°C (100X Magnification)

Figure 5.20 presents a graph with the mean austenite grain size measured for the three systems at each holding temperature. As it can be expected and clearly observed from measured values displayed, austenite grains grow larger at higher holding temperatures. For the lower temperature range between, Ti29 showed the smallest austenite grain size compared to TiF and Ti54 systems.

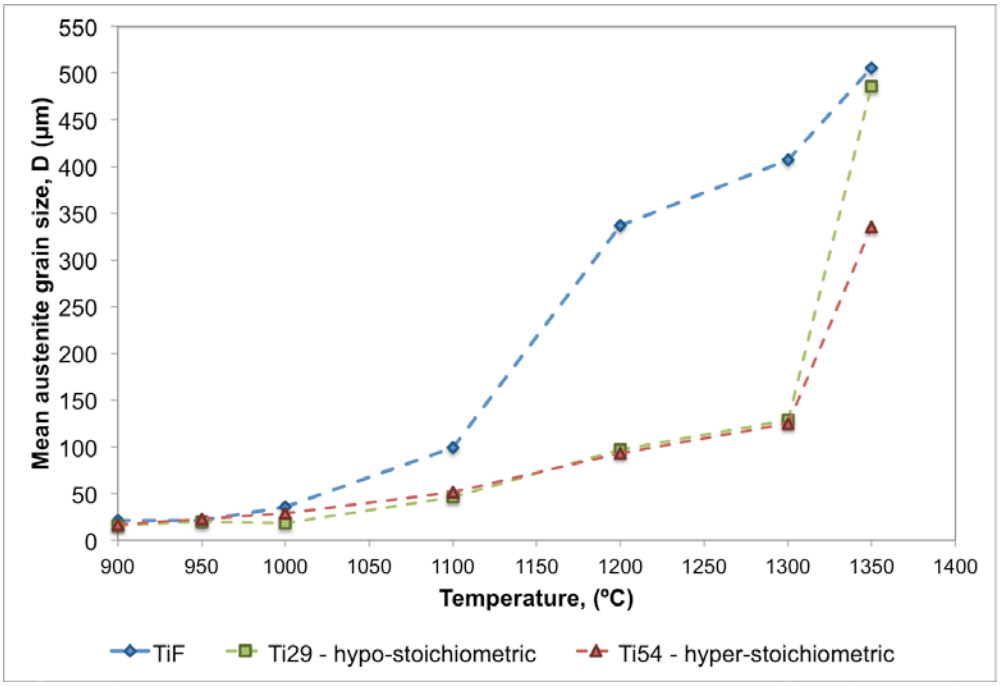

Figure 5.20. Experimental austenite grain size behavior measured on TiF, Ti29, and Ti54 systems

Based on micrographs presented TiF starts to show clear abnormal grain coarsening at a holding temperature of 1000°C and normal grain growth seem to continue at higher temperatures with an apparent significant grain growth rate. The Ti29 system shows abnormal grain coarsening behavior at a holding temperature of 1100°C and homogeneous grain growth behavior continues at temperatures between 1200°C and 1300°C. Ti54 alloy system showed some presence of large grains at the holding temperature of 1000°C and a

clear mixed-grain region at 1100°C followed by a uniform grain growth behavior for higher temperatures similar to that observed on Ti29 system.

In order to help on the determination on the grain coarsening temperature, or in other words, the holding temperature at which austenite grains show a mixed-grain behavior, Figures 5.21 to 5.22 present grain size distribution frequencies for different holding temperatures.

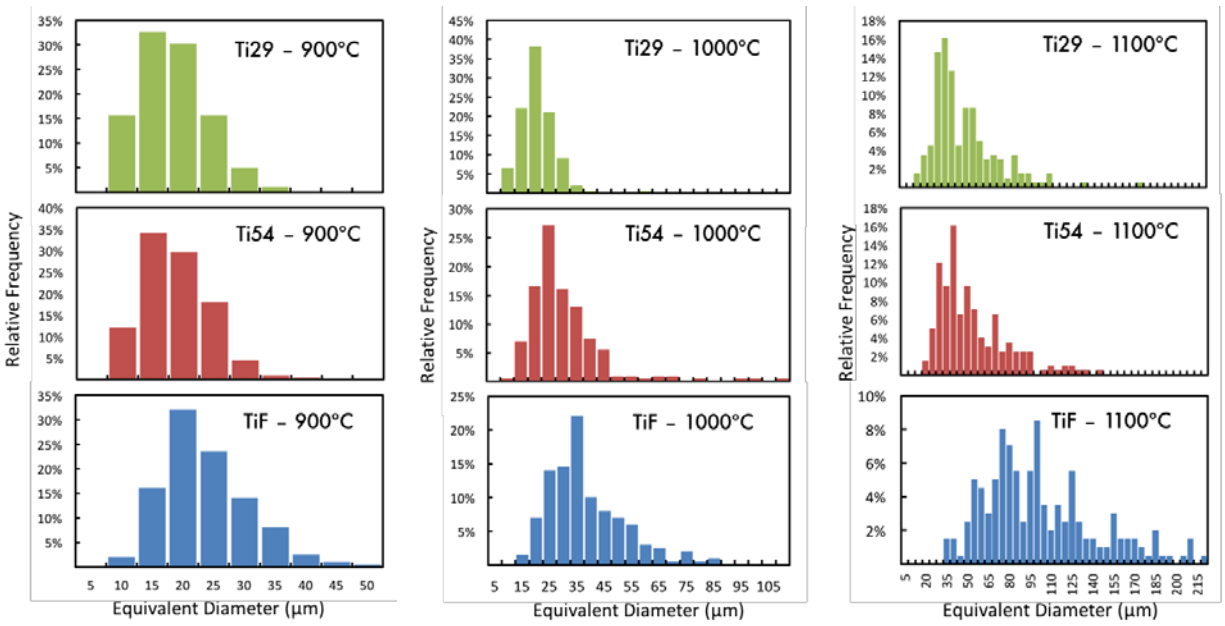

Figure 5.21. Austenite grain size distribution at 900°C, 1000°C, and 1100°C

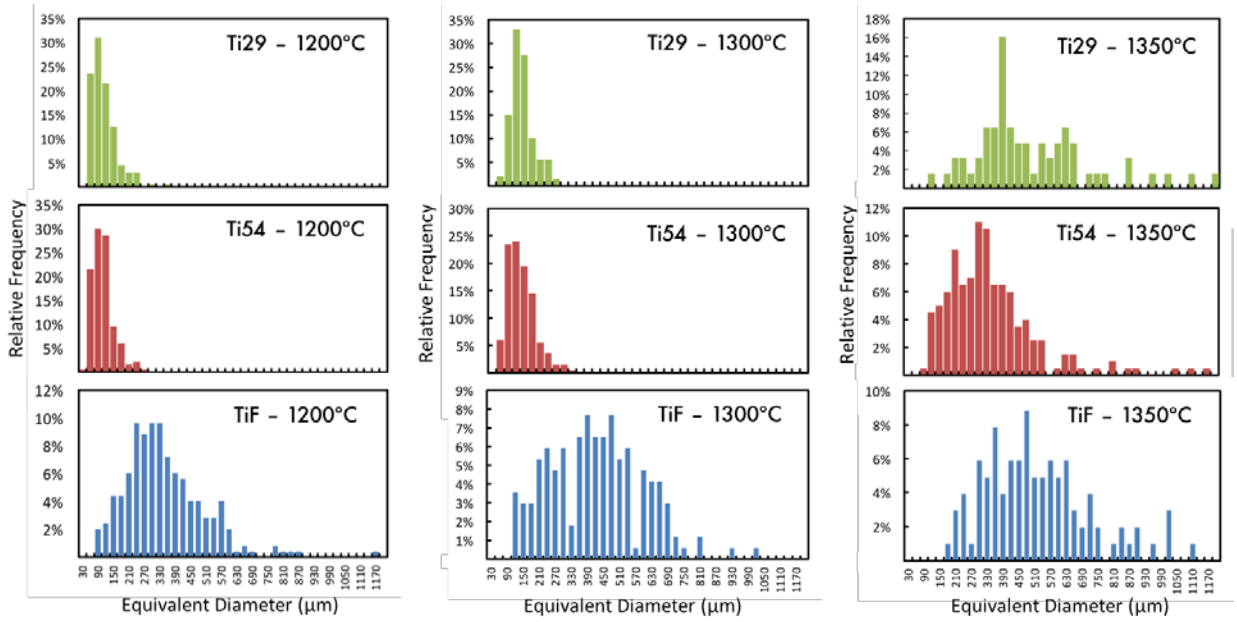

Figure 5.22. Austenite grain size distribution at 1200°C, 1300°C, and 1350°C

Table 5.4 presents a summary of average grain size diameter and the standard deviation for all the conditions tested in the PAGS study. This information will be used for estimations and reference in further sections.

Table 5.4. Measured average austenite grain size diameter and standard deviation

Holding Temp (°C)	TiF		Ti29		Ti54	
	Avg D (µm)	Std Dev (µm)	Avg D (µm)	Std Dev (µm)	Avg D (µm)	Std Dev (µm)
900	21.09	7.11	15.92	5.43	16.21	5.63
950	20.87	6.24	19.19	5.55	22.45	8.37
1000	35.71	13.98	18.34	6.07	28.37	14.19
1100	99.34	40.21	46.03	23.00	51.08	24.81
1200	336.51	165.83	96.74	48.97	93.13	40.87
1300	407.00	175.63	128.59	43.52	124.40	53.36
1350	505.58	203.12	486.21	223.30	335.47	187.37

5.2.2 Volume Fraction and TiN Precipitate Coarsening Estimation

A classical approach for the estimation of volume fraction of TiN and precipitate coarsening was conducted for the Ti-bearing systems by using the solubility product equations of TiN in austenite and the particle coarsening theory presented in section 2.2.3. Calculations were done taking into account only the presence of stable TiN precipitates as other particles were present in smaller fractions and assumed not to play a significant role in exerting pinning forces against grain boundary mobility forces. Similar calculations are provided by Gladman [11], and also available in several publications [46, 49].

For the estimation of the TiN volume fraction changes at the different temperatures used for the PAGS study, the solubility product for TiN in austenite by Inoue et al. (see Table 2.2) was selected [25]. Figure 5.23 shows the isotherm lines of the solubility product in equilibrium including the dashed stoichiometric line (24:7) for TiN where it can be observed that Ti29 falls below this line and Ti54 is above it corresponding to the hypo-stoichiometric and hyper-stoichiometric conditions, respectively.

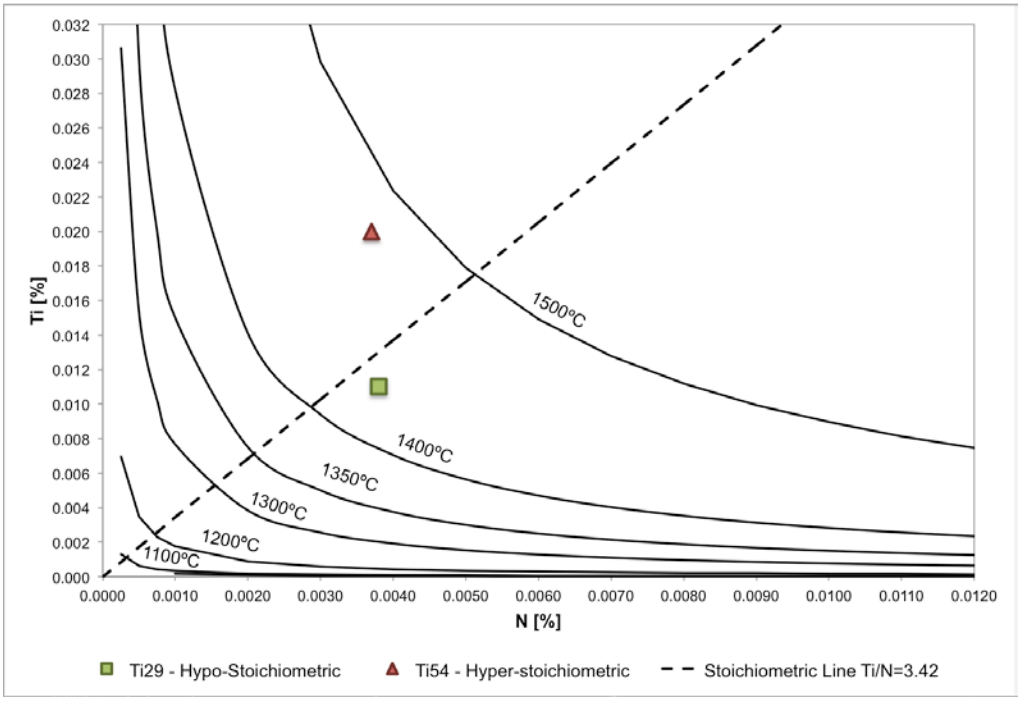

Figure 5.23. TiN solubility product after Inoue et al. [25]

Table 5.5 presents the Ti content dissolved and as precipitate based on solubility product calculations. The N in solution and as precipitate was calculated considering the stoichiometry of Ti/N=3.42. For Ti54 it was assumed that the Ti content that is not tied to TiN particles is considered to be available in the matrix (as Ti dissolved in Table 5.5.) While this might not be accurate for the lower temperature range, it is a good approximation for the estimation at the higher temperature range were TiN is the only stable compound and were most of the further analysis and discussion will be focused.

Table 5.5. Amount of Ti in solution (s) and precipitate (ppt) based on solubility product calculations

Holding Temperature (°C)	Ti29 (Ti_{total} = 0.011%wt)				Ti54 (Ti_{total} = 0.020%wt)			
	Ti_s	Ti_{ppt}	N_s	N_{ppt}	Ti_s	Ti_{ppt}	N_s	N_{ppt}
900	0.00012	0.01088	0.00063	0.00317	0.00747	0.01253	0.00005	0.00365
950	0.00023	0.01077	0.00066	0.00314	0.00757	0.01243	0.00008	0.00362
1000	0.00039	0.01061	0.00071	0.00309	0.00774	0.01226	0.00012	0.00358
1100	0.00105	0.00995	0.00090	0.00290	0.00839	0.01161	0.00031	0.00339
1200	0.00244	0.00856	0.00130	0.00250	0.00979	0.01021	0.00072	0.00298
1300	0.00512	0.00588	0.00208	0.00172	0.01246	0.00754	0.00150	0.00220
1350	0.00716	0.00384	0.00268	0.00112	0.01451	0.00549	0.00210	0.00160

Figure 5.24 shows a graph of the variation of the volume fraction of TiN and the Ti content in the Matrix (dissolved or tied to less stable precipitate) with respect to the holding temperature.

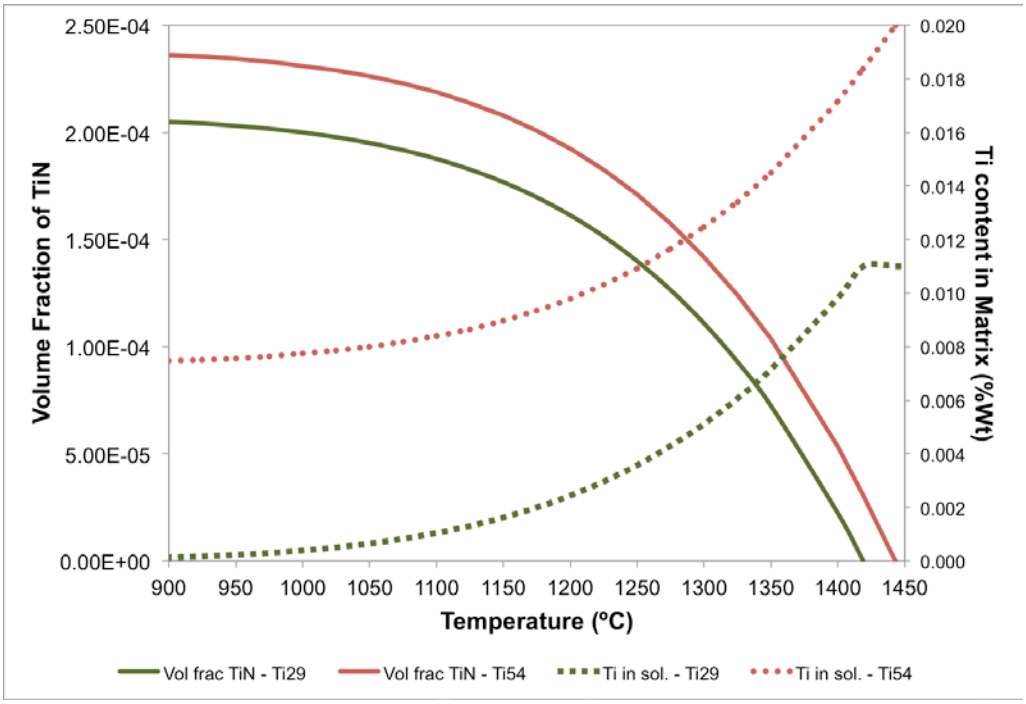

Figure 5.24. Estimated volume fraction of TiN and Ti content in matrix

For the particle size estimation, the theory of particle coarsening provided by Lifshitz, Slyozov, and Wagner (LSW) was used (Equation 2.11). Table 5.6 presents a summary of the physical values used for the calculations at the different holding temperature. The value of the concentration of Ti in solution was taken from the solubility product calculations presented in Table 5.5 and the initial precipitate radius was obtained from the TEM analysis in the initial state (see Figure 5.8) for the respective Ti-bearing system.

The diffusion coefficient in LSW equation will be dictated by the diffusivity of the rate limiting solute, which for this case is Ti in austenite and can be obtained by the following expression:

$$D_{Ti} = D_0 e^{\left(-Q/RT\right)} \qquad \textbf{Equation 5.1}$$

where D_{Ti} is the diffusion coefficient of Ti in austenite, D_0 is a pre-exponential constant, Q is the activation energy for bulk diffusion, R is the gas constant and T is the absolute temperature in K. Values of the diffusion coefficient for the different holding temperatures are presented in Table 5.7.

Table 5.6. Values used for particle coarsening calculations

Symbol	Description	Value	Units	Reference
σ	Interfacial energy	0.8	J/m^2	[46]
V_m	Molar volume of TiN	11.53	11.53 cm^3/mol	[53]
D_0	Diffusion coefficient constant (Ti in austenite)	m^2/s	0.15×10^4	[11]
Q	Activation energy for bulk diffusion	250	kJ/mol	[37]
R	Ideal gas constant	8.314	J/mol·K	-
Av	Avogadro's Number	6.022×10^{23}	atoms/mol	-
Vu_{TiN}	Volume of unit cell for TiN	7.62×10^{-23}	cm^3	[11]
Vu_γ	Volume of unit cell for austenite	4.62×10^{-23}	cm^3	[11]
A_{TiN}	Atomic weight for TiN	61.91	g	[46]
A_γ	Atomic weight for austenite	55.9	g	[46]

Table 5.7. Calculated diffusivity of Ti in austenite

Temp (°C)	Diffusivity*10^{-12} (cm^2/s)
900	1.10525
950	3.15195
1000	8.27839
1100	46.2437
1200	204.514
1300	748.688
1350	1349.11

Figure 5.25 presents the results of the estimated particle coarsening behavior estimated for Ti29 and Ti54. As it can be expected, alloy system presents a higher particle size compared Ti29 given the higher concentration of Ti in solution which is the main driving force for particle coarsening.

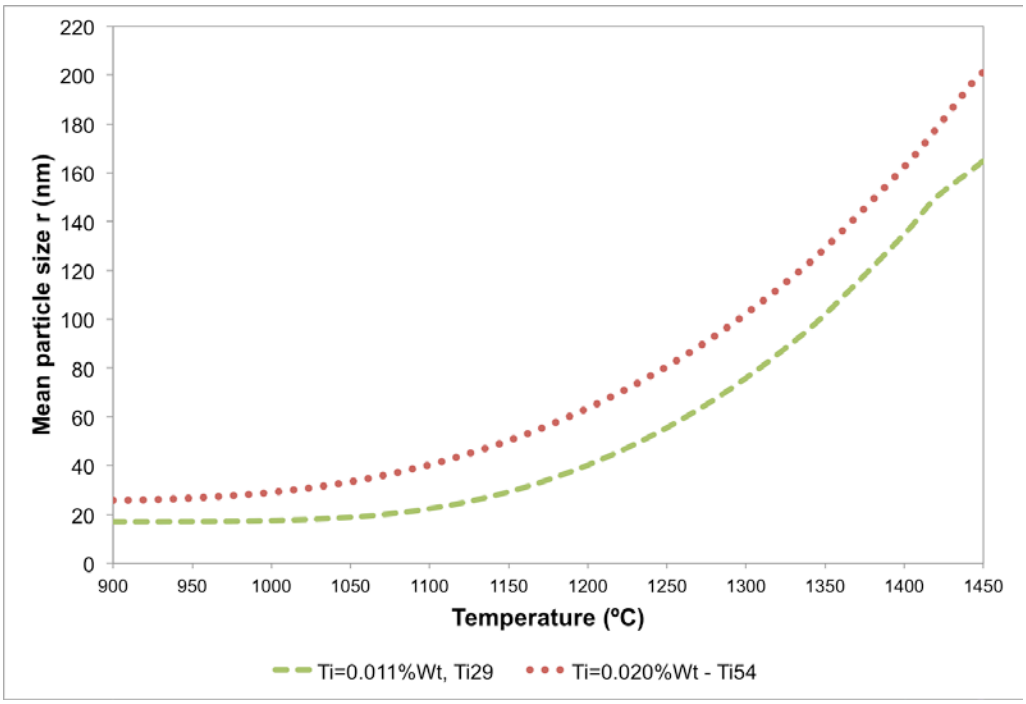

Figure 5.25. Particle coarsening behavior for Ti29 and Ti54 estimation based LSW equation

5.2.3 Austenite Grain Size Model, Pinning Force, and Driving Force for Grain Growth

With the estimation of the TiN volume fraction and the particle size obtained in the previous section, it is possible to construct a simple model for the estimation of the grain coarsening behavior and the pinning force exerted by the stable particles during isothermal treatments as explained in sections 2.24 and 2.25 respectively.

For the austenite grain size model, the Gladman expression (Equation 2.13) with a Zener coefficient of 1.60 gave the best agreement with respect to the experimental values obtained from the isothermal experiments. Figure 5.26 presents a comparison between the austenite grain size prediction and the experimental values.

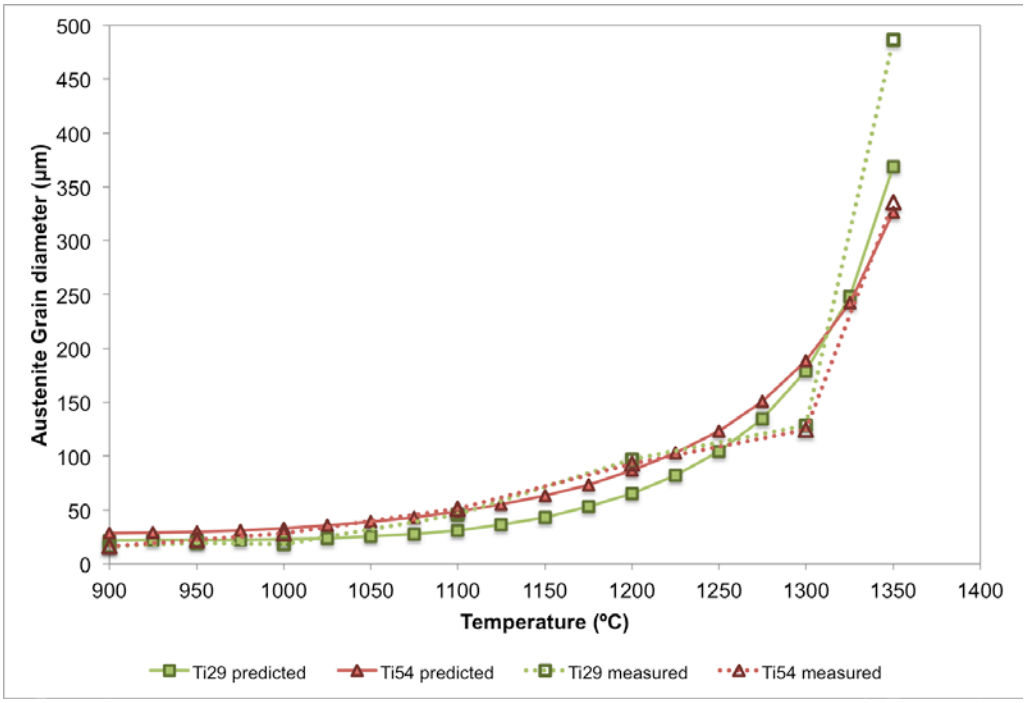

Figure 5.26. Predicted and measured austenite grain size

Table 5.8 presents the pinning force calculated based on the precipitate radius estimation and the three different models for Gladman's expression (Equation 2.16), the rigid boundary model (Equation 2.17), and the flexible boundary model (Equation 2.18). For the precipitate volume fraction only half of the value was considered based on observation by Gao and Baker [3] that only the fraction of fine precipitates plays a role in exerting pinning force (approximately 50% of the size distribution.)

Table 5.8. Pinning force estimations for Ti-bearing systems

Holding Temp (°C)	Ti29					Ti54				
	0.5*Vf (x 10^{-4})	Particle size (nm)	Gladman Model (kN/m^2)	Rigid boundary model (kN/m^2)	Flexible boundary model (kN/m^2)	0.5*Vf (x 10^{-4})	Particle size (nm)	Gladman Expression (kN/m^2)	Rigid boundary model (kN/m^2)	Flexible boundary model (kN/m^2)
900	1.025	15.83	7.772	9.896	105.723	1.181	22.84	6.206	7.901	80.522
950	1.016	15.94	7.647	9.736	104.341	1.171	24.17	5.815	7.404	75.660
1000	0.999	16.38	7.324	9.325	100.454	1.156	26.96	5.145	6.550	67.235
1100	0.938	21.69	5.191	6.610	72.731	1.094	39.33	3.338	4.251	44.434
1200	0.806	40.03	2.418	3.079	35.628	0.962	63.16	1.829	2.329	25.406
1300	0.554	75.85	0.877	1.117	14.643	0.710	102.08	0.835	1.063	12.835
1350	0.361	101.98	0.426	0.542	8.196	0.517	129.09	0.481	0.613	8.221

As it can be observed in Table 5.8, the flexible boundary model overestimates the pinning force exerted by particles compared to both the Gladman and the rigid boundary models. Overall, Gladman's model estimates conservative values of pinning for the isothermal temperature range studied. On the other hand, Table 5.9 presents the estimated driving forces for grain growth for the different reheating temperatures taking into account Zener (Equation 2.19) and Gladman's models (Equation 2.20), the later includes two values of Z, 1.6 and 2.0. For Zener equation the radius of curvature R considered was one order of magnitude higher than the austenite grain size measured [54].

Table 5.9. Estimation of driving forces for grain growth in Ti-bearing systems

Holding Temperature (°C)	Ti29				Ti54			
	Austenite Grain radius (μm)	Zener (kN/m^2)	Gladman (kN/m^2)		Austenite Grain radius(μm)	Zener (kN/m^2)	Gladman (kN/m^2)	
			Z=8/5	Z=2			Z=8/5	Z=2
900	7.96	20.097	-25.121	-50.243	8.10	19.746	-24.682	-49.365
950	9.59	16.676	-20.845	-41.690	11.23	14.252	-17.814	-35.629
1000	9.17	17.451	-21.814	-43.628	14.18	11.281	-14.101	-28.203
1100	23.01	6.952	-8.690	-17.380	25.54	6.265	-7.832	-15.663
1200	48.37	3.308	-4.135	-8.270	46.56	3.436	-4.295	-8.590
1300	64.30	2.488	-3.111	-6.221	62.20	2.572	-3.216	-6.431
1350	243.11	0.658	-0.823	-1.645	167.73	0.954	-1.192	-2.385

Following the aforementioned assumptions and the experimental data obtained from the PAGS study, the calculated driving forces for grain growth for both Ti-bearing systems are around two times greater than the pinning force calculated with either Gladman's model or rigid boundary model. The flexible boundary model always estimates a greater pinning force compared to the driving forces for grain growth.

5.2.4 Precipitation Analysis for Selected Conditions

This section includes some preliminary evidence of precipitates from SEM analysis with both secondary and backscatter electron detection for selected isothermal conditions as well as TEM images analysis from the isothermal conditions at 1,200°C and 1,350°C for the Ti-bearing systems in order to confirm stability of TiN and dissolution of less stable precipitates observed in the initial state conditions.

Figure 5.27 shows a line scan and point analysis on TiN precipitates observed in a specimen with isothermal holding temperature of 900°C for Ti54 system.

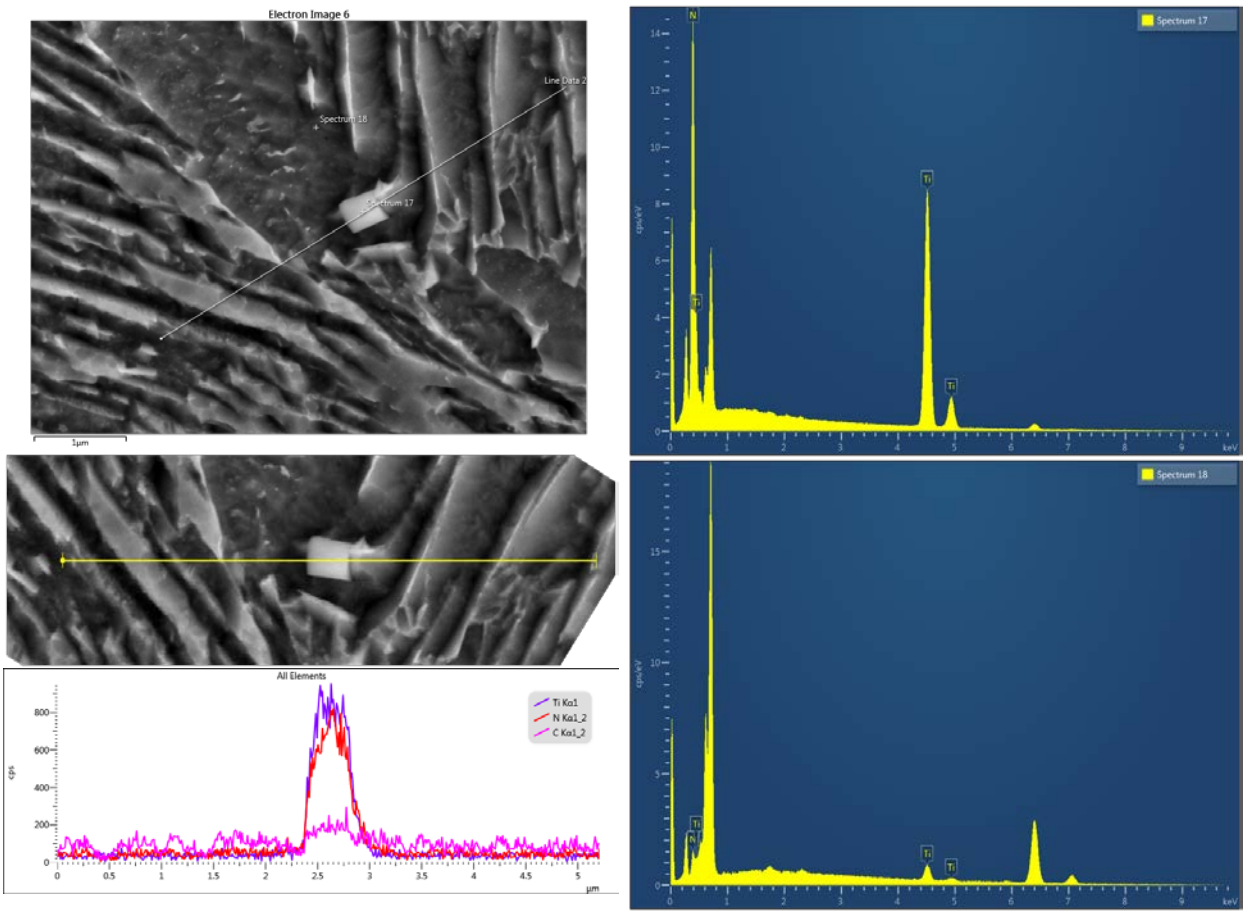

Figure 5.27. Line scan and point analysis on particles along a grain boundary (Ti54 at 900°C)

Figure 5.28 presents an example of large and small TiN particles that were observed with backscattered-electron detector (BSD) in Ti54 under isothermal condition at 900°C. This confirmed the stability of precipitates subjected to this type of heat treatment similar to an austenitizing condition before quenching. Table 5.10 shows a summary of the EDS analysis conducted on precipitates shown in image (a) of Figure 5.28.

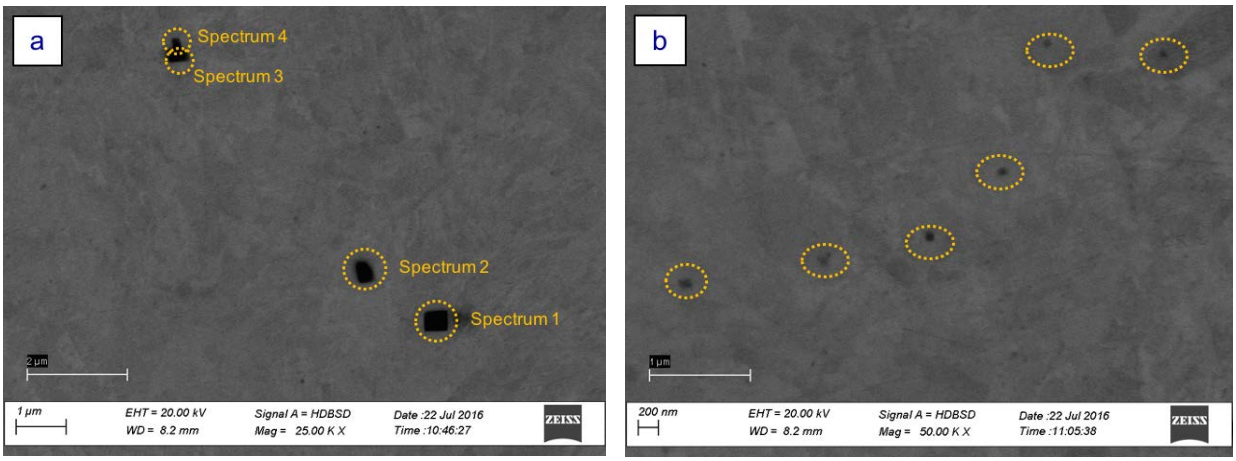

Figure 5.28. Large (a) and small (b) TiN particles observed with BSD (Ti54 at 900°C)

Table 5.10. EDS analysis spectra for large precipitates shown in Figure 5.32 (a)

Element	Spectrum 1		Spectrum 2		Spectrum 3		Spectrum 4	
	wt%	at%	wt%	at%	wt%	at%	wt%	at%
N	23.61	51.38	18.28	43.35	26.62	55.36	25.15	53.46
Ti	76.39	48.62	81.72	56.65	73.38	44.64	74.85	46.54

Figure 5.29 includes backscattered-electron images for Ti29 and Ti54 form isothermal condition at 1200°C; some TiN particles observed are encircled in the image. It is important to notice that the magnification for this condition is lower compare to the images shown in Figure 5.28.

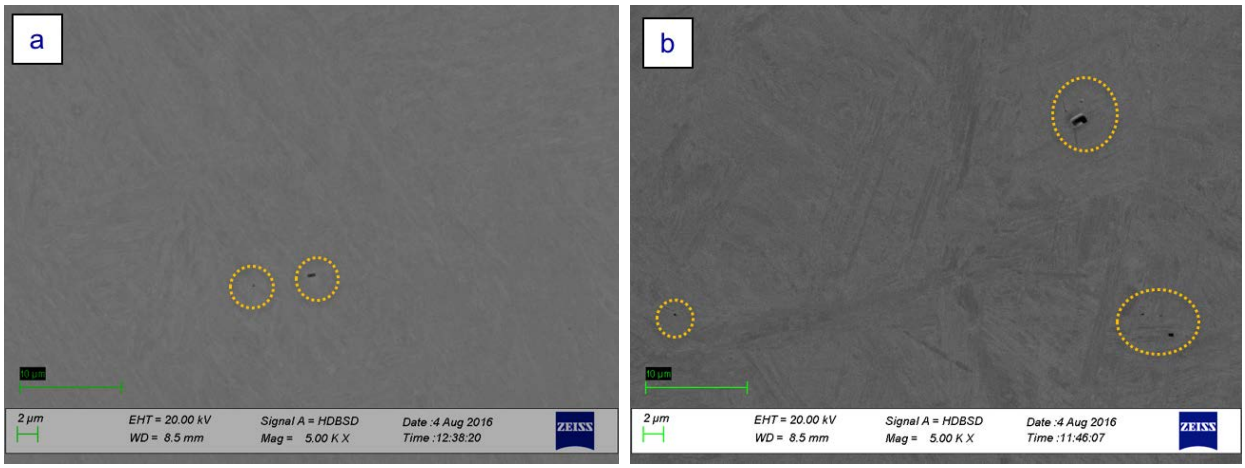

Figure 5.29. TiN precipitates observed in Ti29 (a) and Ti54 (b) with BSD (1200°C condition)

Figure 5.30 presents representative BF images of Ti29 and Ti54 systems from isothermal treatment at 1200°C, TiN particles are encircled in red.

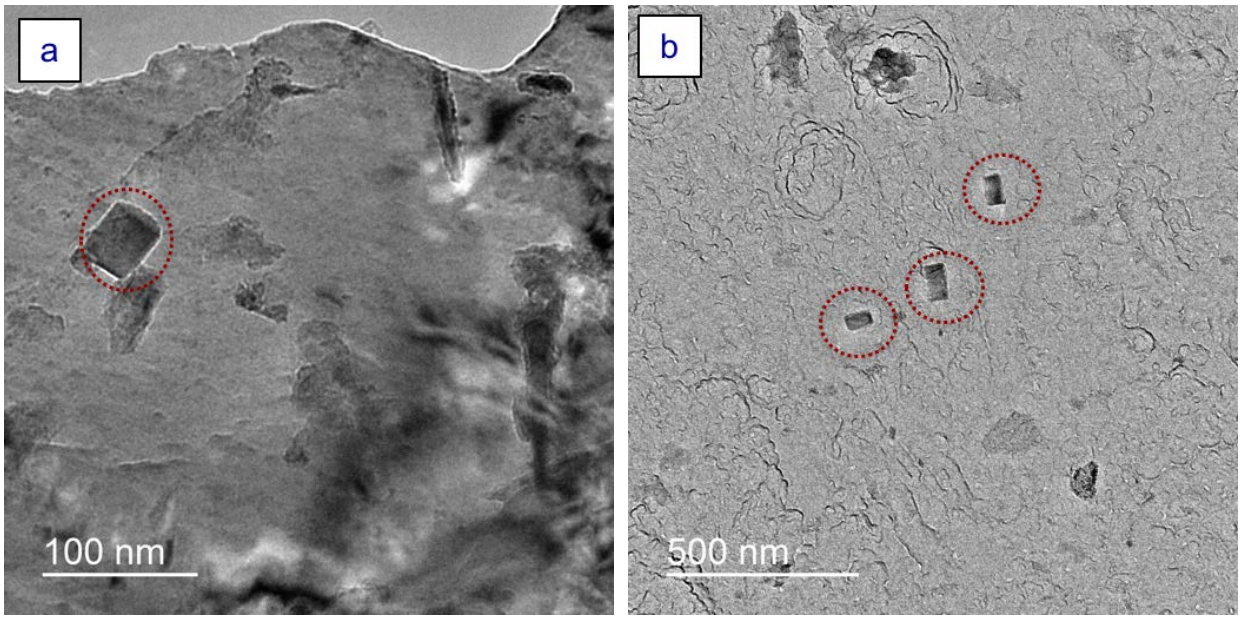

Figure 5.30. BF images of Ti29 (a) and Ti54 (b) showing TiN precipitates (1200°C PAGS condition)

Figure 5.31 shows backscattered-electron images for Ti29 and Ti54 from isothermal condition at 1300°C. TiN particles are encircled in the images. Figure 5.32 shows representative bright field images of usual absence of TiN precipitates in Ti29 and Ti54 from samples isothermal condition at 1350°C.

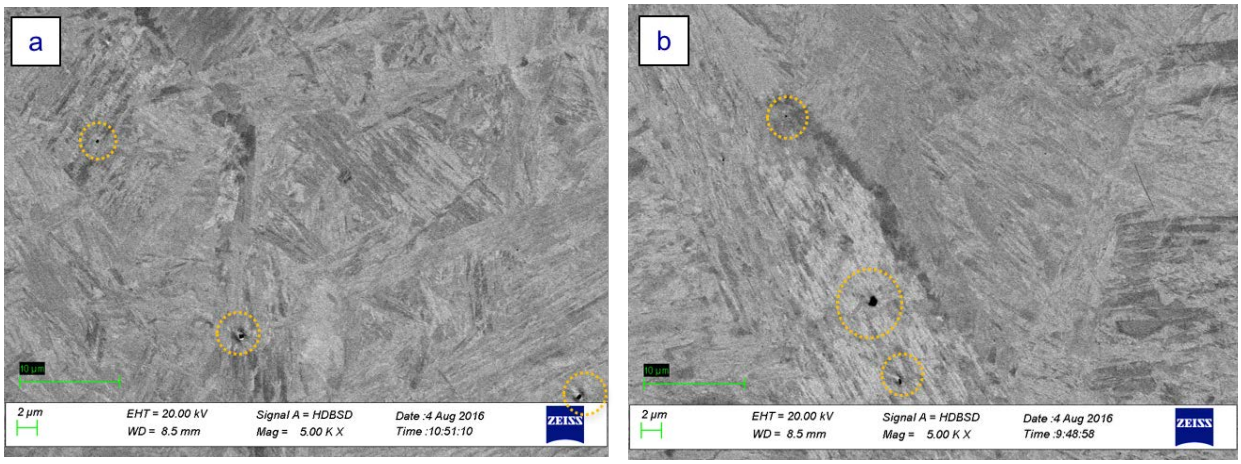

Figure 5.31. TiN precipitates observed in Ti29 (a) and Ti54 (b) with BSD (1300°C condition)

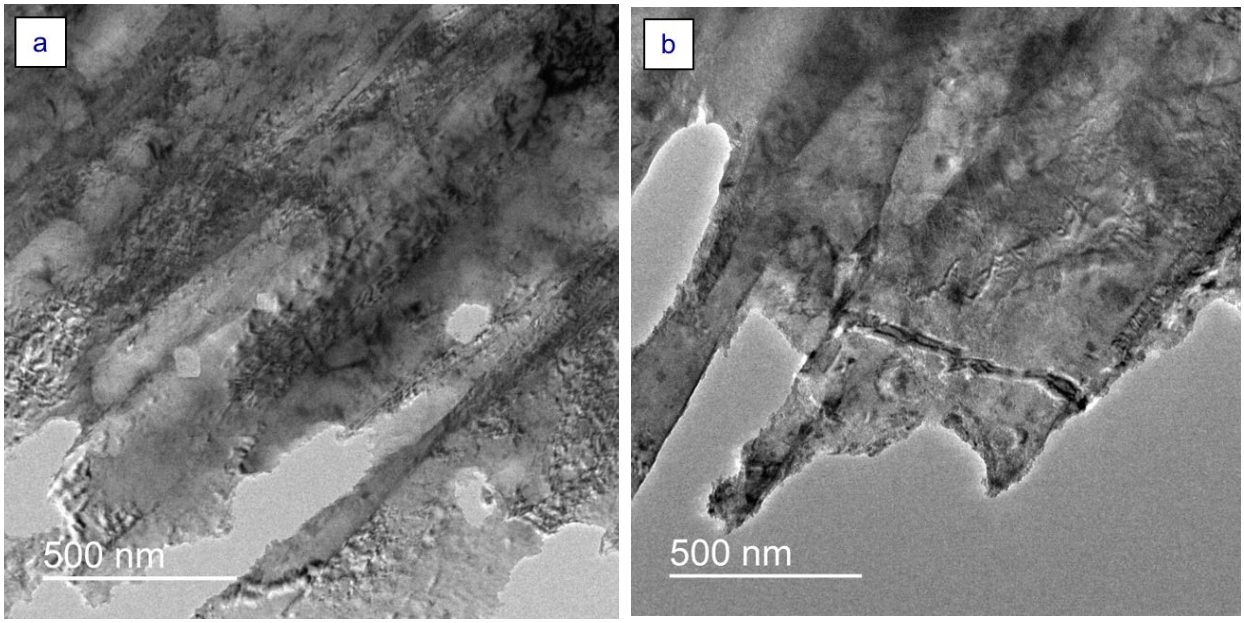

Figure 5.32. Representative BF images of Ti29 (a) and Ti54 (b) from 1350°C PAGS condition

It is important to mention that besides some Al_2O_3 and MnS particles, only TiN particles where observed on thin foils from 1200°C and 1350°C isothermal conditions for both Ti29 and Ti54 systems.

5.2.5 Effect of Initial Condition on Austenite Grain Growth Behavior

Table 5.11 presents a summary of the austenite grain size measurements from samples of the three alloy systems at 1,200°C and 1,350°C that were previously subjected to a fixed quenching and tempering (Q+T) condition, the results obtained at the same isothermal treatments from as-rolled conditions is also included. A difference in the austenite grain size behavior was observed for the 1,200°C condition for the Ti-bearing systems, while the 1,350°C condition presents no significant variation with respect to the same isothermal reheating from the as-rolled condition.

Table 5.11. Comparison of AGS from as-rolled condition and Q+T condition

Holding Temp (°C)	Initial Condition	TiF		Ti29		Ti54	
		D (μm)	Std Dev	D (μm)	Std Dev	D (μm)	Std Dev
1200	As-rolled	336.51	165.83	96.74	48.97	93.13	40.87
	Q+T	344.25	177.50	62.80	29.19	68.60	33.13
1350	As-rolled	505.58	203.12	486.21	223.30	335.47	187.37
	Q+T	533.12	233.02	476.36	182.32	274.44	117.07

Figures 5.33 and 5.34 show micrographs comparing the differences between the effect on the final austenite grain size from the as-rolled and quenched and tempered initial conditions for the three the systems.

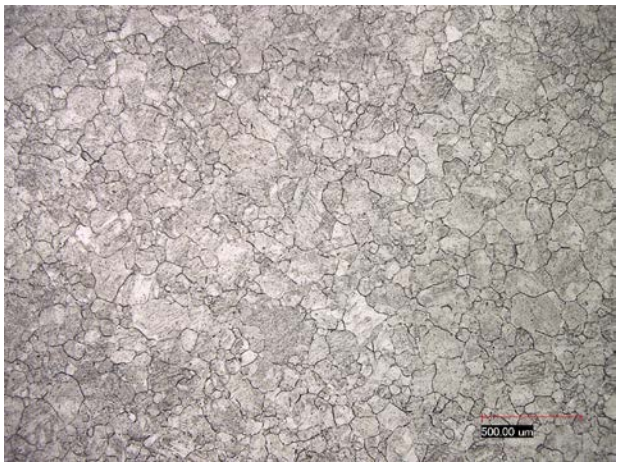

(a) Ti29 from as-rolled

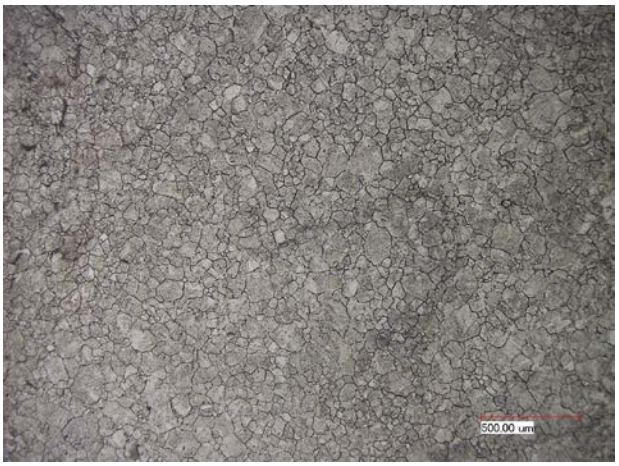

(b) Ti29 from quenched and tempered

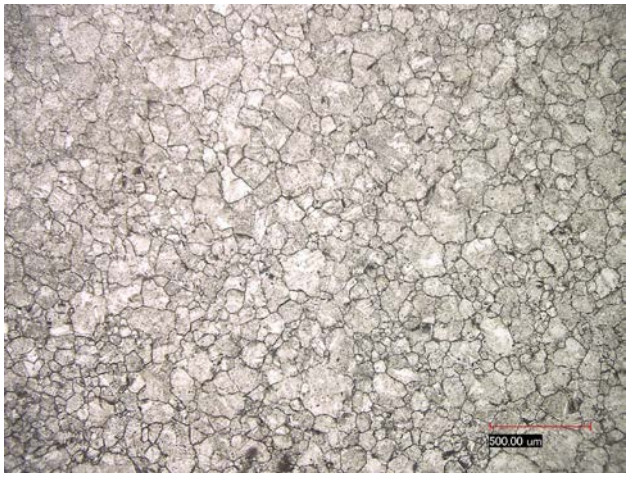

(c) Ti54 from as-rolled

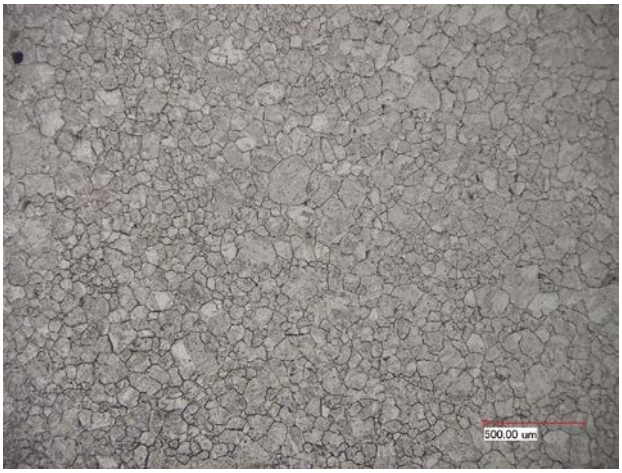

(d) Ti54 from quenched and tempered

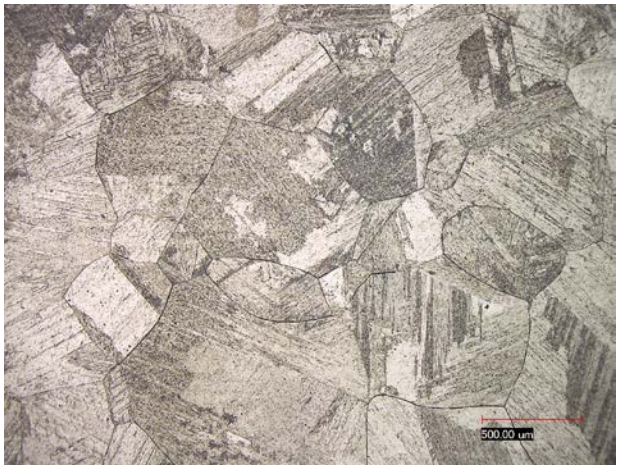

(e) TiF from as-rolled

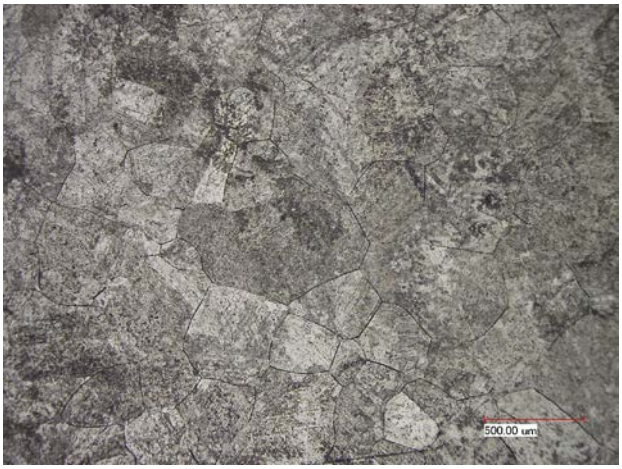

(f) TiF from quenched and tempered

Figure 5.33. Effect observed of initial microstructural condition on PAGS at 1200°C

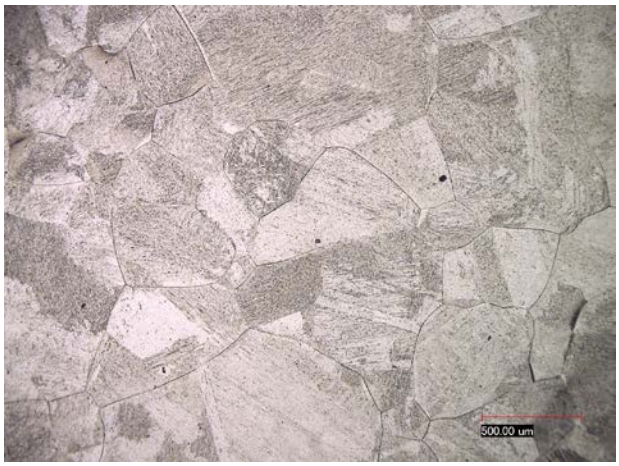

(a) Ti29 from as-rolled

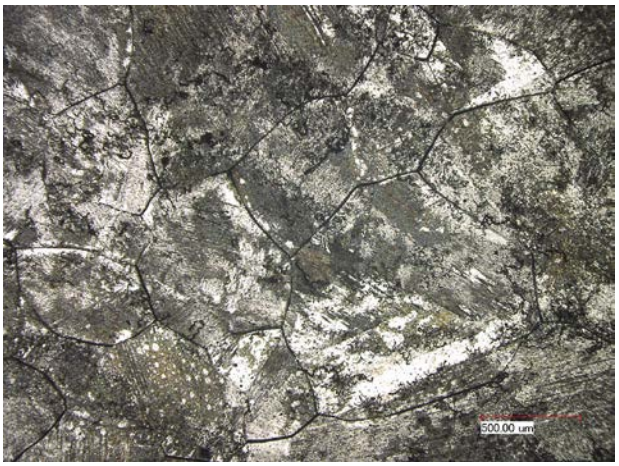

(b) Ti29 from quenched and tempered

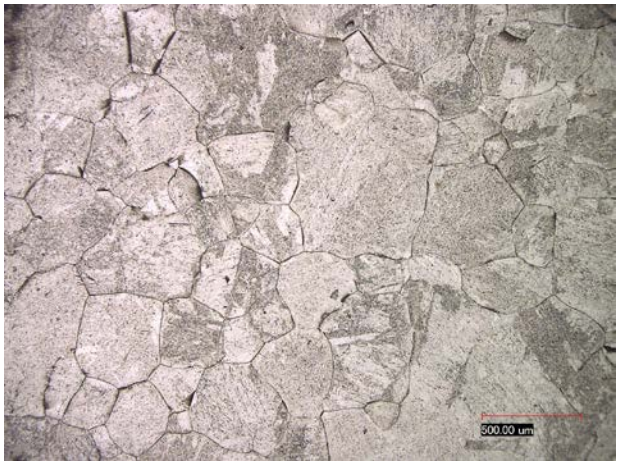

(c) Ti54 from as-rolled

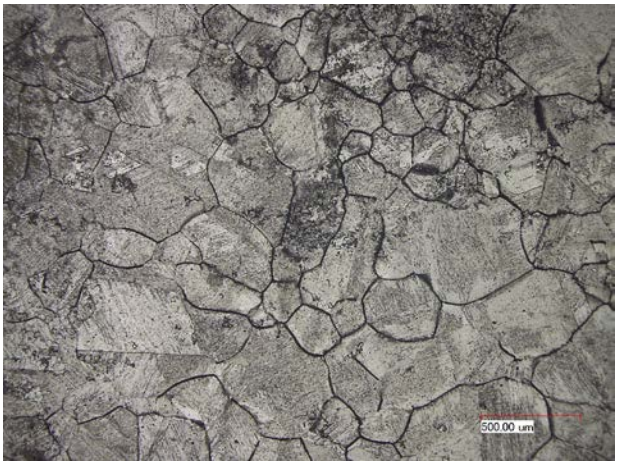

(d) Ti54 from quenched and tempered

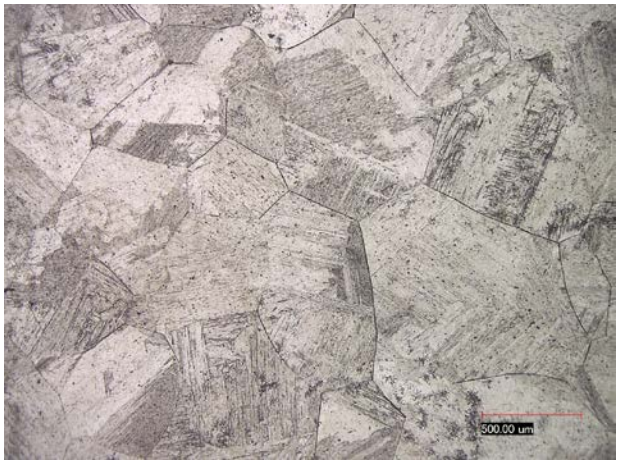

(e) TiF from as-rolled

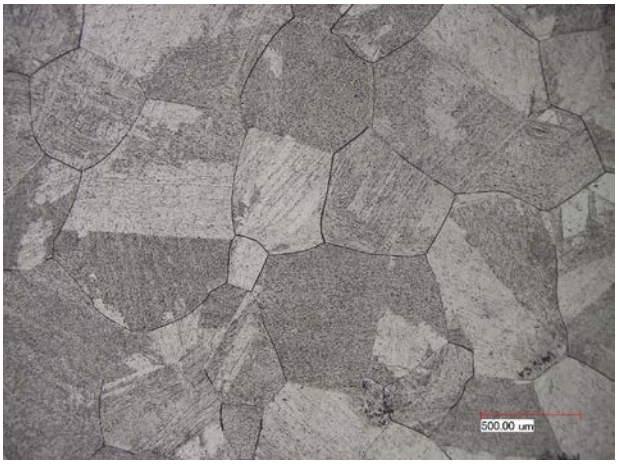

(f) TiF from quenched and tempered

Figure 5.34. Effect observed of initial microstructural condition on PAGS at 1350°C

At a holding temperature of 1350°C no significant difference in the effect of initial microstructural condition on the PAGS was observed for the three alloy systems which suggest that at this holding temperature and time the austenite grain coarsening behavior is basically independent of the initial microstructure.

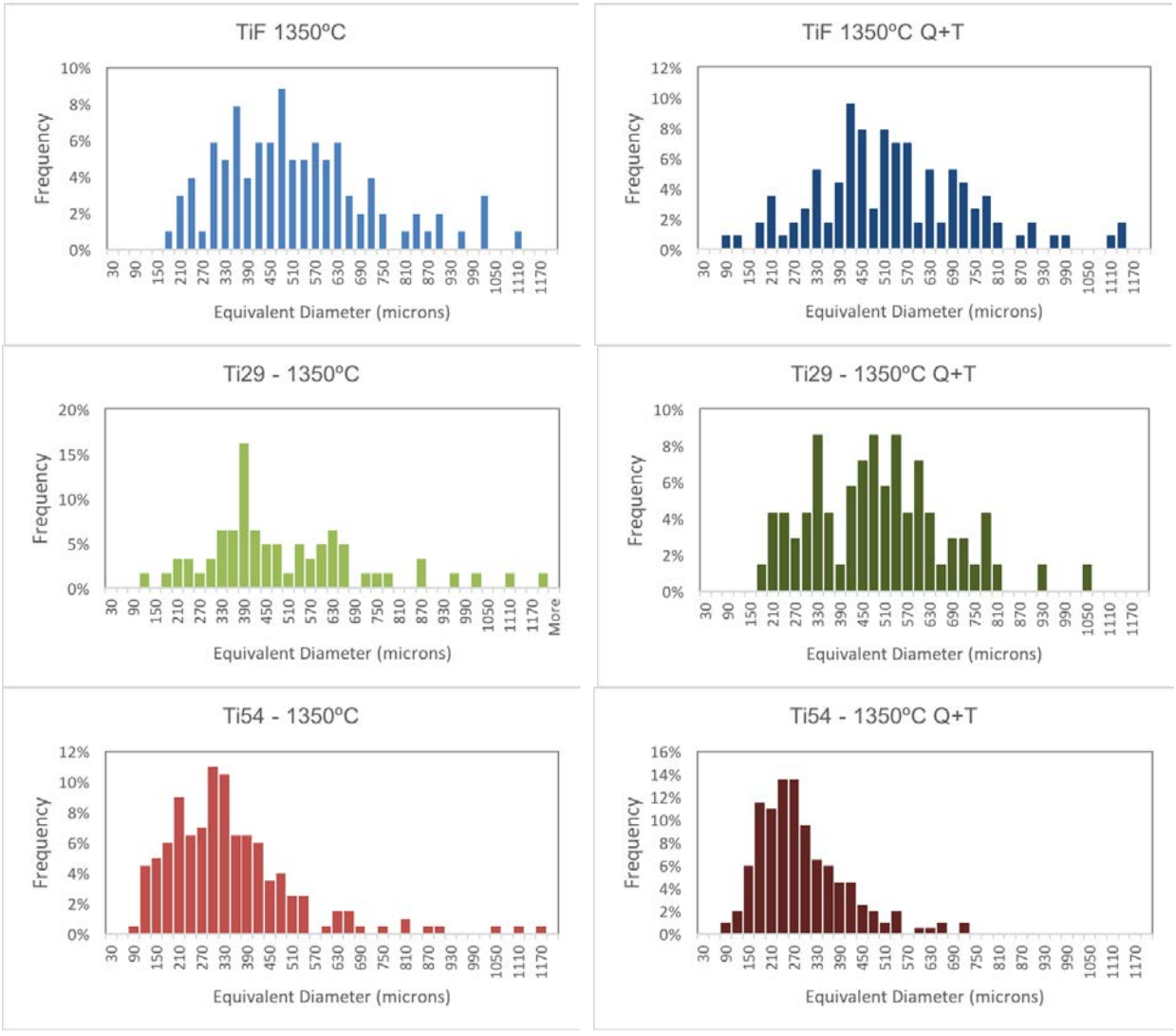

Figure 5.35. Frequency histograms for initial condition effect on PAGS at 1350°C

5.2.6 Effect of Heating Rate on Austenite Grain Coarsening Behavior

Figures 5.36 and 5.37 present the comparison between isothermal holding at 1350°C with 30min soaking condition and high heating rate effect (350°C/s to peak temperature of 1350°C with 1 s of soaking). The initial state for all samples was a quenched and tempered microstructure. Austenite grain size values are compared in Table 5.12.

Table 5.12. Comparison of AGS from as-rolled condition and Q+T condition

Condition	Ti29		Ti54	
	D (µm)	Std Dev (µm)	D (µm)	Std Dev (µm)
Isothermal 1350°C HR-10°C/s 30 min soaking time	476.36	182.32	274.44	117.07
HR=350°C/s to peak temperature of 1350°C 1 s soaking time	146.61	55.14	102.29	41.73

Figure 5.38 shows a comparison of the AGS between Ti29 and Ti54 after the high heating rate cycle. While there are differences observed in the austenite grain size, both systems presented a fairly uniform grain size distribution.

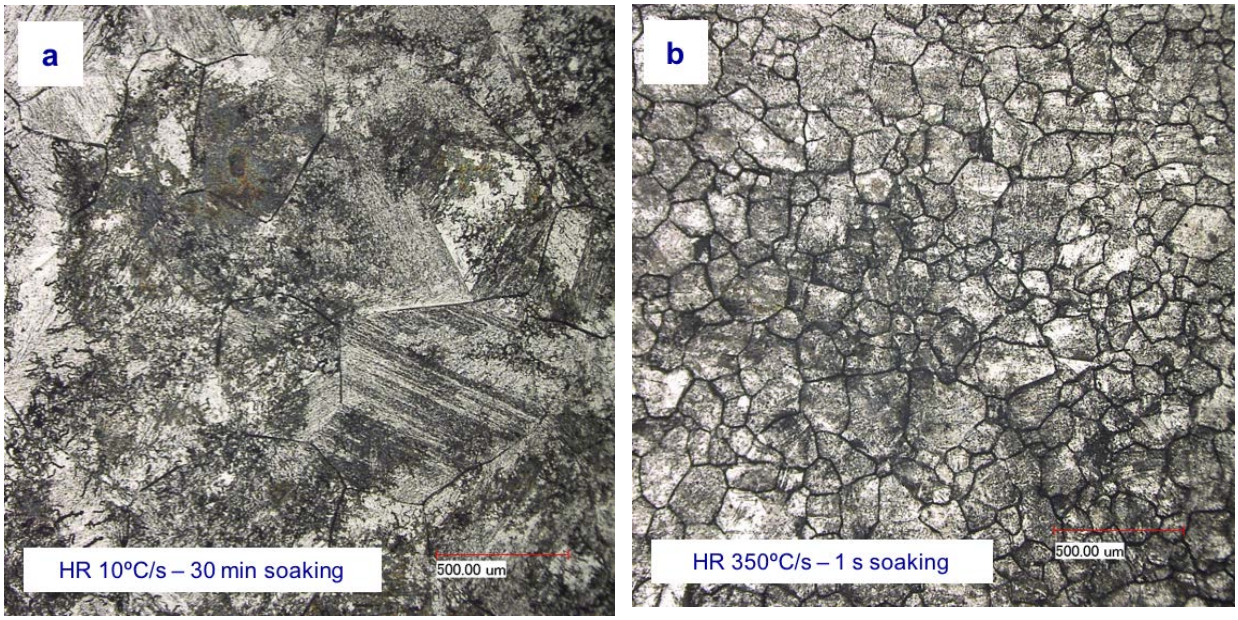

Figure 5.36. Effect of heating rate on PAGS – Ti29 alloy at 1350°C

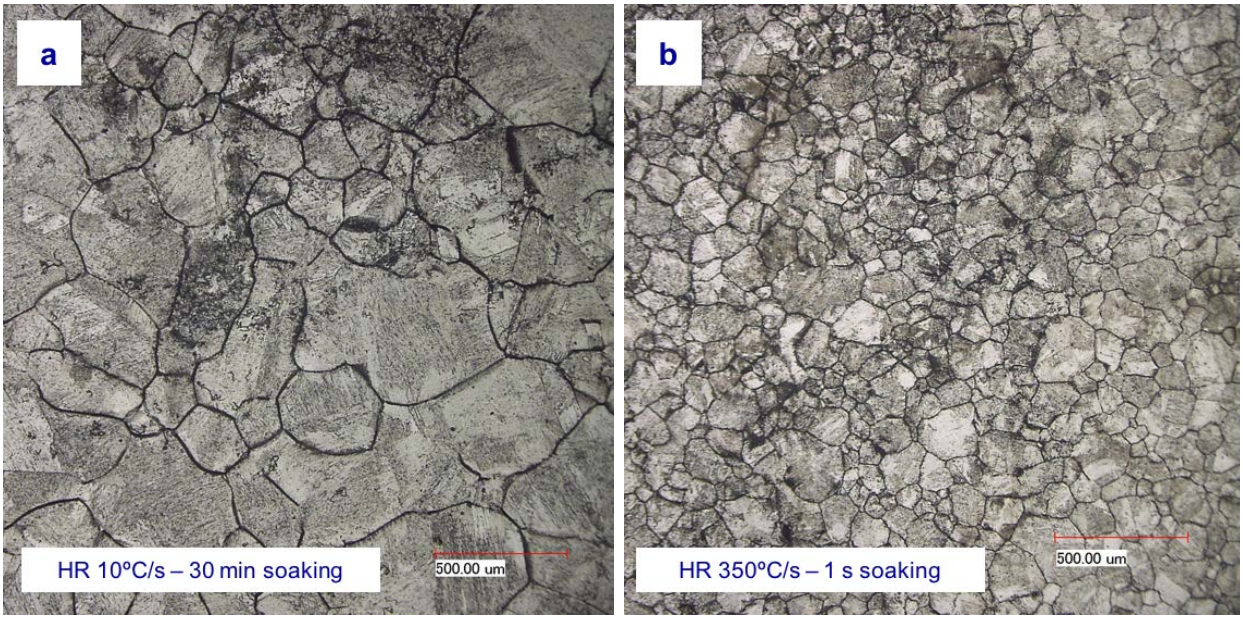

Figure 5.37. Effect of heating rate on PAGS – Ti54 alloy at 1350°C

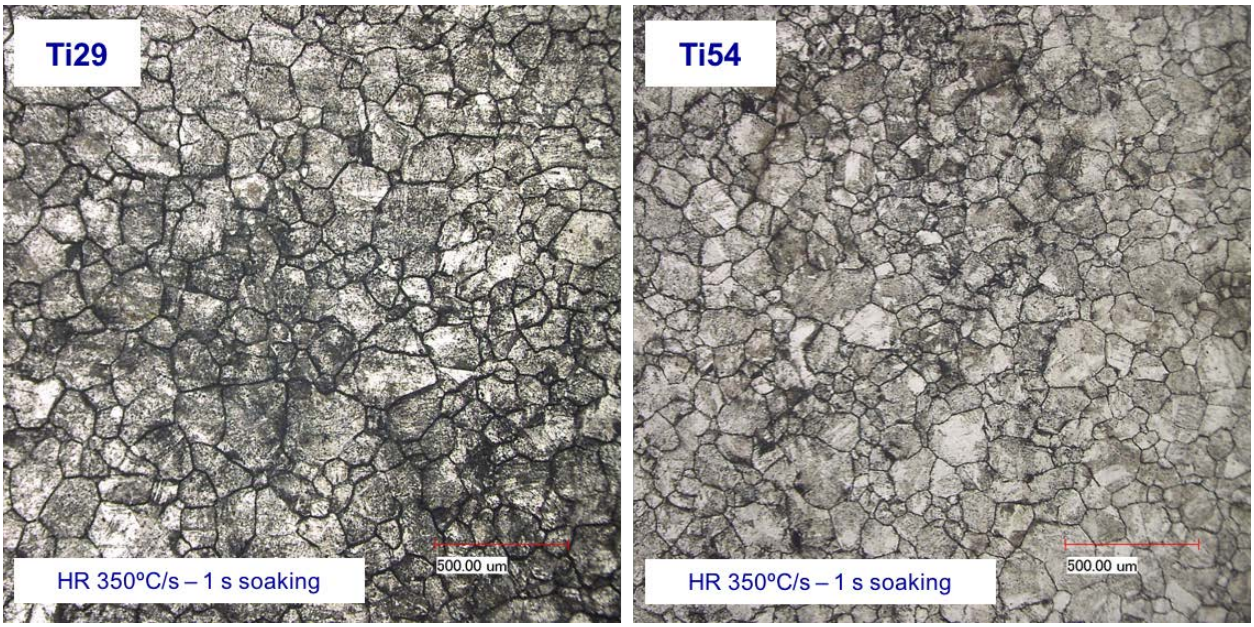

Figure 5.38. Comparison of Ti29 and Ti54 at high heating rate to peak temperature of 1350°C, 1s soaking

Figure 5.39 presents a comparison frequency histograms of the grain size distribution from the isothermal and high heating rate conditions for the Ti-bearing systems.

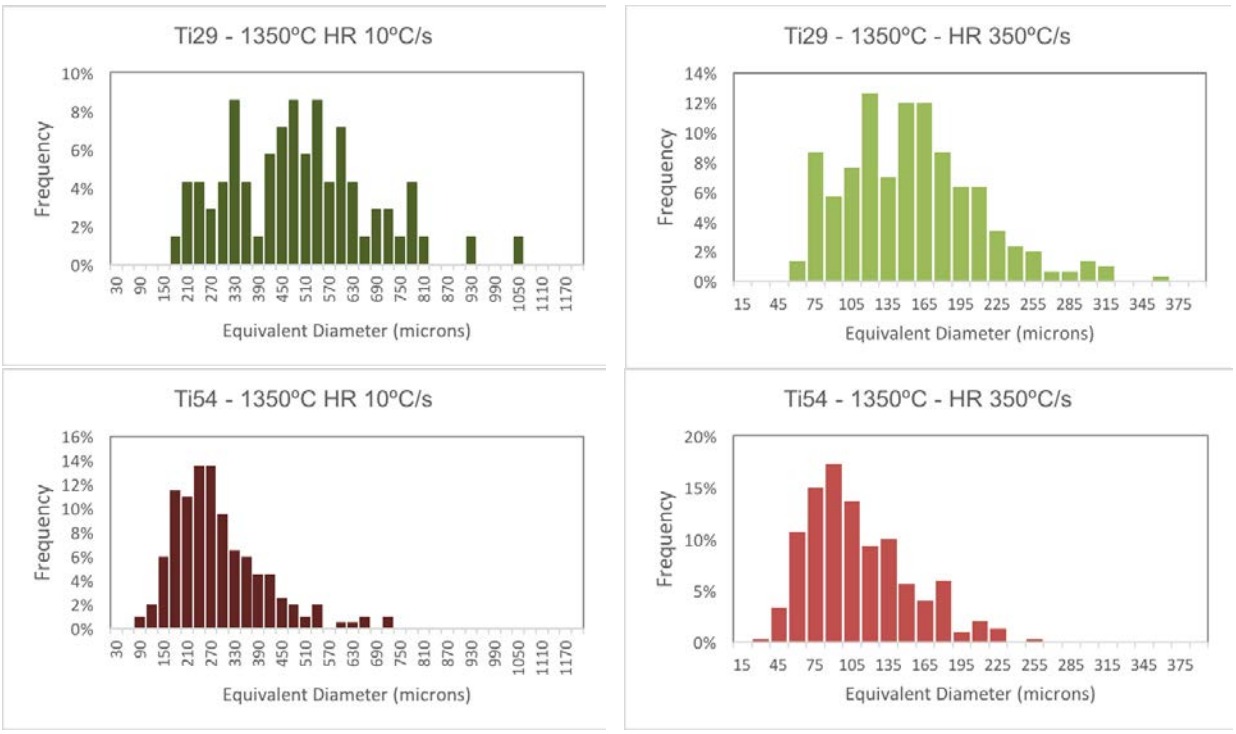

Figure 5.39. Comparison of Ti29 and Ti54 at high heating rate and isothermal at 1350°C

5.3 EBSD ANALYSIS DURING THE DISSOLUTION OF PRECIPITATES

5.3.1 Analysis Conditions Set-Up and Selection of Samples

Before running the EBSD scans for grain boundary character distribution analysis, a set of scanning tests were conducted in order to determine the optimal magnification, step size, the type of system (square of hexagonal) and the scanning area. These parameters were basically determined by the known austenite grain size of the sample, and the dominant martensitic microstructure features with a primary austenite grain size boundary present in the samples.

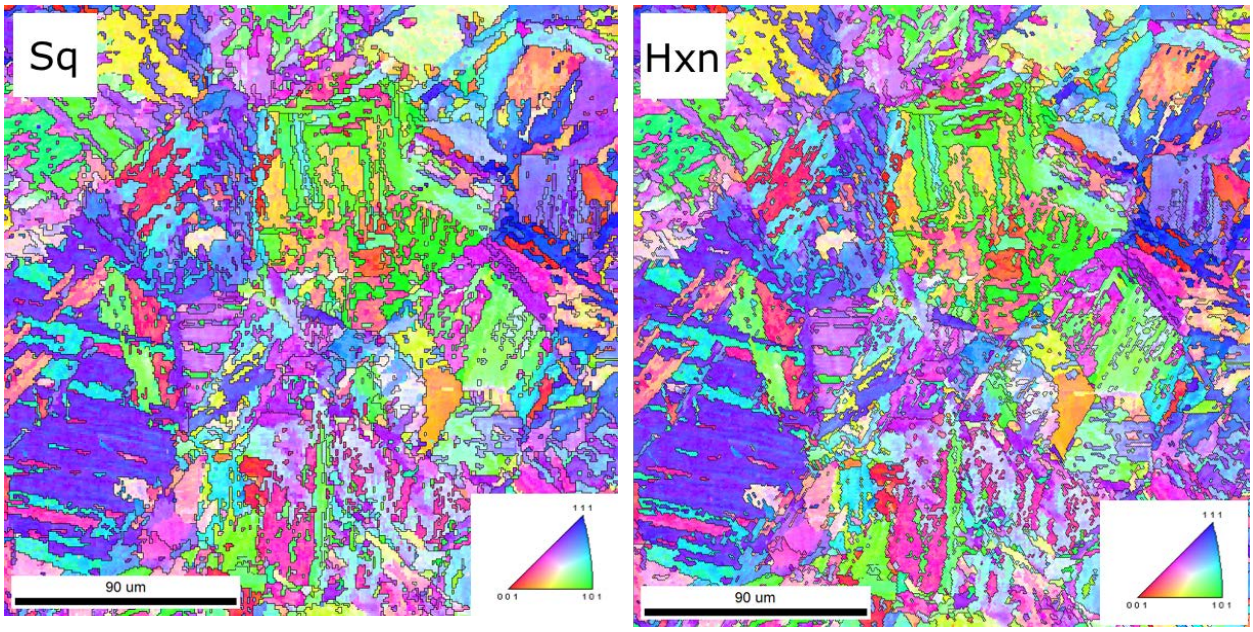

Figure 5.40. Comparison of IPF between square (Sq) and Hexagonal (Hxn) scan system.

Figure 5.40 presents a comparison between the inverse pole figures (IPF) obtained with the square scanning system and the hexagonal scanning system with a step size of 0.8

μm and scanned area of 250 μm x 250 μm for the Ti54 alloy system with holding temperature of 1200°C from isothermal heat treatments. As it can be observed, the hexagonal scan system presented a better delimitation in the austenite grain boundaries compared to the square scan system.

Figure 5.41 presents a scan test conducted on TiF system (900°C from isothermal heat treatment) to evaluate the step size for the samples from isothermals at 900°C that resulted in an average grain diameter between 15 and 20 μm. The step sizes tested for this condition were 0.2 μm, 0.4 μm, and 0.6 μm with scanned areas of 100 μm x 100 μm, 120 μm x 120 μm, and 150 μm x 150 μm, respectively.

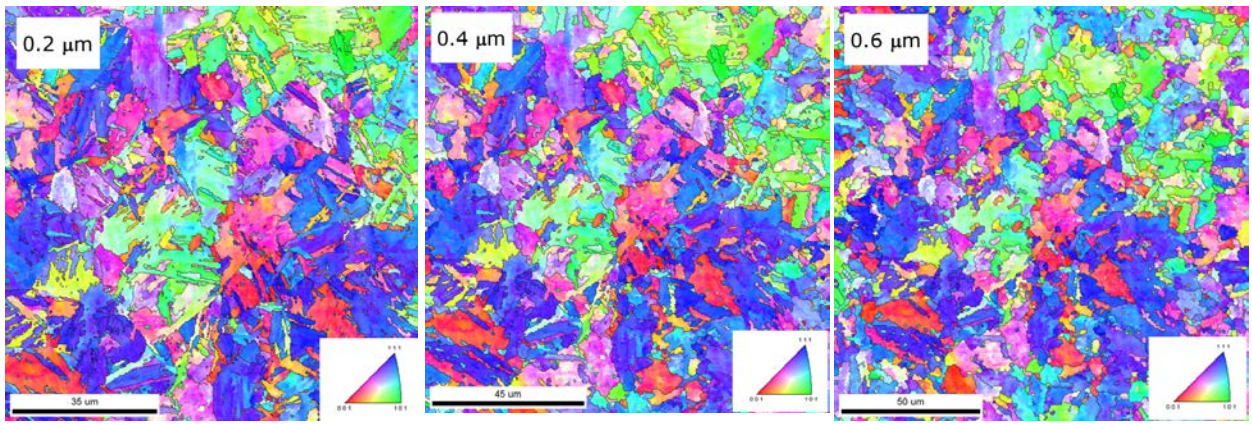

Figure 5.41. IPF of step size test for 900°C condition (TiF system)

The increase on step size allows to run the EBSD scans on larger sample areas without increasing the scanning time, however, for the step sizes tested the increase in area resulted in a reduction in the grain boundary delimitation as well as a gradual decrease in the confidence index. Figure 5.42 presents the scan test conducted on specimen from 1200°C isothermal condition to evaluate the step size for the samples with an average grain

size close to 100 μm. The step sizes tested for this condition were 0.4 μm, 0.8 μm, and 1.6 μm with scanned areas of 250 μm x 250 μm for all step sizes. For this condition, the step size of 0.4 μm was chosen since it provided better delimitation of the grain boundaries as well as microstructural features.

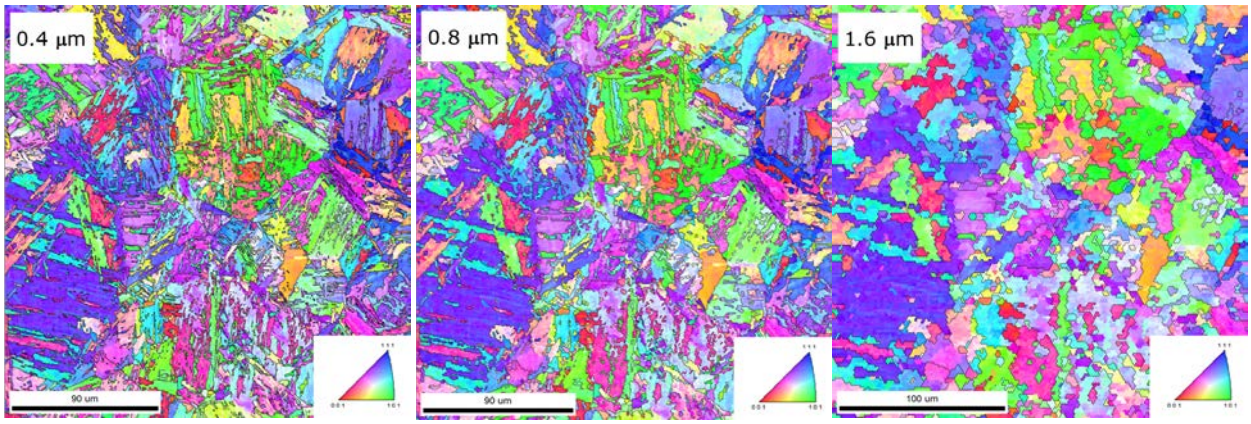

Figure 5.42. IPF of step size test for 1200°C condition (Ti54 system)

Figure 5.43 illustrates the selection of samples for grain boundary character distribution analysis through EBSD based on the PAGS study results.

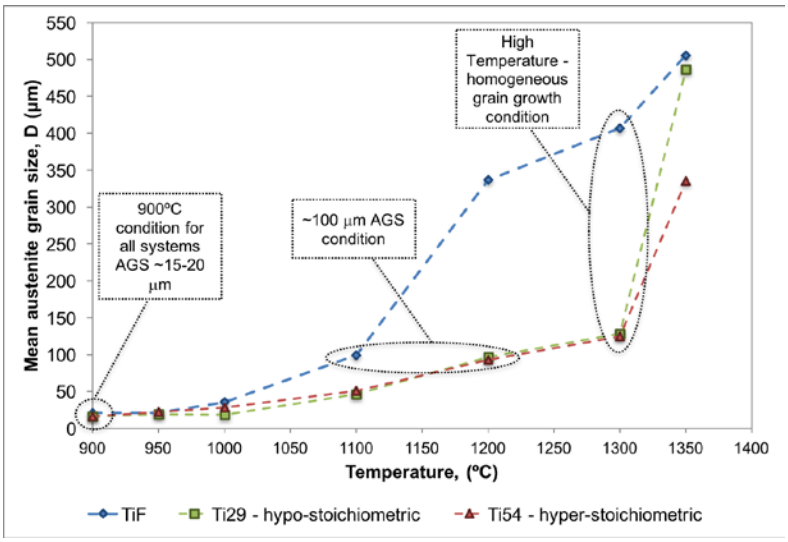

Figure 5.43. Selection criteria of samples for EBSD analysis based on PAGS results

Samples from 900°C condition were scanned on an area of 100 µm x 100 µm with a step size of 0.2 µm. For the 100 µm AGS condition (1200°C for Ti29 and Ti54, and 1100°C for TiF) the scanned area selected was 250 µm x 250 µm and a step size of 0.4 µm. for the 1300°C condition the scanned area selected was 250 µm x 250 µm for Ti29 and Ti54 and 300 µm x 300 µm for TiF. Appendix A includes a summary of the EBDS data for OIM analysis.

5.3.2 Grain Boundary Character Distribution on Selected Conditions

For the OIM analysis, the misorientation angle criteria for all conditions tested was as follows:

- 2° – 20°: Low angle boundary.
- 20° – 45°: High angle boundary with misorientation from 20° to 45° or High mobility boundaries (HMB). Based on approach by Tao et al. [49]

- >45°: High angle misorientation.

Figure 5.44 presents the EBSD analysis results for the 900°C condition from the isothermal experiments. Red lines correspond to the misorientation angles from 20° to 45°, located at the grain and some sub-grain boundaries.

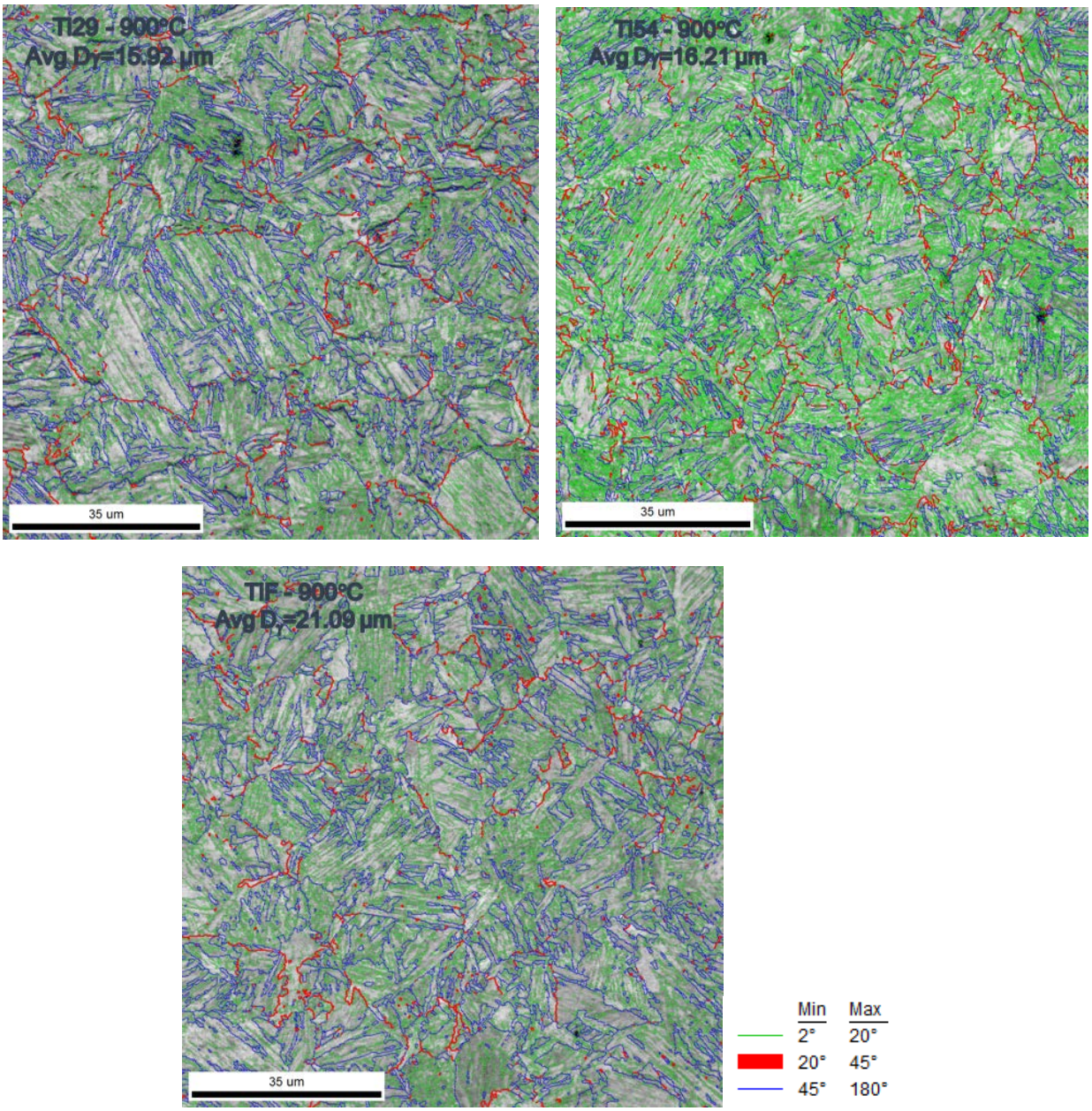

Figure 5.44. IQ misorientation angle results for 900°C condition

Figure 5.45 presents the EBSD analysis results for the condition that showed an average austenite grain size close to 100 µm on the three alloy systems, 1100°C for TiF and 1200°C for Ti29 and Ti54. from the isothermal experiments.

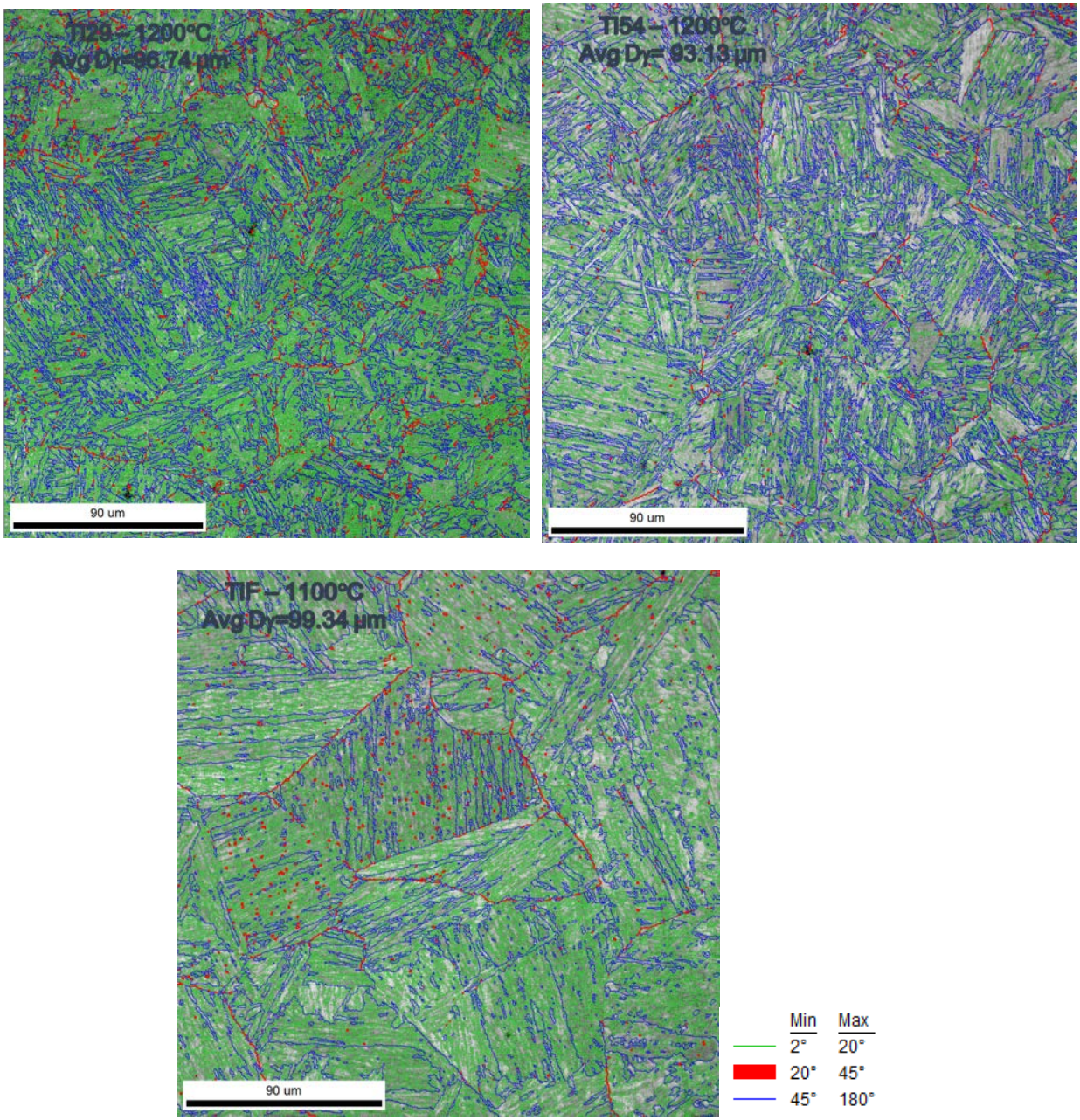

Figure 5.45. IQ misorientation angle results for 1100°C (TiF) and 1200°C conditions (Ti29 and Ti54)

Figure 5.46 the results for the 1300°C for the three systems. The average grain size diameter measured is indicated at the top left corner of each image.

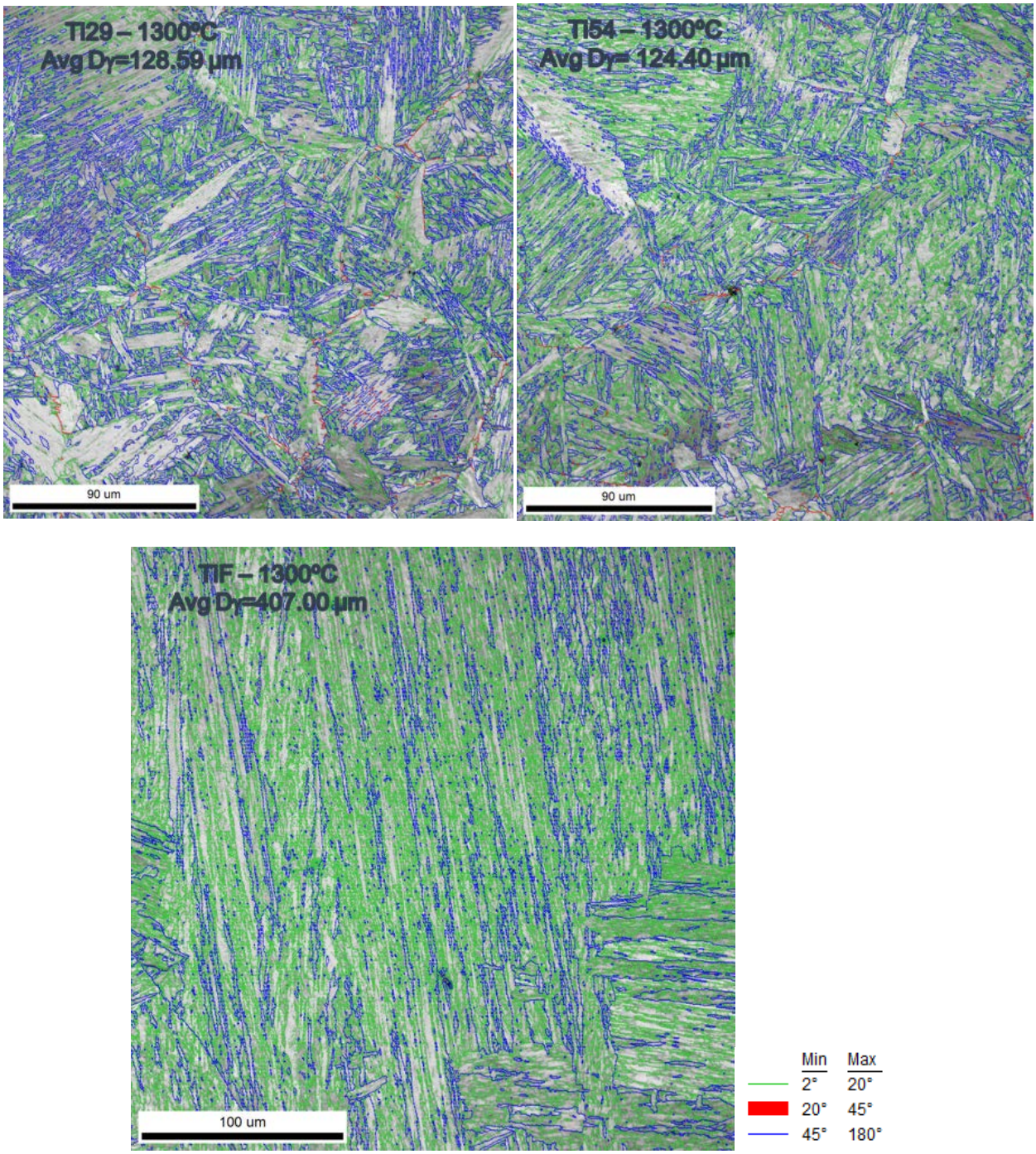

Figure 5.46. IQ misorientation angle results for 1300°C condition

Table 5.13 presents a summary of the fraction of misorientation angle ranges for the different conditions and alloy systems.

Table 5.13. Fraction of misorientation angle ranges obtained from EBSD for different isothermal conditions

Holding Temp. (°C) 30 min soaking	TiF			Ti29			Ti54		
	2°-20°	**20°-45°**	**>45°**	**2°-20°**	**20°-45°**	**>45°**	**2°-20°**	**20°-45°**	**>45°**
900	0.688	**0.037**	0.275	0.681	**0.041**	0.279	0.746	**0.046**	0.208
1100	0.800	**0.017**	0.183	-	**-**	-	-	**-**	-
1200	-	**-**	-	0.739	**0.026**	0.235	0.602	**0.016**	0.382
1300	0.782	**0.002**	0.218	0.52	**0.016**	0.464	0.651	**0.011**	0.338

According to the results obtained from EBSD analysis, the fraction of high angle boundaries between 20° and 45° (HMB) decreases with increasing the holding temperature for isothermal heat treatments. TiF system shows a faster decrease in the fraction of HMBs with a fraction of 0.016 at a holding temperature of 1100°C and a fraction of 0.002 at 1300°C. Ti29 and Ti54 showed a similar trend in the decrease of HMB. Figure 5.47 presents an overview of these results; the information of the measured average grain size diameter is also included.

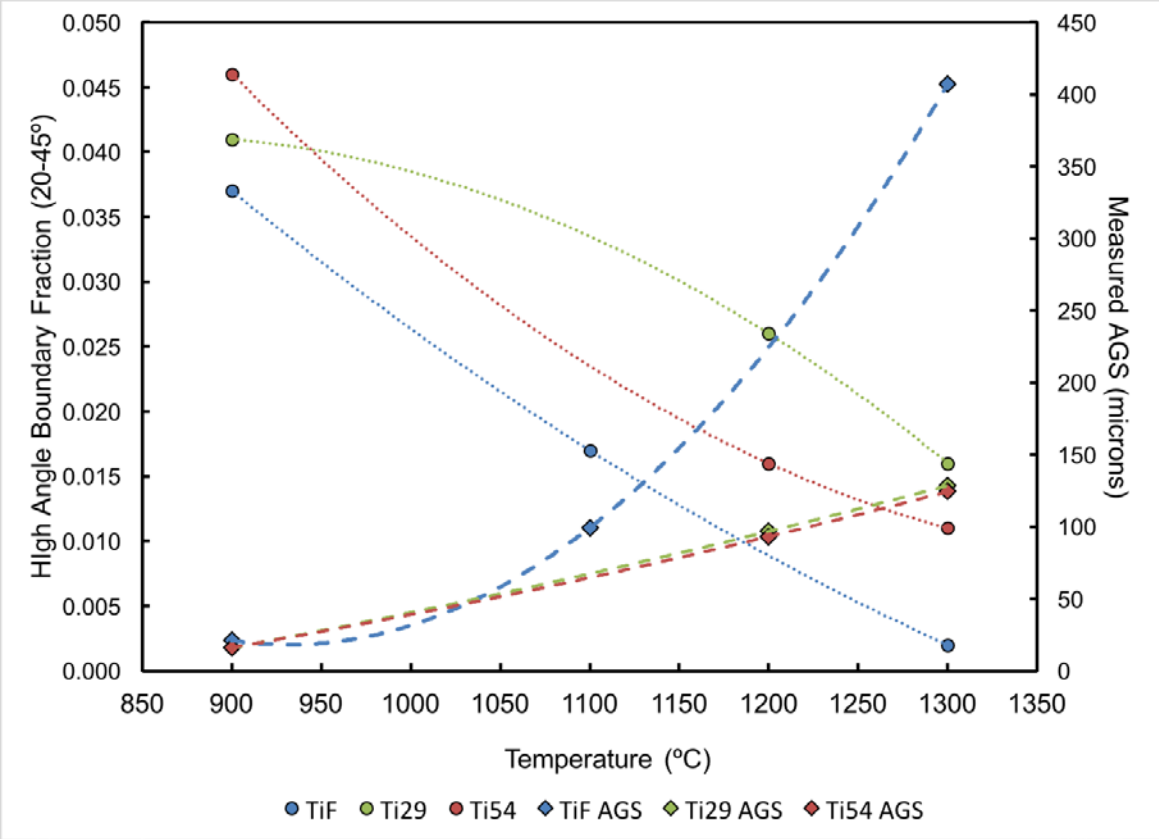

Figure 5.47. Fraction of HMB (HA boundaries 20°-45°) and measured AGS for different isothermal conditions

5.3.3 EBSD and SEM Systematic Analysis

A systematic analysis has been conducted with the information obtained from the grain boundary misorientation angle distribution and the SEM with backscatter detection. This was done with the aim of obtaining a correlation with the presence of TiN precipitates and the identified HMBs. Figure 5.48 presents an analysis on Ti29 system for the isothermal condition at 1300°C; image from IQ rotation angle analysis is presented to the left with black arrows indicating the presence of TiN particles which are also indicated in the SEM image to the right in yellow arrows. Dotted circles in both images represent cluster of TiN particles observed by SEM. Both IQ rotation angle and SEM images present the approximately the same scanned area at the same magnification. Some zones were labeled on the IQ image for further reference and discussion.

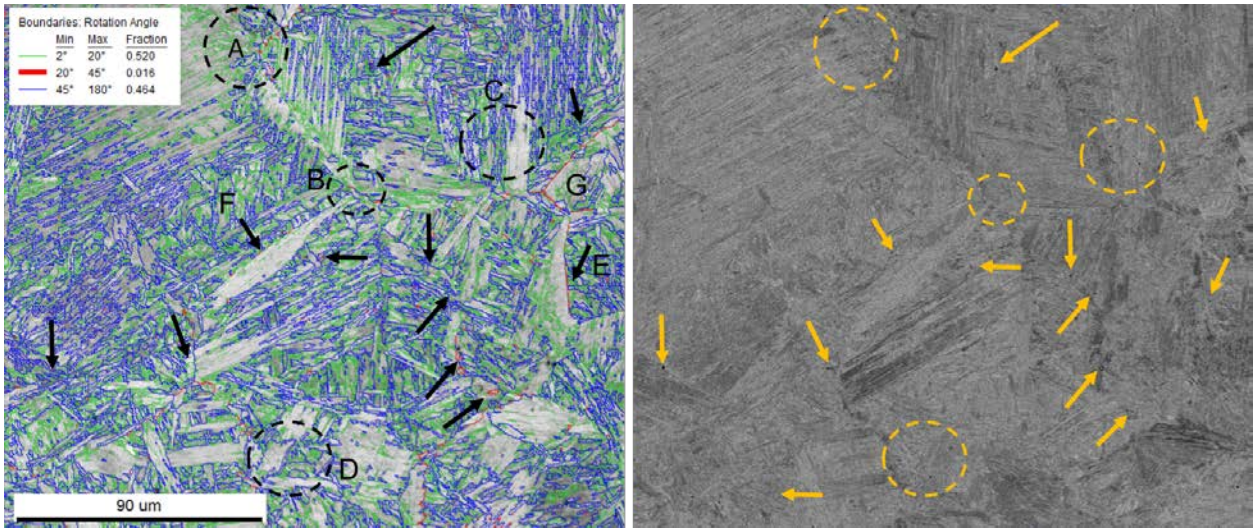

Figure 5.48. Systematic EBSD-IQ rotation angle analysis (left) and SEM-BSD analysis (right) for Ti29 with isothermal treatment at 1300°C

As it is observed in Figure 5.48, there seems to be a correlation between the presence of TiN particles and HMB. In some cases, there is presence of HMB with no TiN observed through SEM analysis (Zone G) which suggest that smaller particles might be present but cannot be observed at the presented magnification. Arrows labeled E and F correspond to small TiN particles specifically observed on the SEM at higher magnification. It can be noticed in Figure 5.48 that these small particles appear to be closer to the HMB compared to many of the large particles analyzed. Figure 5.49 presents a similar analysis on Ti54 system for the isothermal condition at 1300°C.

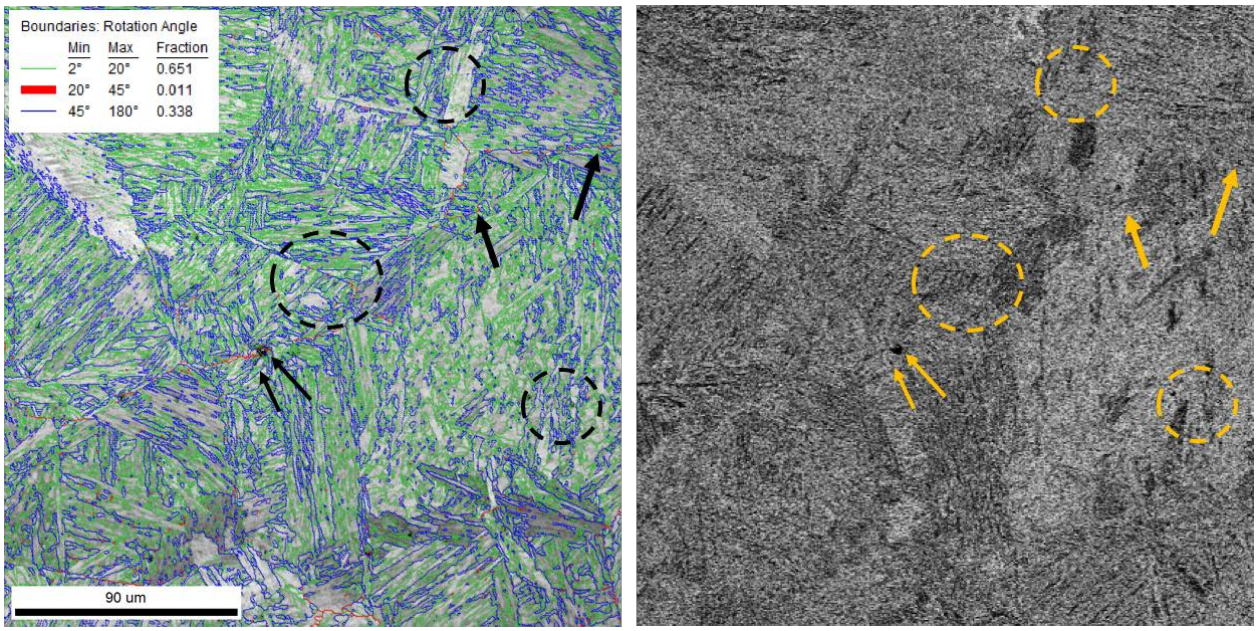

Figure 5.49. Systematic EBSD-IQ rotation angle analysis (left) and SEM-BSD analysis (right) for Ti54 with isothermal treatment at 1300°C

5.4 ELECTRON PROBE MICROANALYZER RESULTS

Electron probe micro-analysis was conducted on samples from isothermal treatments at 1200°C in the Ti-bearing systems with the aim of exploring a quantitative experimental method for determining the concentration variation of Ti as a diffusion rate controlling solute in the TiN particle coarsening behavior.

For the Ti54 system a line scan was performed with 51 positions every 3 μm along several grain boundaries detected by back scattered electrons. Figure 5.50 includes an image of the line scan and the results of the Ti concentration. Dotted lines in the concentration graph indicate the locations of the austenite grain boundaries.

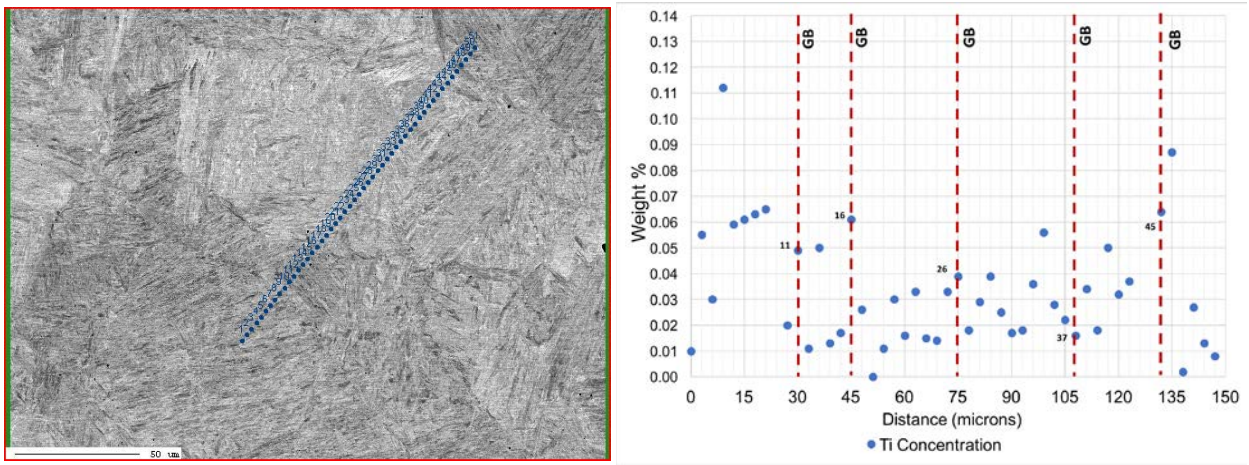

Figure 5.50. EPMA line scan along grain boundaries on isothermal condition of 1200°C for Ti54

For the Ti29 system the line scan was performed on 22 positions every 5 μm also along several grain boundaries detected by back-scattered electrons. The image of the line scan and Ti concentration analyzed are presented in Figure 5.51.

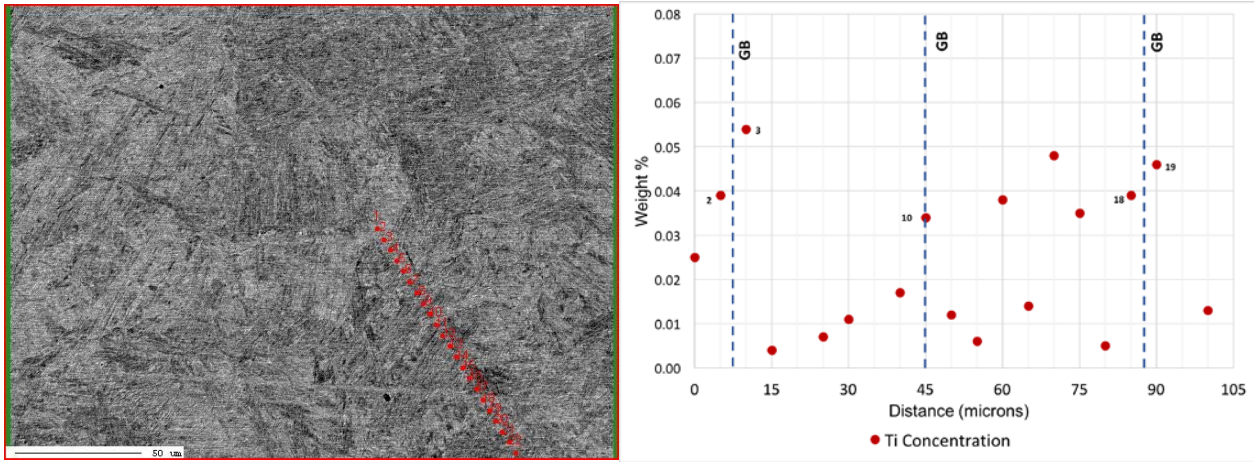

Figure 5.51. EPMA line scan along grain boundaries on isothermal condition of 1200°C for Ti29

Based on the information obtained from the microanalysis, some peaks of Ti concentration are observed near the grain boundary locations, although some other peaks are also observed inside the observable austenite grains. While there was a high concentration variation observed in both Ti-bearing alloys, Ti54 system showed a higher variation compared to Ti29 which would be expected as the former system is anticipated to have more dissolved Ti in the matrix. It was difficult to conclude that the amount of Ti was tied to TiN or available in solid solution, however, the relative differences observed in the Ti concentration near grain boundaries suggest possible differences in the energy and nature of the grain boundaries.

6.0 DISCUSSION

6.1 INITIAL STATE ASSESSMENT

According to thermodynamical models and experimental values from many references, precipitate size is expected to be smaller if precipitation of titanium takes place in the solid state [23]. For this study it was anticipated that precipitates present in the as-rolled condition for the Ti-bearing systems would have formed after solidification of the ingots. Nevertheless, the presence of some large cuboidal and rectangular-shaped TiN (between 200 nm and 0.7 μm in size), particularly in Ti54 system, suggests that these particles might have been formed during solidification at interdendritic regions with higher concentration of Ti; this has been already reported in the literature [25, 37, 46]. Both Ti29 and Ti54 SEM and TEM analysis showed presence of these large TiN precipitates (in larger amount in Ti54.) These observations support the recommendations about additions of Ti that result in a Ti/N ratio below and close to the stoichiometric condition since the higher the Ti concentration for a similar N content the higher the probability of forming TiN during the solidification process. These TiN precipitates formed during solidification will be stable along the subsequent processes with the possibility of coarsen under heat treatment conditions that allow dissolution of Ti [10]. In their study, which included larger concentration of Ti compared to this study, Shen and Hansen [45] conclude that there is a

linear relationship between the product of Titanium and Nitrogen concentration ([T]*[N]) and the presence of coarse TiN particles which they claim to be responsible of a reduction in toughness properties.

Irregular-shaped precipitates together with cubic TiN precipitates (NaCl crystal structure and a lattice parameter of 4.232 Å) observed in the as-rolled condition for the Ti54 and T29 were also reported by Liu and Liao [39] on Ti-V micro-alloyed steels at a temperature of 1065°C and were identified as (Ti, V)N and more generally as complex precipitates bearing Ti, V, C, Al, among others. In this study, the presence of Mo-V rich Ti-based irregular-shaped particles of finer size in the as-rolled condition (Section 5.3.1.) and the absence of these particles in PAGS condition at 1200°C (Section 5.2.4) suggests that they do not have a role in exerting pinning forces in the high temperature range.

6.2 AUSTENITE GRAIN COARSENING BEHAVIOR

6.2.1 Effect of Ti-Microalloying content and stoichiometry

Overall the austenite grain coarsening pinning effect, in particular at higher temperatures, was clearly observed on the Ti-bearing systems. This behavior is in agreement with the information found in the literature with respect to Ti-microalloyed steels and its role on the austenite grain growth [6, 9, 10, 23, 42, 55]. In the present study it was possible to visualize this effect by comparison with the Ti-free system which started to show grain coarsening at lower isothermal holding temperatures.

Even though both hypo and hyper-stoichiometric conditions showed a similar grain coarsening behavior, the hyper-stoichiometric alloy design showed a stronger bimodal grain structure which resulted in a higher grain size standard deviation compared to the hypo-stoichiometric condition. This condition leads to a less effective localized pinning force exerted on grain boundary mobility.

6.2.2 Stability of Precipitates and Coarsening during Isothermal Treatments

For the estimation of TiN volume fraction, differences in the adequate amount of precipitates on exerting pinning forces for austenite grain size control can be found among the literature mainly because the choice of the solubility product, one example is the work conducted by Medina et al. [10] in which they make use of Turkdogan's solubility product (see Table 2.2) and considered that a TiN volume fraction of 1.75×10^{-4} is insufficient for adequate grain size control at an isothermal treatment of 1300°C with 10 minutes of holding time, while in the present study, homogeneous controlled grain size on both Ti29 and Ti54 was observed at the same temperature with a holding time of 30 minutes and estimated volume fractions of 1.10×10^{-4} and 1.42×10^{-4} (see Figure 5.28), respectively, in accordance with Inoue et al. solubility product. It is important to mention that the alloy composition used by Medina et al. did not include alloying elements such as Cr, Ni, and Mo that could provide grain boundary mobility resistance by solute drag effect. Figure 6.1 shows the changes in the predicted austenite grain size by changing the solubility product (from Table 2.2) in the estimation of volume fraction of TiN; LSW equation (Equation 2.11)

was used for particle coarsening and the Gladman's model for grain coarsening behavior with a Zener coefficient of 1.6.

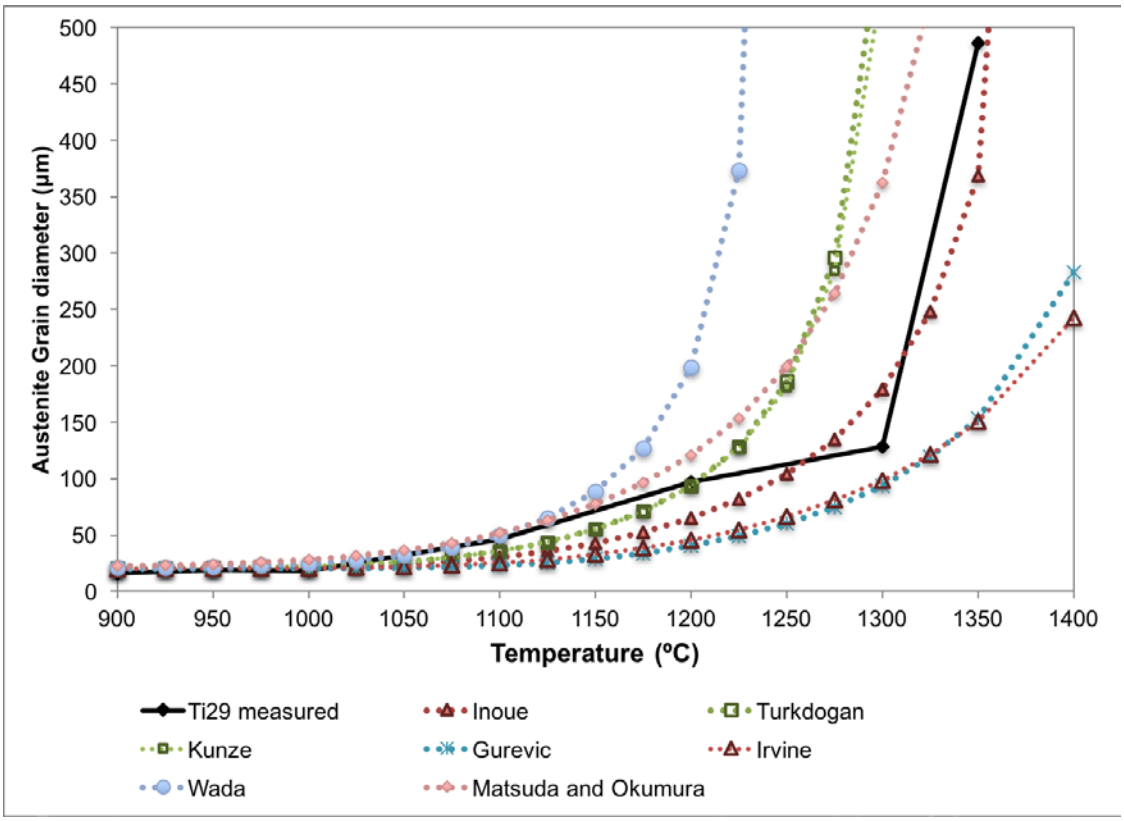

Figure 6.1. Comparison of predicted AGS for Ti29 based on different solubility product

In this work, both TEM and SEM high resolution techniques were used for the different material conditions studied, taking the advantage of the particle coarsening expected at the higher temperature ranges (i.e. 1200°C – 1350°C). While few precipitates were observed on samples from the 1350°C condition, it confirmed the small amount of Ti tied as large precipitates at that particular temperature as estimated with the volume fraction through solubility product.

Furthermore, the calculated volume fraction of second stable particles is assumed to be constant over time, meaning that at a specific holding temperature the pinning force exerted by the particles will evolve based on the rate of growth of the particle given by LSW equation (Equation 2.11.) For the grain size estimation presented in this study, only bulk diffusion of the rate-limiting solute (Ti in solution from either matrix or the dissolved precipitates) was considered.

With the use of the precipitation coarsening theory and the solubility product it was possible to predict the higher average austenite grain size in Ti54 system compared to Ti29 in the holding temperature range between 950°C and 1100°C. This would be expected since in one hand the mean particle radius in the initial state of Ti54 was larger than that of Ti29 (22.1 nm vs 15.8 nm) and on the other hand, Ti54 is anticipated to have higher concentration of Ti available in the matrix, which is the driving force for particle coarsening. On the other hand, the slightly smaller average austenite grain size observed in system T54 compared to Ti29 at 1350°C could be explained by the higher volume fraction of Ti tied as TiN and either randomly distributed on the matrix or located at the grain boundaries.

No significant indication of coarsening behavior of the TiN particles was observed at a holding temperature of 1200°C (from as-rolled starting condition), nor presence of finer precipitates at the 1350°C condition that could indicate some reprecipitation occurring within the heat treatment procedure.

6.2.3 Grain Growth Prediction Models

As it was presented in section 2.2.4, several models are available for the prediction of the austenite grain coarsening behavior in microalloyed steels, being most of them variations of the Smith-Zener equation. The Zener parameter on Gladman's expression makes it a suitable option for fitting the model based on experimental results and not surprisingly most authors declare to have found good agreement between their experimental results and Gladman's expression (Equation 2.13.)

An approach for the estimation of precipitate size and volume fraction was done taking into account just the presence of stable TiN precipitate and the solubility product by Inoue and al. was the best choice for predicting the austenite grain size under the different isothermal conditions, through the estimation of particle size and volume fraction of stable TiN precipitates; still an underestimation of the pinning effect was observed in the temperature range between 1250°C and 1300°C.

6.3 HIGH MOBILITY BOUNDARIES AND PINNING FORCE

Results obtained in this study from the EBSD analysis seem to be in agreement with those obtained by Tao et al. [49]. An interesting observation is that in their study, the dissolution analysis consisted on varying the holding time at a constant temperature and the same reduction in the fraction of HMB was observed.

For the present study, the decrease in the HMB appears to be related to the topological features of grain growth for space filling and surface tension equilibrium. The

equilibrium condition for a two-dimensional grain geometry is a 3-rayed vertex with all boundaries having equal angles of 120° which would lead to equal surface tension from all boundaries [11, 40]. Figure 6.2 shows an example of vertex angles formed by HMB analyzed by EBSD.

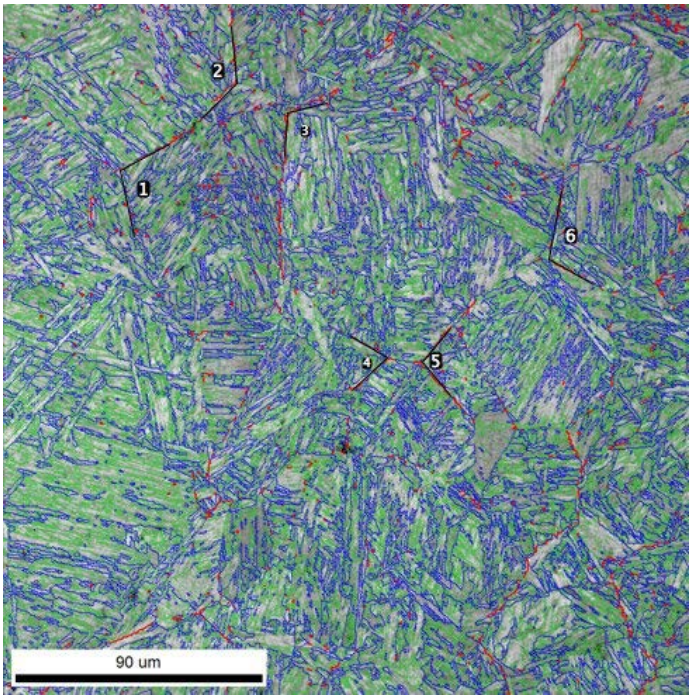

Label	Angle (°)
1	106.484
2	129.428
3	107.728
4	73.265
5	100.389
6	108.95

Figure 6.2. Examples of 2D vertex angles formed by HMB showing deviation from equilibrium.

With this concept in mind, it can be possible to correlate the evolution of high mobility boundaries with the difference in the free energy created by the surface tension from the boundaries, and therefore the driving forces for grain growth and the pinning force being exerted by the stable precipitates. Figures 6.3 and 6.4 present the exponential correlation observed between the fraction of HMB and the estimated pinning force exerted by TiN precipitates calculated with the Gladman and Flexible models, respectively, for the

Ti-bearing systems. The calculated values of pinning force for both the Gladman and Flexible models is presented in Table 5.8.

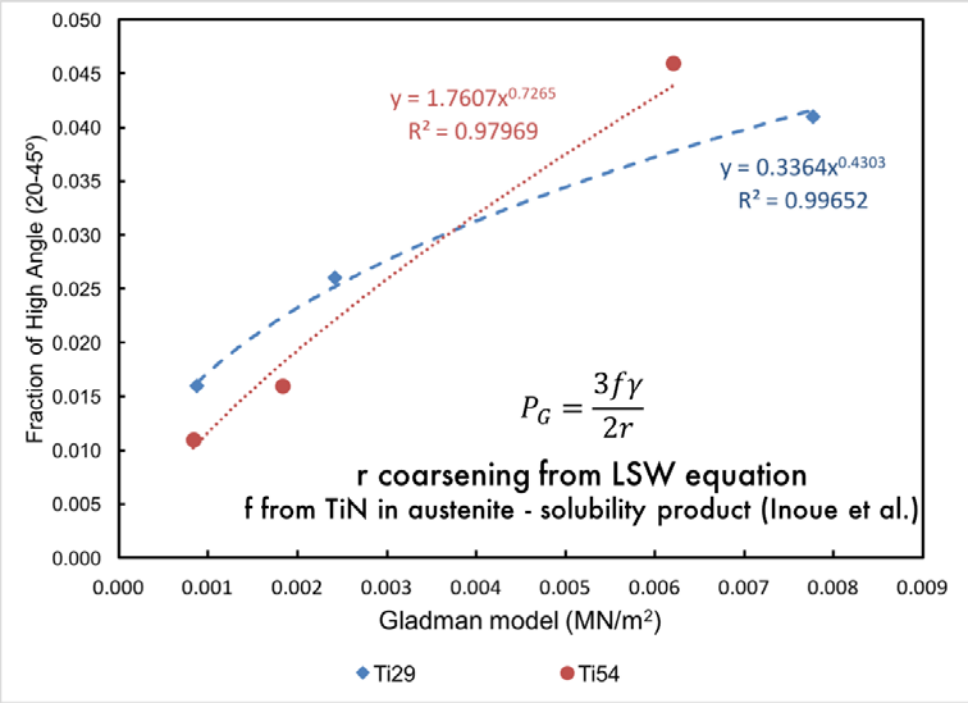

Figure 6.3. Correlation between fraction of HMB pinning force estimated with the Gladman model

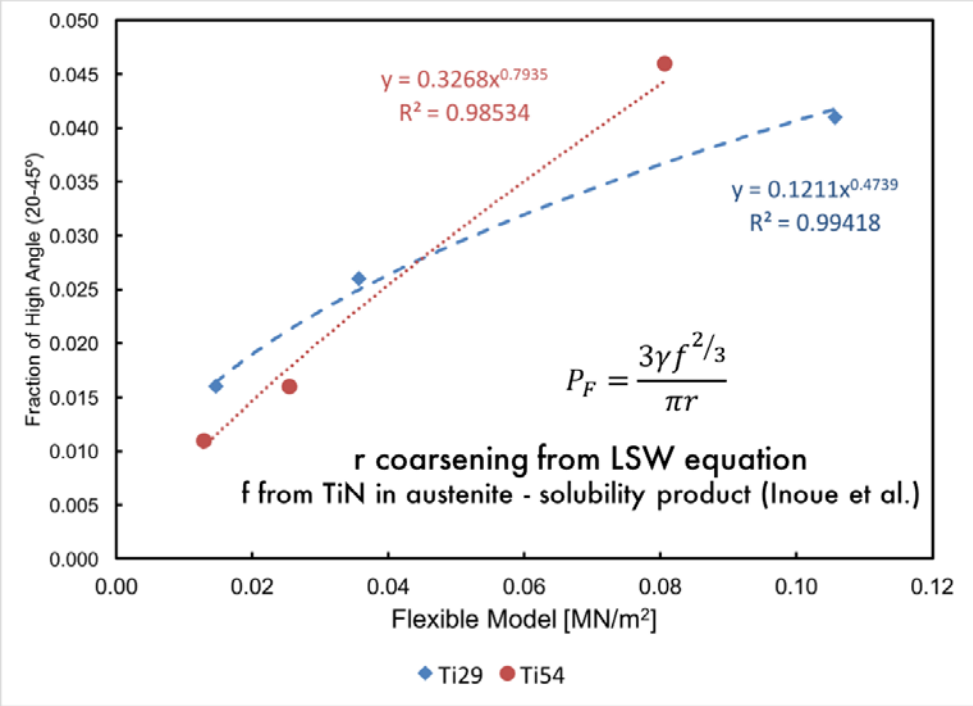

Figure 6.4. Correlation between fraction of HMB pinning force estimated with the flexible model

The correlation of the grain character distribution obtained from EBSD and the estimation of the particle coarsening and volume fraction of precipitates appears to be a new potential approach to understand the growth and dissolution of second phase and the grain structure evolution in steels. It would still be necessary to continue exploring this type of analysis with other conditions and perhaps other materials.

Another interesting observation made in both studies by Hayakawa et al., and Tao et al. is the insignificance on the role of special Coincidence Site Lattice (CSL) boundaries on the Goss Texture [50], and the austenite grain growth [49], respectively. In this study, a similar analysis on the possible correlation was conducted for CSL boundaries Σ5, Σ7, and Σ9 and no evidence of correlation with grain growth or grain boundary mobility was found between isothermal conditions.

One of the main challenges during the EBSD analysis was identifying the crystallographic features of the low-carbon martensitic structure of PAGS specimens. Kitahara et al. published a good paper that includes a procedure for conducting crystallographic analysis on lath martensite for low-carbon steels [56]. They provide a good summary of the different martensite variants (for laths, packets, blocks, and sub-blocks) transformed from austenite maintaining the Kurdjumov-Sachs (K-S) relationship and their misorientation angles. For their study, they made use of a plain C-Mn steel with no MAE addition.

Based on the observations made in the present study, Figure 6.5 depicts a schematic of the proposed austenite grain coarsening and unpinning mechanism considering the correlation with HMB (red boundaries in Figure 6.5) and the presence or absence of TiN precipitates.

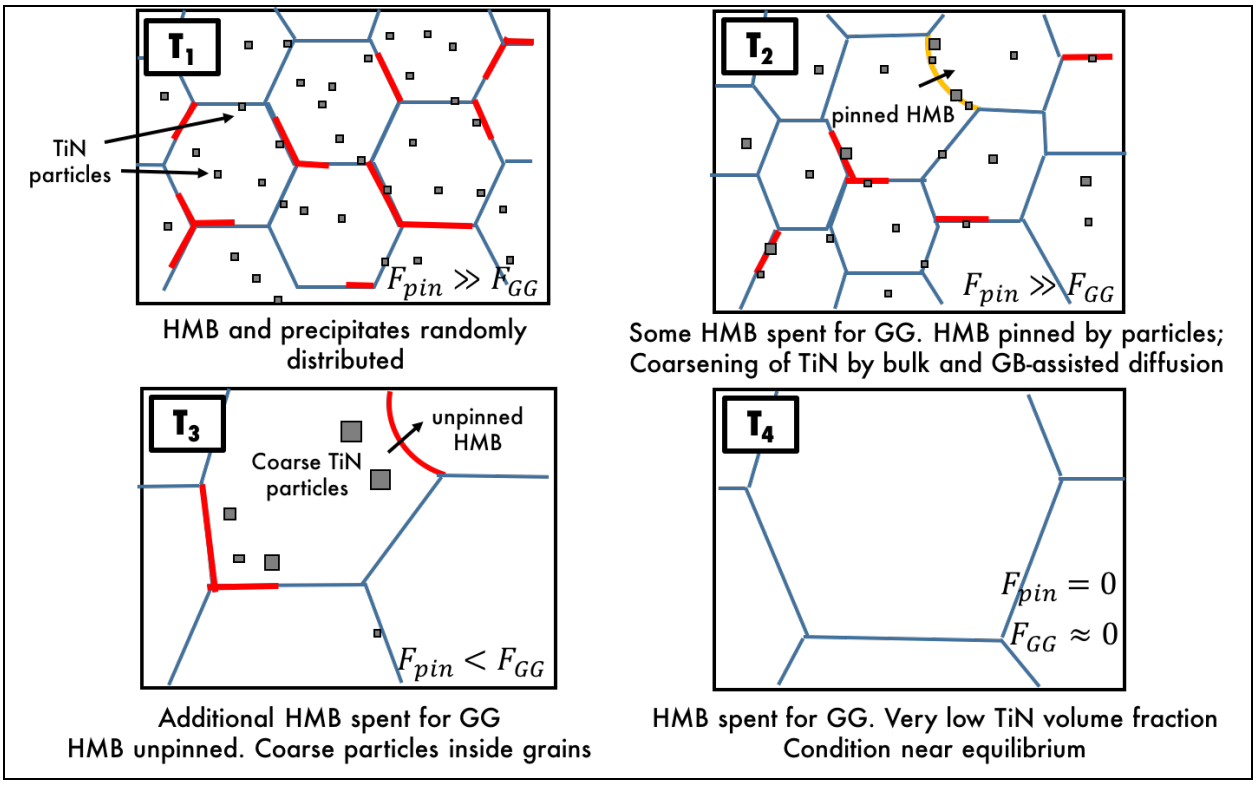

Figure 6.5. Schematics of the proposed new view of grain boundaries unpinning mechanism based on HMB, TiN coarsening and dissolution as temperature is increased. $T_1<T_2<T_3<T_4$.

As it is depicted in Figure 6.5, at a low temperature in the austenite range **T_1**, HMB and TiN precipitates appear to be randomly distributed in the matrix and grain boundaries; under this condition the pinning force exceeds the driving forces for grain growth, therefore grain boundary mobility is inhibited. At a higher temperature **T_2**, some HMB with high energy are consumed for grain growth; grain boundaries are pinned by the presence of TiN precipitates; particle coarsening and dissolution by both Oswald Ripening and grain-boundary assisted diffusion occurs on HMB. As the system is increase to a higher temperature **T_3**, HMB are eventually overcome the ineffective pinning force exerted by coarse TiN particles (located now inside the grains), some HMBs are consumed for grain coarsening. At the highest temperature in the austenite range **T_4**, TiN precipitates are

mostly dissolved; HMB are also completely spent and the system condition is near equilibrium with a small driving force for grain growth.

6.4 EFFECT OF HEATING RATE IN THE DISSOLUTION PROCESS OF PRECIPITATES

While during isothermal holding at 1350°C for 30 minutes Ti54 system showed a relatively finer AGS compared to Ti29, both stoichiometric conditions (hyper and hypo) seemed to have a similar response on precipitation stability under the high heating rate tested at 350°C/s with a holding time of one second. One particular observation was that under such fast heating conditions strong bimodal features are not observed compared to those observed during isothermal treatments at high temperatures and holding time of 30 minutes.

In their publication from 2010, Banerjee et at. [22] discuss the effect of high heating on the rate of short dissolution times of NbCN and TiN precipitates. In one hand they conclude that for heating rates higher than 100°C/s (similar to conditions in the HAZ) the austenite grain coarsening behavior is purely dependent on the peak temperature and independent of the heating rate. Another important observation they make is the absence of the bimodal behavior in the austenite grain size measured from high heating rate conditions which is similar to what it was observed in this study (Section 5.2.6.). This is associated to the expected increase in the dissolution temperatures for precipitates and the superheating of the ferrite or initial state of the material.

Both Ti29 and Ti54 presented precipitate thermal stability in the high heating rate experiments and this was clearly observed when compared to the results obtained at the same temperature of 1350°C in the isothermal treatments for PAGS. A similar austenite grain coarsening behavior in Ti-bearing low-carbon steels was observed by Liu and Liao [39], for the low nitrogen (30 ppm) alloy system, the austenite grain measured for a condition of heating rate (200°C/s) up to a peak temperature of 1350°C was of 170 μm for 2 seconds of holding time and increased up to 350 μm for a holding time of 1 min. This last value means that at that holding time of 60 seconds at 1350°C pinning forces of TiN (and therefore their stability) are ineffective for grain growth inhibition.

The observations made by different authors confirm a strong peak temperature dependence of particle coarsening and dissolution at the high temperature range of a welding thermal cycle and this is relevant when considering potential differences in the estimations of grain coarsening behavior between isothermal treatments and welding-type cycles.

This study was focused the dissolution mechanisms, in particular for stable TiN precipitates, an interesting future approach would be to continue with the evaluation of possible reprecipitation of different nitrides or carbides during both reheating, cooling after peak temperatures during welding thermal cycles or even during tempering conditions depending on the solute concentration available in the matrix and the type of applications and final mechanical properties desired in the product.

6.5 EFFECT OF STOICHIOMETRY ON MECHANICAL PROPERTIES

The mechanical properties assessment presented in this study in the as-rolled condition was considered complementary and important in this study as a way to assess the potential effect of the Ti/N stoichiometry on the material performance (i.e. hardness, fracture toughness). This way some quantifications and comparisons can be made with respect to other author's findings.

For instance, Shen et al. concluded that the increase in volume fraction of coarse TiN particles was the main responsible in the reduction of the toughness properties of quenched and tempered steels [45]. They concluded that higher content of Ti in excess will increase the hardenability of steel in as quenched condition and also will increase strength properties after tempering as fine Ti(C,N) precipitates will form. Other studies have also concluded the significance of the Ti/N ration in the growth behavior of TiN particles during different heat treatment conditions and their impact on toughness properties when these particles coarsen [43, 57, 58].

In the present study, mechanical properties were assessed in the as-rolled condition. While this is unlikely to be the delivery condition for most high-end seamless line pipe steel products offer in the market (especially if they require to comply with requirements for critical applications) it was considered important to have a reference for the observations that many authors have addressed. It was observed that the mechanical properties of the Ti-bearing alloy systems were superior compared to the Ti-free alloy for both toughness and tensile properties in the as-rolled condition. A further assessment of mechanical properties for the different alloy systems under different heat treatment

conditions (i.e. quenched and tempered, normalized, thermo-mechanical) could be an interesting future work for exploring the role of stoichiometry of Ti/N in the performance of material.

6.6 EFFECT OF OTHER ELEMENTS IN PRECIPITATION STABILITY

Several authors have studied the effect other elements in the precipitation stability of TiN. In the present work, there was no direct observation on the effect of the presence of other nitride or carbide formers such as Vanadium, Aluminum, in the precipitation stability of TiN.

Adrian and Pickering studied the effect increased content of Nb in Ti and V steels on the decrease the size (and stability) of the carbonitride particles [23], observing that generally their stability increases with the increased amount of microalloying elements which have strong affinity with C and N. Moreover, they conclude that the concentration of N in solid solution decreases with simultaneous additions of Ti, Nb and V and suggest that this affects the rate at which austenite decomposes, having therefore effects in the hardenability of the material.

Enloe et al. recently presented a work that shows the possible effect of elements such as Mo, Al, and V on retarding the coarsening behavior of precipitates and therefore the austenite grain pinning effect [48]. They include a discussion on the Mo effect on the reduction of the diffusivity of Ti by the hypothesis of replacing Ti atoms by Mo atoms on

the metallic sublattice (reduction of frequency factor or preferential exchange of other elements to available sites.)

Additionally, Loberg et al. observed a decreased in the stability of TiN particles on normalized alloy designs as a result of higher additions of another strong nitride formers such as Al and V (this latter to a less extent) that would compete for the nitrogen available in the system [42]. The same observations were made by Lee et al. in their study about the interaction of V, Al, and N in microalloyed forging steels under different temperatures and holding times [59].

In this study, V and Mo showed the strongest interaction with Ti and interstitial elements by the formation of the complex irregular-shaped particles observed in the as-rolled condition.

7.0 CONCLUSIONS

Ti-bearing systems showed a better control in the austenite grain coarsening behavior compared to the alloy system without Titanium. Prior austenite grain growth experiments showed good agreement with predictions following a classical approach of particle coarsening theory and Gladman's expression.

Based on the results obtained in this study, the concentration of Ti in solution, under the different thermal conditions, was considered the most relevant parameter in the prediction of the coarsening and dissolution of TiN precipitates and consequently the austenite grain coarsening behavior.

EBSD analysis showed that high angle boundaries with misorientation angle between 20° and 45° might have been responsible of grain boundary mobility at the different austenitizing temperatures during isothermal heat treatments.

Grain boundary character distribution analysis results obtained in this study provided a strong correlation between the high angle boundaries with misorientations between 20° and 45° and the estimated pinning force exerted by TiN particles. The findings suggest that this approach could also be applied on other materials, heat treatment cycles, or temperature ranges.

It is considered that the present work contributes with a new view for the understanding of the austenite grain coarsening behavior in Ti-bearing low carbon steels

through the integration of prediction models, experimental work, material assessments, and the exploration of advanced microscopy characterization methods for the analysis of austenite grain boundaries.

8.0 FUTURE WORK

Based on the observations made from the results obtained in this study, it is considered that the methodology presented can be applied to other materials as well as other temperature ranges and thermal cycles. The following topics are potential future works based on unanswered research questions and findings in the present work:

- High Mobility Boundaries (HMB) analysis in the mixed-grained austenite temperature range.
- Role of Ti/N ratio on the fraction of HMB and its correlation with the mixed-grained austenite temperature range.
- Precipitation stability analysis under different simulated welding thermal cycles: HMB evolution during a thermal cycle, i.e. high heat input, low heat input.
- Study the kinetics of other carbide and nitride formers (i.e. V, Nb, and Al.)

APPENDIX A

EBSD ANALYSIS DATA

Table A.1. Summary of EBSD data for OIM analysis

Alloy System	PAGS Condition (°C)	Number of Points	Scanned Area (μm x μm)	Step Size (μm)	Avg Confidence Index	Avg Image Quality	Average Fit (degrees)
TiF	900	288212	100 x 100	0.2	0.26	3533	1.89
Ti29	900	288212	100 x 100	0.2	0.24	3533	1.93
Ti54	900	287058	100 x 100	0.2	0.26	3816	1.62
TiF	1100	454739	250 x 250	0.4	0.30	3274	2.05
Ti29	1200	454739	250 x 250	0.4	0.20	2885	2.14
Ti54	1200	454739	250 x 250	0.4	0.22	3768	1.68
TiF	1300	648318	300 x 300	0.4	0.35	4361	1.49
Ti29	1300	454739	250 x 250	0.4	0.22	4362	1.46
Ti54	1300	454739	250 x 250	0.4	0.27	4449	1.50

A.1 INVERSE POLE FIGURES

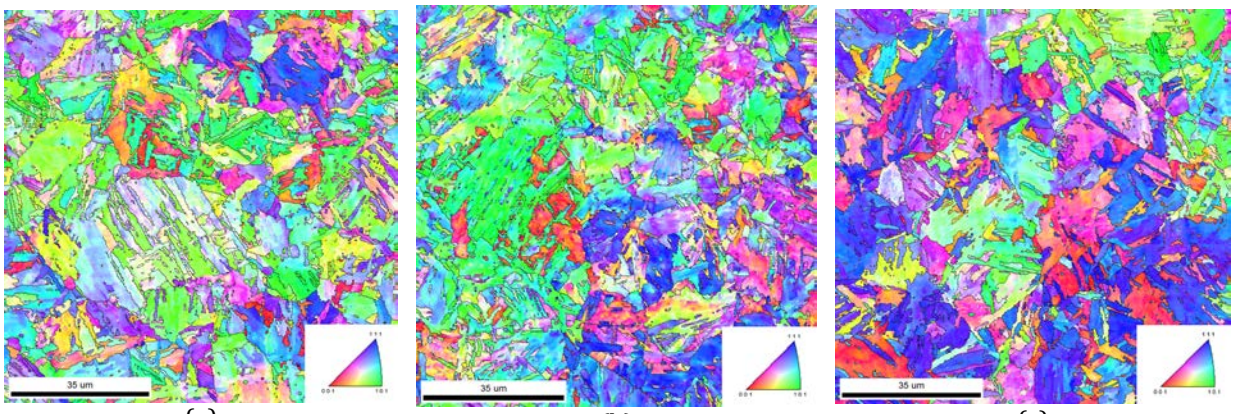

(a) (b) (c)

Figure A.1. Inverse Pole Figures for 900°C Condition. (a) Ti29, (b) Ti54, (c) TiF

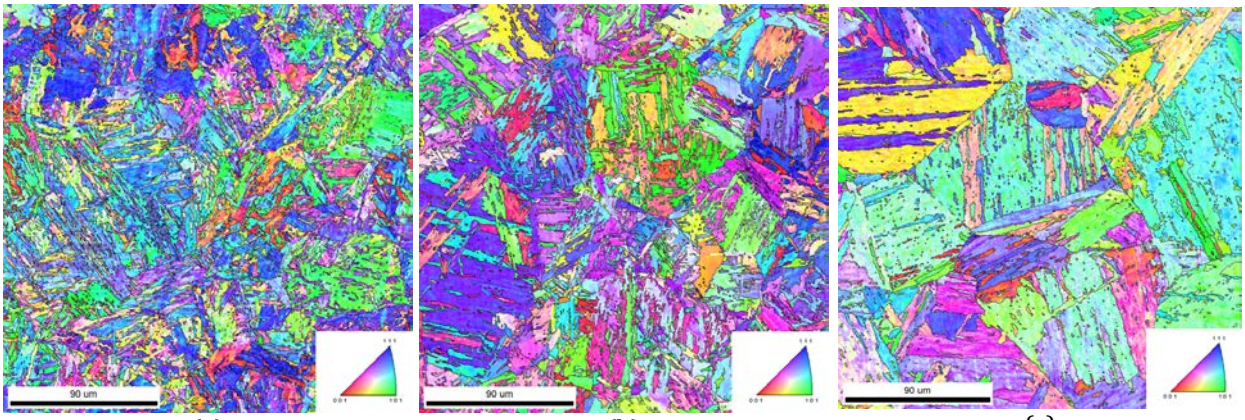

(a) (b) (c)

Figure A.2. Inverse Pole Figures for 1200°C Condition: (a) Ti29, and (b) Ti54; and 1100°C condition: (c) TiF

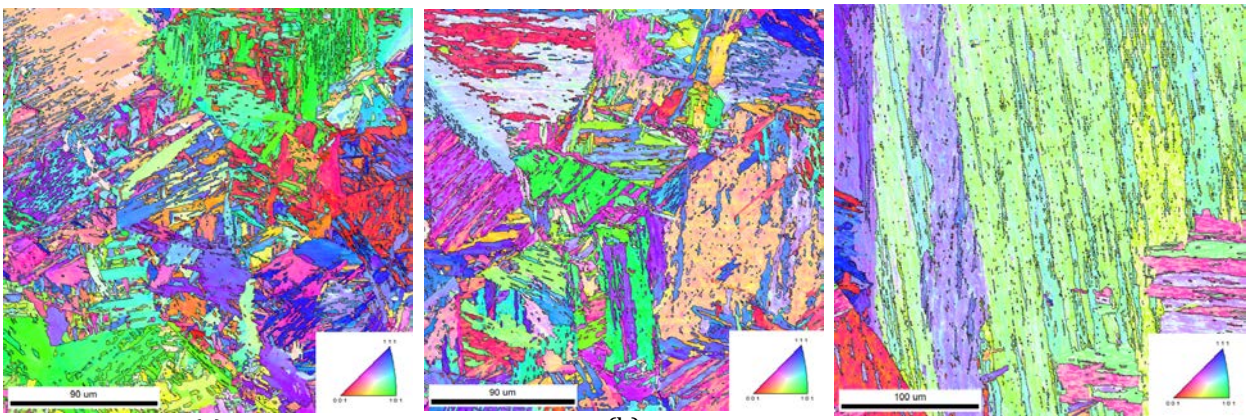

(a) (b) (c)

Figure A.3. Inverse Pole Figures for 1300°C Condition: (a) Ti29, and (b) Ti54, (c) TiF

A.2 MISORIENTATION DISTRIBUTION

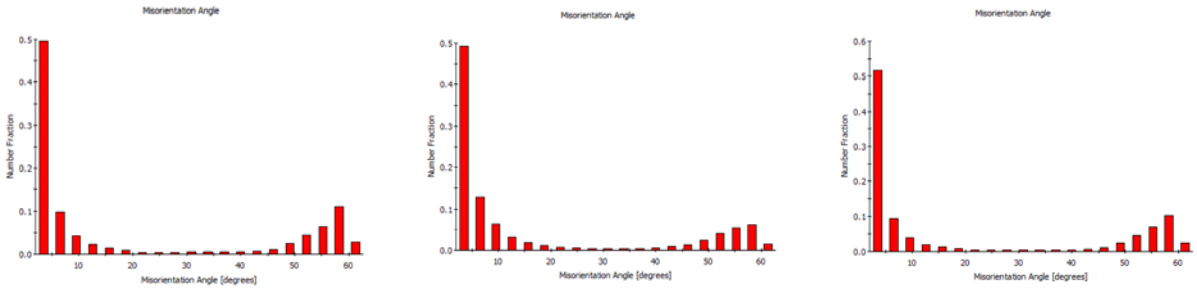

(a) (b) (c)

Figure A.4. Misorientation Distribution for 900°C Condition. (a) Ti29, (b) Ti54, (c) TiF

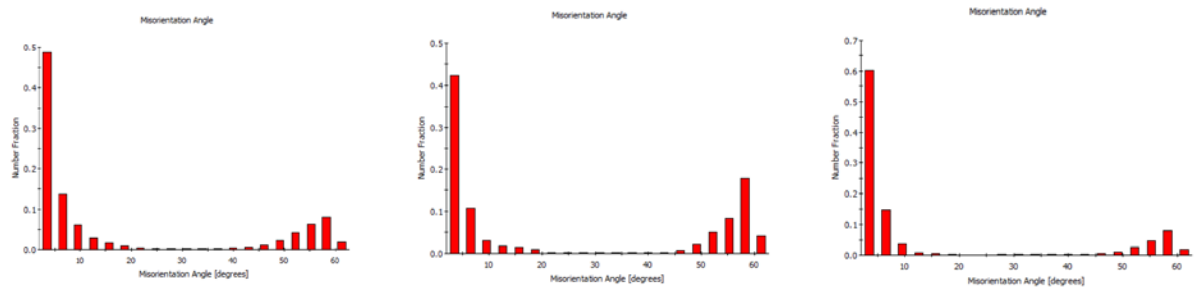

(a) (b) (c)

Figure A.5. Misorientation Distribution for 1200°C Condition: (a) Ti29, and (b) Ti54; and 1100°C condition: (c) TiF

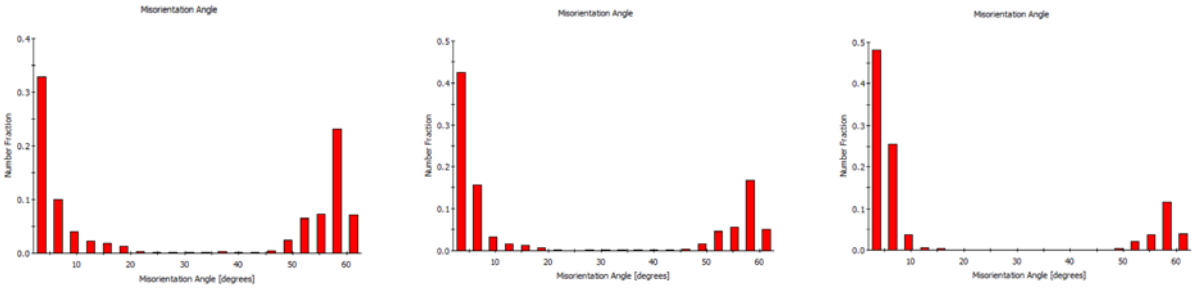

(a) (b) (c)

Figure A.6. Misorientation Distribution for 1300°C Condition. (a) Ti29, (b) Ti54, (c) TiF

REFERENCES

[1] W. B. Morrison, "Microalloy steels the beginning," Materials Science and Technology, vol. 25, pp. 1066-1073, 2009.

[2] T. N. Baker, "Processes, microstructure and properties of vanadium microalloyed steels," Materials Science and Technology, vol. 25, pp. 1083-1107, 2009.

[3] N. Gao and T. N. Baker, "Austenite Grain Growth Behaviour of Microalloyed Al–V–N and Al–V–Ti–N Steels," ISIJ International, vol. 38, pp. 744-751, 1998.

[4] A. Grajcar, "Thermodynamic analysis of precipitation processes in Nb–Ti-microalloyed Si–Al TRIP steel," Journal of Thermal Analysis and Calorimetry, vol. 118, pp. 1011-1020, 2014.

[5] Z. Wang, X. Mao, Z. Yang, X. Sun, Q. Yong, Z. Li, et al., "Strain-induced precipitation in a Ti micro-alloyed HSLA steel," Materials Science & Engineering A, vol. 529, pp. 459-467, 2011.

[6] L. J. Cuddy and J. C. Raley, "Austenite grain coarsening in microalloyed steels," Metallurgical Transactions A, vol. 14, pp. 1989-1995, 1983.

[7] J. Moon, J. Lee, and C. Lee, "Prediction for the austenite grain size in the presence of growing particles in the weld HAZ of Ti-microalloyed steel," Materials Science & Engineering A, vol. 459, pp. 40-46, 2007.

[8] S. Matsuda and N. Okumura, "EFFECT OF THE STATE OF DISPERSION OF TITANIUM NITRIDE ON THE AUSTENITE GRAIN SIZE OF LOW-CARBON LOW-ALLOY STEELS," Tetsu-To-Hagane/Journal of the Iron and Steel Institute of Japan, vol. 62, pp. 1209-1218, 1976.

[9] S. C. Wang, "The effect of titanium and nitrogen contents on the austenite grain coarsening temperature," Journal of Materials Science, vol. 24, pp. 105-109, 1989.

[10] S. F. Medina, M. Chapa, P. Valles, A. Quispe, and M. I. Vega, "Influence of Ti and N contents on austenite grain control and precipitate size in structural steels," ISIJ International, vol. 39, pp. 930-936, 1999.

[11] T. Gladman, The physical metallurgy of microalloyed steels vol. 615.;615;. London: Institute of Materials, 1997.

[12] I. I. Gorbachev, A. Y. Pasynkov, and V. V. Popov, "Prediction of the austenite-grain size of microalloyed steels based on the simulation of the evolution of carbonitride precipitates," The Physics of Metals and Metallography, vol. 116, pp. 1127-1134, 2015.

[13] N. Isasti, D. Jorge-Badiola, M. L. Taheri, and P. Uranga, "Microstructural and precipitation characterization in Nb-Mo microalloyed steels: Estimation of the contributions to the strength," Metals and Materials International, vol. 20, pp. 807-817, 2014.

[14] B. K. Show, R. Veerababu, R. Balamuralikrishnan, and G. Malakondaiah, "Effect of vanadium and titanium modification on the microstructure and mechanical properties of a microalloyed HSLA steel," Materials Science and Engineering A, vol. 527, pp. 1595-1604, 2010.

[15] H. R. Wang and W. Wang, "Precipitation of complex carbonitrides in a Nb–Ti microalloyed plate steel," Journal of Materials Science, vol. 44, pp. 591-600, 2009.

[16] S. Shanmugam, M. Tanniru, R. D. K. Misra, D. Panda, and S. Jansto, "Microalloyed V-Nb-Ti and V steels Part 2 - Precipitation behaviour during processing of structural beams," Materials Science and Technology, vol. 21, pp. 165-177, 2005.

[17] X.-l. Wan, K.-m. Wu, G. Huang, R. Wei, and L. Cheng, "In situ observation of austenite grain growth behavior in the simulated coarse-grained heat-affected zone of Ti-microalloyed steels," International Journal of Minerals, Metallurgy, and Materials, vol. 21, pp. 878-885, 2014/09/01 2014.

[18] P. A. Beck, J. C. Kremer, and L. Demer, "Grain Growth in High Purity Aluminum," Physical Review, vol. 71, pp. 555-555, 1947.

[19] Q. Sha and Z. Sun, "Grain growth behavior of coarse-grained austenite in a Nb–V–Ti microalloyed steel," Materials Science & Engineering A, vol. 523, pp. 77-84, 2009.

[20] D. Dong, F. Chen, and Z. Cui, "Modeling of Austenite Grain Growth During Austenitization in a Low Alloy Steel," Journal of Materials Engineering and Performance, vol. 25, pp. 152-164, 2016.

[21] M. I. Vega, S. F. Medina, A. Quispe, P. P. Gómez, and M. Gómez, "Recrystallisation driving forces against pinning forces in hot rolling of Ti-microalloyed steels," Materials Science & Engineering A, vol. 423, pp. 253-261, 2006.

[22] K. Banerjee, M. Militzer, M. Perez, and X. Wang, "Nonisothermal Austenite Grain Growth Kinetics in a Microalloyed X80 Linepipe Steel," Metallurgical and Materials Transactions A, vol. 41, pp. 3161-3172, 2010.

[23] H. Adrian and F. B. Pickering, "Effect of titanium additions on austenite grain growth kinetics of medium carbon V–Nb steels containing 0·008–0·018%N," Materials Science and Technology (United Kingdom), vol. 7, pp. 176-182, 1991.

[24] K. Xu, B. G. Thomas, and R. O'malley, "Equilibrium Model of Precipitation in Microalloyed Steels," Metallurgical and Materials Transactions A, vol. 42, pp. 524-539, 2011.

[25] K. Inoue, I. Ohnuma, H. Ohtaimi, K. Ishida, and T. Nishizawa, "Solubility product of Tin in austenite," ISIJ International, vol. 38, pp. 991-997, 1998.

[26] M. I. Vega, S. F. Medina, A. Quispe, M. GÓMez, and P. P. GÓMez, "Influence of TiN Particle Precipitation State on Static Recrystallisation in Structural Steels," ISIJ International, vol. 45, pp. 1878-1886, 2005.

[27] J. Moon, C. Lee, J. Lee, and S. Uhm, "Coarsening kinetics of TiN particle in a low alloyed steel in weld HAZ: Considering critical particle size," Acta Materialia, vol. 54, pp. 1053-1061, 2006.

[28] M. Opiela, "Analysis of the kinetics of precipitation of MX-type interstitial phases in microalloyed steels," Journal of Achievements in Materials and Manufacturing Engineering, vol. 47, pp. 7-18, 2011.

[29] S. P. Ringer, R. P. Kuziak, and K. E. Easterling, "Liquid film simulation of Zener grain boundary pinning by second phase particles," Materials Science and Technology (United Kingdom), vol. 7, pp. 193-200, 1991.

[30] D. A. Porter and K. E. Easterling, Phase transformations in metals and alloys. New York: Van Nostrand Reinhold, 1981.

[31] T. Gladman, "On the Theory of the Effect of Precipitate Particles on Grain Growth in Metals," Proceedings of the Royal Society of London. Series A, Mathematical and Physical Sciences, vol. 294, pp. 298-309, 1966.

[32] T. Nishizawa, I. Ohnuma, and K. Ishida, "Examination of the Zener relationship between grain size and particle dispersion," Materials Transactions, JIM, vol. 38, pp. 950-956, 1997.

[33] P. R. Rios, "On the relationship between pinning force and limiting grain radius," Scripta Materialia, vol. 34, pp. 1185-1188, 1996.

[34] E. J. Palmiere, C. I. Garcia, and A. J. DeArdo, "The influence of niobium supersaturation in austenite on the static recrystallization behavior of low carbon microalloyed steels," Metallurgical and Materials Transactions A: Physical Metallurgy and Materials Science, vol. 27, pp. 951-960, 1996.

[35] A. J. DeArdo, M. J. Hua, K. G. Cho, and C. I. Garcia, "On strength of microalloyed steels: an interpretive review," Materials Science and Technology, vol. 25, pp. 1074-1082, 2009.

[36] I. G. V. Rak and M. Kocak, "Weldability and toughness assessment of Ti-microalloyed offshore steel," Metallurgical and Materials Transactions.A, Physical Metallurgy and Materials Science, vol. 28, pp. 199-206, 1997.

[37] S. Suzuki, G. C. Weatherly, and D. C. Houghton, "The response of carbo-nitride particles in hsla steels to weld thermal cycles," Acta Metallurgica, vol. 35, pp. 341-352, 1987.

[38] K. E. Easterling, Introduction to the physical metallurgy of welding vol. 2nd. Oxford;Boston;: Butterworth Heinemann, 1992.

[39] S. Liu and F.-C. Liao, "Precipitate stability in the heat affected zone of nitrogen-enhanced high strength low alloy steels," Materials Science & Engineering A, vol. 244, pp. 273-283, 1998.

[40] S. Mishra and T. DebRoy, "Non-isothermal grain growth in metals and alloys," Materials Science and Technology, vol. 22, pp. 253-278, 2006.

[41] M. F. Ashby and K. E. Easterling, "A first report on diagrams for grain growth in welds," Acta Metallurgica, vol. 30, pp. 1969-1978, 1982.

[42] B. Loberg, A. Nordgren, J. Strid, and K. E. Easterling, "ROLE OF ALLOY COMPOSITION ON THE STABILITY OF NITRIDES IN Ti-MICROALLOYED STEELS DURING WELD THERMAL CYCLES," Metallurgical transactions. A, Physical metallurgy and materials science, vol. 15 A, pp. 33-41, 1984.

[43] W. Yan, Y. Y. Shan, and K. Yang, "Effect of TiN inclusions on the impact toughness of low-carbon microalloyed steels," Metallurgical and Materials Transactions A: Physical Metallurgy and Materials Science, vol. 37, pp. 2147-2158, 2006.

[44] B. L. Bramfitt and J. G. Speer, "A perspective on the morphology of bainite," Metallurgical Transactions A, vol. 21, pp. 817-829, 1990.

[45] Y. H. S. S. Shen, "Effect of the Ti/N ratio on the hardenability and mechanical properties of a quenched-and-tempered C-Mn-B steel," Metallurgical and Materials Transactions.A, Physical Metallurgy and Materials Science, vol. 28, pp. 2027-2035, 1997.

[46] P. A. Manohar, D. P. Dunne, T. Chandra, and C. R. Killmore, "Grain growth predictions in microalloyed steels," ISIJ International, vol. 36, pp. 194-200, 1996.

[47] S. Uhm, J. Moon, C. Lee, J. Yoon, and B. Lee, "Prediction model for the austenite grain size in the coarse grained heat affected zone of Fe-C-Mn steels: Considering the

effect of initial grain size on isothermal growth behavior," ISIJ International, vol. 44, pp. 1230-1237, 2004.

[48] C. M. Enloe, K. O. Findley, and J. G. Speer, "Austenite Grain Growth and Precipitate Evolution in a Carburizing Steel with Combined Niobium and Molybdenum Additions," Metallurgical and Materials Transactions A, vol. 46, pp. 5308-5328, 2015.

[49] X. Tao, J. Gu, and L. Han, "Carbonitride Dissolution and Austenite Grain Growth in a High Cr Ferritic Heat-resistant Steel," ISIJ International, vol. 54, pp. 1705-1714, 2014.

[50] Y. Hayakawa and J. A. Szpunar, "The role of grain boundary character distribution in secondary recrystallization of electrical steels," Acta Materialia, vol. 45, pp. 1285-1295, 3// 1997.

[51] R. M. Alé, J. M. A. Rebello, and J. Charlier, "A metallographic technique for detecting martensite-austenite constituents in the weld heat-affected zone of a micro-alloyed steel," Materials Characterization, vol. 37, pp. 89-93, 1996.

[52] J. G. S. Amar K. De and K. M. David, "Color Tint-Etching for Multiphase Steels," vol. 161, ed: ASM International, 2003, p. 27.

[53] H. R. Wang and W. Wang, "Simple model for austenite grain growth in microalloyed steels," Materials Science and Technology, vol. 24, pp. 228-232, 2008.

[54] G. Gottstein, L. S. Shvindlerman, and I. ebrary, Grain boundary migration in metals: thermodynamics, kinetics, applications vol. 2nd. Boca Raton: Taylor & Francis, 2010.

[55] A. Hossain Seikh, M. S. Soliman, A. Almajid, K. Alhajeri, and W. Alshalfan, "Austenite grain growth kinetics in API X65 and X70 line-pipe steels during isothermal heating," Advances in Materials Science and Engineering, vol. 2014, 2014.

[56] H. Kitahara, R. Ueji, N. Tsuji, and Y. Minamino, "Crystallographic features of lath martensite in low-carbon steel," Acta Materialia, vol. 54, pp. 1279-1288, 2006.

[57] W. Yan, Y. Y. Shan, and K. Yang, "Influence of TiN inclusions on the cleavage fracture behavior of low-carbon microalloyed steels," Metallurgical and Materials Transactions A: Physical Metallurgy and Materials Science, vol. 38, pp. 1211-1222, 2007.

[58] Y. Fukui, D. P. Fairchild, H. Okada, D. G. Howden, N. Kumazawa, W. A. T. Clark, et al., "The mechanism of brittle fracture in a microalloyed steel: Part I. Inclusion-induced cleavage," Metallurgical and Materials Transactions A, vol. 31, pp. 2627; 641-652; 2636, 2000.

[59] L. M. Rothleutner, R. Cryderman, and C. J. Van Tyne, "Influence of Temperature and Holding Time on the Interaction of V, Al, and N in Microalloyed Forging Steels," Metallurgical and Materials Transactions A, vol. 45, pp. 4594-4609, 2014.